AN INVERSE SCATTERING APPROACH TO IMAGING USING MARCHENKO EQUATIONS IN THE PRESENCE OF A FREE SURFACE

by

Satyan Singh

A thesis submitted to the Faculty and the Board of Trustees of the Colorado School of Mines in partial fulfillment of the requirements for the degree of Doctor of Philosophy (Geophysics).

Golden, Colorado

Date _____

Signed: _____
Satyan Singh

Signed: _____
Dr. Roel Snieder
Thesis Advisor

Golden, Colorado

Date _____

Signed: _____
Dr. Terence K. Young
Professor and Head
Department of Geophysics

ABSTRACT

The Green's function is the impulse response of a system and is used to infer the properties of the system from surface measurements. In exploration seismology, imaging algorithms use estimates of the Green's functions along with surface measurements to image the subsurface, i.e. locate the Earth's interfaces and its properties, so as to identify valuable energy resources. These conventional imaging algorithms only account for singly reflected waves (primaries) in the subsurface and hence, in the subsurface image, produce false interfaces in the presence of multiply reflected waves (internal and free-surface multiples).

Recent work has shown that we can retrieve the Green's function that accounts for primaries and internal multiples. Imaging with these Green's functions reduces the artifacts caused by internal multiples compared to conventional imaging algorithms. These Green's functions require the free-surface multiples to be removed from the surface measurements before retrieval and imaging.

I modify the retrieval of the Green's function to account for free-surface reflections and therefore no longer require the free-surface multiples to be removed from the surface measurements. Thus the Green's function, in the method I propose, includes not only primaries and internal multiples but also free-surface multiples. These Green's functions are constructed from an arbitrary point *in the subsurface* (no physical receiver is required at this location) to *the surface*.

The method I use to retrieve the Green's function does not specify the approach to image the subsurface. In this thesis I also analyze different imaging strategies using the retrieved Green's functions. Imaging with these Green's functions reduces the artifacts caused by multiply reflected waves compared to standard imaging algorithms. Significantly, the Green's function that I retrieve and use for imaging require the same inputs as conventional imaging algorithms: the surface measurements and a smooth version of the subsurface velocity.

I also extend the construction of the Green's function from the subsurface to the surface to any two arbitrary points in the *subsurface* (no physical source or physical receiver is required at either

of these locations). This Green's function is called the virtual Green's function and includes all the primaries, internal and free-surface multiples. The virtual Green's function retrieval requires the same inputs as the previously mentioned Green's functions.

TABLE OF CONTENTS

LIST OF FIGURES

LIST OF TABLES

ACKNOWLEDGMENTS

It's a bitter-sweet feeling writing this, the last section of my thesis, but it's probably the most important section. Throughout my academic career, I have met and thankfully been taught by great men, unfortunately I do not have the space to mention them all here, but thank you all.

A good/great teacher can inspire hope, ignite the imagination, and instill a love of learning, Brad Henry.

Roel you are a great teacher. Actually, my words cannot explain how blessed I felt to be your advisee/student. You were not just my advisor, you were my friend. Your jokes were not good as mine but at least you tried.

I am probably only writing this thesis today as a CWP PhD because of Jyoti's intervention in my graduate career. Thanks a lot Jo, I am eternally gratefully to you. Jyoti and Roel, thanks for believing in me.

Luc Ikelle was my graduate advisor at Texas A&M. Thanks Luc for pushing me to leave Texas and come to CWP for bigger and better things; and thank you Paul Sava for accepting me at CWP.

Thank you Dipchand Bahal and Ravi Rajaballe, my Mathematics and Physics teachers at Presentation College Chaguanas, Trinidad, for pushing me to achieve academic success that even I doubted. Your impact on my academic life was in no way small. Keep inspiring.

Diane you have been my mother away from home. I am grateful for our conversations, your advice and your food. You have helped me tremendously become a better writer and person. If you read my acknowledgements Diane, it is probably poorly written as I am speaking my 'mother tongue' in this section.

Thanks to my committee members, Terry Young, Paul Martin, Leslie Wood and Mike Batzle (RIP). Pamela Kraus and Shingo Ishida: thanks for making my graduate career logistically easy; you two were always there when I was in trouble or needed help with 'grad school hassles'. My co-authors in Kees Wapenaar, Joost van Der Neut, Evert Slob and Jan Thorbecke, it was a pleasure

to learn and collaborate with you all.

My friends made my stay here both eventful and life changing and I thank you all for that. Special thanks to Esteban Diaz, Mauricio Pedrassi and Vladimir Li, who were like brothers, for leading me away from the straight and narrow; I needed it. Also Nishant Kamath despite our totally different personalities, you were a great friend and roommate during my PhD.

Finally, thank you my mother, my father and my brother, Sachin Singh (I mentioned his name so he can become a little famous) for being my support and motivation to pursue excellence.

CHAPTER 1

GENERAL INTRODUCTION

One of the main goals of geophysicists is to image the subsurface of the Earth in order to locate mineral deposits or other resources. By *image* I mean the location of the interfaces and its properties. Generally, to image an area of interest, one has available the reflection response at the surface and a smooth version of the velocity. The reflection response at the surface consists of the waves, generated by a source, that are reflected from the interior of the Earth and recorded by receivers at the surface. We can also think of the reflection response as the surface expression of the wavefield generated by a source. The reflection response consists of primary events which have one reflection point in the subsurface and multiples which have more than one reflection point in the subsurface. Multiples can be categorized further as 1) internal multiples which have more than one reflection point in the subsurface, and 2) free-surface multiples which have at least one reflection point at the free surface as shown in Figure 1.1.

Using a form of Green's theorem, one can relate the surface reflection response to properties of the medium in the volume (Challis and Sheard, 2003; Morse and Feshbach, 1953; Schneider, 1978):

$$U(x,t) = \frac{1}{4\pi}\int dt_0 \int dS_0 \{G\frac{\partial}{\partial n}R(x_0,t_0) - R(x_0,t_0)\frac{\partial}{\partial n}G\}, \tag{1.1}$$

where $R(x_0,t_0)$ is the reflection response at the surface S_0 for a fixed source (the surface expression of $U(x,t)$), $U(x,t)$ is the wavefield at a point x in the subsurface (interior of the volume) that is generated by the same source, G is the Green's function. Note that the subscript 0 in x_0 means it is the coordinate at the surface while t_0 is the time at which the surface reflection $R(x_0,t_0)$ is observed.

The reflection response $R(x_0,t_0)$ is recorded at the surface, therefore, if one can compute G, we can find the the field inside the medium $U(x,t)$, which in turn gives the properties of the medium, specifically the location and reflection coefficients of the interfaces (equation 1.1). The Green's

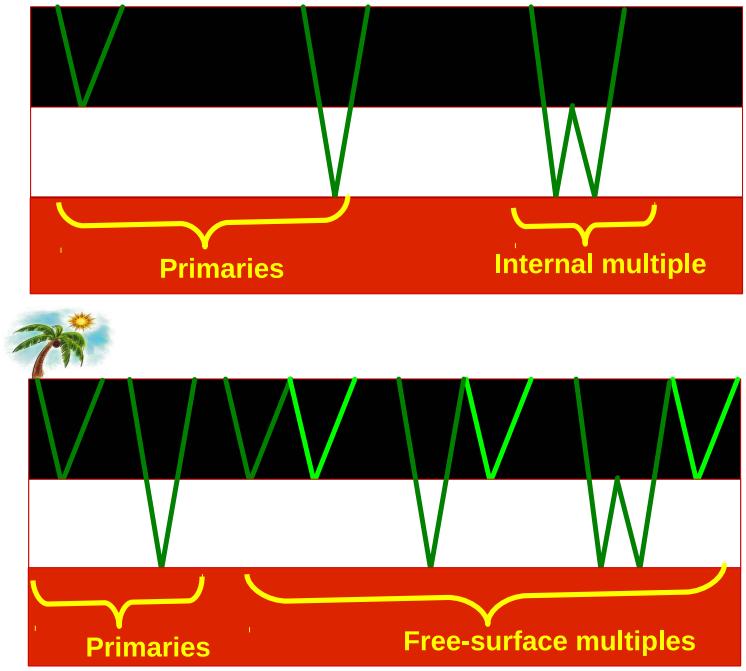

Figure 1.1: Simple model that illustrates primaries, internal multiples, and free-surface multiples. The tree symbolizes the presence of a free surface.

function G is the impulse response of the medium between two points in the medium; for equation 1.1, G is the Green's function between the subsurface point x and the acquisition surface S_0.

Kirchhoff migration (Wiggins, 1984), a standard imaging technique, constructs the Green's function G from the smooth version of the velocity and substitutes this Green's function in equation 1.1 to image the subsurface. Constructing the Green's function for the smooth velocity model in Kirchhoff migration only accounts for singly-scattered waves, i.e. primary reflections (first-order Born approximation). This approximation of the Green's function leads to imaging artifacts in the presence of multiples. If the small-scale details of the velocity are known, one can compute the exact Green's function that includes the multiples, thus avoiding these artifacts; however the feasibility of knowing this exact velocity is extremely difficult on a seismic scale. Alternatively, obtaining a smooth version of the velocity (no small-scale details) is a far simpler problem (Chavent and Jacewitz, 1995; Noble et al., 1991; Sava and Biondi, 2004; Symes and Carazzone, 1991).

Traditionally, to image the subsurface using standard imaging methods like Kirchhoff migration, reverse time migration (RTM) (Baysal et al., 1983; McMechan, 1989; Whitmore, 1983) or downward continuation (Claerbout, 1985), one assumes the first-order Born approximation. In order to implement conventional imaging and to ensure the assumption of single scattering holds (to avoid artifacts from multiples), one has to remove multiply reflected waves.

The free surface is the strongest reflector in the Earth, and free-surface multiples are generally stronger than internal multiples. Free-surface multiples can even be as strong as primaries (Weglein and Dragoset, 2007). Therefore the removal of free-surface multiples is generally a priority in the recorded reflection response before using this response for imaging. Methods for the removal of free-surface multiples are extensively described in the literature (Amundsen, 2001; Berkhout and Verschuur, 1997; Lokshtanov, 1999; Verschuur et al., 1992; Weglein et al., 1997; Ziolkowski et al., 1999).

Unlike standard imaging methods, the Marchenko equations construct the Green's function that not only accounts for primary reflections but also multiple reflections. This Green's function (retrieved by the Marchenko equations) is the function G in equation 1.1; it is the field between a point x_0 at the surface and the subsurface point x. Hence imaging the subsurface with the Marchenko Green's functions, which include the primaries and multiples instead of the Green's function that only includes primaries, reduces (if not eliminates) the artifacts caused by multiple reflections. The beauty about the Marchenko equation is that one does not need a physical receiver at the subsurface point x to retrieve the Green's function, hence one calls the subsurface point a *virtual receiver*. The requirements to construct the Green's function are the same as conventional imaging algorithms: the reflection response at the surface and a smooth version of the velocity. Another marvel of the Marchenko equation (applied in geophysics) is that, it locally decomposes the Green's function into corresponding up- and down-going Green's function at the subsurface point x (virtual receiver).

The Marchenko equation is an exact integral equation in 1D that relates the reflection response on one side of the medium to a field inside the medium (Burridge, 1980; Chadan and Sabatier,

2012; Lamb Jr, 1980; Marchenko, 1955). Rose (2002a) iteratively solves the 1D Marchenko equation to focus waves at a point in a 1D medium for a specific time, given the velocity profile is unknown. Since Rose (2002a) used the Marchenko equation for focusing, he requires only the reflection response on one side of the medium. Broggini et al. (2012) extend this focusing principle (Rose, 2002a) to retrieve the 1D Green's function. They realized that the summation of the focusing wavefield and its reflection response is the Green's function of the medium at the specified point of focusing to the surface. Their Green's function include **primaries and internal multiples**. Wapenaar et al. (2012) later extend the Green's function retrieval to 3D, by solving the Marchenko equations in multidimensions. To retrieve these Green's functions, they require the reflection response at the surface with the **free-surface multiples removed** and an estimate of the first arrivals from the focusing point to the surface. The solutions to the Marchenko equation, i.e. the up- and down-going components Green's functions, are used to image the subsurface (Behura et al., 2012; Broggini et al., 2014; Slob et al., 2014; Wapenaar et al., 2011, 2014b).

1.1 Thesis Overview

–In Chapter 2, I extend the Marchenko equation to retrieve the Green's function from a point in the subsurface to the surface in the presence of a free surface. Hence my Green's function includes not only primaries and internal multiples but also free-surface multiples. In comparison to previous work on the Green's function retrieval by the Marchenko equation, the reflection response I use includes free-surface multiples, and therefore, obviates the need to remove free-surface multiples in the reflection response. To retrieve the Green's function in the presence of the free surface I still require the reflection response at the surface and a macro-model of the subsurface overburden velocity (at least between the surface and the virtual source depth level). In this chapter, I show that imaging with the Marchenko-retrieved Green's functions in 1D reduces the imaging artifacts due to multiples compared to standard imaging algorithms like reverse time migration.

In Chapter 3, I simplify the solutions to the Marchenko equation to directly solve for the up- and down-going Green's function. I also extend the imaging with the retrieved Green's functions

to 2D numerical examples.

In Chapter 4, I investigate imaging conditions for the Green's functions that include primaries, internal multiples, and free-surface multiples, called Marchenko imaging. In addition to correlation and deconvolution imaging algorithms using the up- and down-going Green's function (Behura et al., 2012; Broggini et al., 2014; Slob et al., 2014; Wapenaar et al., 2011, 2014b), I propose using the first arrival of the down-going Green's function with the up-going Green's function to image the subsurface. Including the free-surface multiples in the Green's functions obviates the need to remove the free-surface multiples. These multiples can also create artifacts in the imaging step depending on the choice of the imaging condition. These artifacts are non-existent when imaging with the first arrival of the down-going Green's function and the up-going Green's function. In addition, multidimensional deconvolution (MDD) imaging using the up and down-going Green's function closely match the true reflectivity of the subsurface. I obtain similar MDD images, that match the reflectivity, using the up-going and first arrival of the down-going Green's function. I also compare a standard imaging method, reverse time migration, to Marchenko imaging. I conclude that the artifacts in reverse time migration caused by the multiples are reduced (if not eliminated) in Marchenko imaging.

I re-emphasize that the Green's function is retrieved between a virtual receiver (arbitrary subsurface point) and **the acquisition surface**; I take this one step further in Chapter 5; I retrieve the Green's function (both up- and down-going at the virtual receiver) for virtual sources and virtual receivers **in the subsurface**. In this chapter, I modify the Marchenko method so as to not restrict the retrieval of the Green's function at the surface for each virtual source. I propose a new method to retrieve the response of a virtual source at a virtual receiver anywhere **in the subsurface**. I also create snapshots of the wavefield from an arbitrary virtual source. In Chapter 6, I highlight my main contributions and discuss future research ideas concerning the Marchenko equations.

Chapters 2-5 of the thesis have been published in, submitted to, or will soon be submitted to peer-reviewed journals:

Singh, S., R. Snieder, J. Behura, J. van der Neut, K. Wapenaar, and E. Slob, 2015, Marchenko imaging: Imaging with primaries, internal multiples, and free-surface multiples: *Geophysics*, 80, S165-S174.

Singh, S., R. Snieder, J. Thorbecke, J. van der Neut, K. Wapenaar, and E. Slob, 2016, Accounting for free surface multiples in Marchenko imaging: *Geophysics*, submitted.

Singh, S., R. Snieder, 2016, Strategies for imaging with Marchenko Green's functions: *in preparation for Geophysics*

Singh, S., R. Snieder, 2016, Beyond Marchenko – Obtaining virtual receivers and virtual sources in the subsurface: *in preparation for Geophysics*

CHAPTER 2

MARCHENKO IMAGING: IMAGING WITH PRIMARIES, INTERNAL MULTIPLES AND FREE-SURFACE MULTIPLES

Recent work on retrieving the Green's function with the Marchenko equation has shown how these functions for a virtual source in the subsurface can be obtained from reflection data. The response to the virtual source is the Green's function from the location of the virtual source to the surface. The Green's function is retrieved using only the reflection response of the medium and an estimate of the first arrival at the surface from the virtual source. Current techniques, however, only include primaries and internal multiples. Therefore, all surface-related multiples must be removed from the reflection response prior to Green's function retrieval. We extend the Marchenko equation to retrieve the Green's function that includes primaries, internal multiples, and free-surface multiples. In other words, we retrieve the Green's function in the presence of a free surface. The information needed for the retrieval is the same as the current techniques, with the only difference that the reflection response now includes also free-surface multiples. The inclusion of these multiples makes it possible to include them in the imaging operator and it obviates the need for surface-related multiple elimination. This type of imaging with the Green's functions is called Marchenko imaging.

2.1 Introduction

To focus a wavefield at a point in a medium only requires surface reflection data and an estimate of the first arriving wave at the surface from a point source at the focusing location (Broggini and Snieder, 2012; Broggini et al., 2012; Wapenaar et al., 2013a). Unlike in seismic interferometry (Bakulin and Calvert, 2006; Wapenaar and Fokkema, 2006), no receiver is required at the desired focusing location, i.e. the virtual source location, and single-sided illumination suffices. Significantly, the detailed medium parameters need not be known to focus the wavefield as opposed to the time-reversal method, which requires the knowledge of detailed medium parameters and enclosing

boundaries for correct focusing. However, the travel-time of the direct-arrival of the virtual source to the surface is required for Green's function retrieval. To obtain an estimate of this traveltime, one only needs a macro-model of the velocity.

The focusing scheme of Broggini et al. (2012), Broggini and Snieder (2012), and Wapenaar et al. (2013a) are extensions of the algorithm of Rose (2002a,b) who shows an iterative scheme that solves the Marchenko equation for wavefield focusing in one dimension. The focused events in the wavefield for the virtual source consist of primaries and internal multiples (Wapenaar et al., 2013a) but not free-surface multiples. Importantly, Rose (2002a,b) derived the focusing method for single-sided illumination with sources and receivers on one side of the medium, similar to current geophysical acquisition methods.

Wapenaar et al. (2011) illustrate imaging with the Green's function in 1D and also discuss how to image in multi-dimensions (2D and 3D). Similarly, Behura et al. (2012) introduce a correlation-imaging algorithm based on the Green's function retrieval scheme that images not only primaries but also internal multiples. Broggini et al. (2014) extend the work of Behura et al. (2012) by using multidimensional deconvolution (MDD) as the imaging condition in place of conventional cross-correlation or deconvolution, which further reduces the artifacts. Central in these methods is the retrieval of the Green's function from the acquisition surface to any point in the medium. This Green's function is essentially a redatuming or downward continuation operator. Since this Green's function includes both primaries and internal multiples, we expect improved subsurface images compared to using primaries alone.

We summarize our work in Figure 2.1. In this paper, any variable with a subscript 0 (e.g., R_0) indicates that no free-surface is present. As shown in Figure 2.1, prior to the algorithm of Broggini et al. (2012), one must remove the free-surface multiples from the reflection response of the medium (solid up-going arrow) to retrieve the Green's function. The removal of the free-surface multiples can be achieved by Surface Related Multiple Elimination (SRME) (Verschuur et al., 1992). In our study, we modify the earlier focusing algorithms (Broggini et al., 2012; Rose, 2002a; Wapenaar et al., 2013a) to focus not only primaries and internal multiples but also the free-

surface multiples; this is labeled "**Our Work**" in Figure 2.1. We achieve such focusing using the reflection response R in the presence of a free surface and an estimate of the first arrival from the focus location to the surface. Notably, our proposed Green's function retrieval scheme obviates the need for SRME (see Figure 2.1) to construct the Green's function.

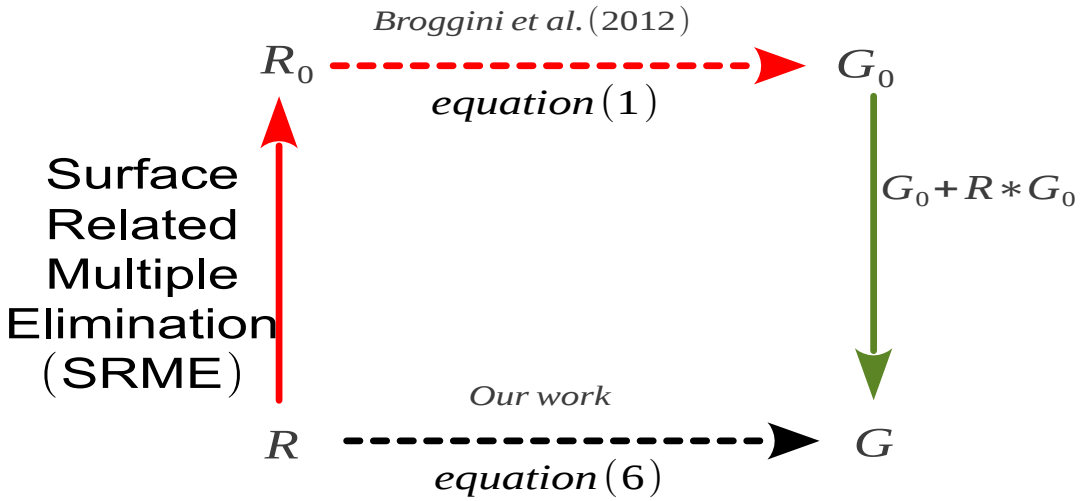

Figure 2.1: Overview of the methods to focus the wavefield using an iterative approach. R denotes reflected waves recorded at the surface in the presence of a free surface, and R_0 is the reflection response for a medium without a free surface. G is the Green's function at the surface for a virtual source located at a point in the medium in the presence of a free surface and G_0 is the Green's function in the absence of a free surface. The two dashed arrows indicate separate iterative schemes.

The free surface is the strongest reflector in the system; therefore, in general, the free-surface multiples are stronger than internal multiples. In addition, free-surface multiples can be used to provide better illumination, higher fold, and better vertical resolution of the subsurface (Jiang et al., 2007; Muijs et al., 2007a,b; Schuster et al., 2003). For these reasons, by retrieving the Green's function, which includes primaries and all multiples (including free-surface multiples), and using the imaging condition proposed by Behura et al. (2012) and by Broggini et al. (2014), we expect better imaging of the subsurface.

2.2 Theory

In this section we derive the main equations for the retrieval of the Green's function in the presence of a free-surface, with the detailed derivations in the Appendix. We first summarize existing theory that this paper is building on.

The theory of focusing the wavefield without a free surface, i.e. retrieving the Green's function G_0 from R_0, is covered by Rose (2002a), Broggini et al. (2012), and Wapenaar et al. (2013a). As summarized in Figure 2.1, we have to remove the free-surface multiples from the reflection response R (for instance by SRME) to get R_0 and then compute G_0, the Green's function in the absence of the free surface.

Wapenaar et al. (2004a) showed that we can relate the transmission operators for media with and without the free surface. Similarly, we can retrieve G (the Green's function in the presence of the free surface) from G_0 in the frequency domain with the expression

$$G(\mathbf{x_i'}, \mathbf{x_0}, \omega) = G_0(\mathbf{x_i'}, \mathbf{x_0}, \omega) - \int_{\partial D_0} G_0(\mathbf{x_i'}, \mathbf{x}, \omega) R(\mathbf{x}, \mathbf{x_0}, \omega) d\mathbf{x}, \tag{2.1}$$

where ∂D_0 is the acquisition surface, $\mathbf{x_0}$ and $\mathbf{x_i'}$ are spatial positions along ∂D_0 and ∂D_i (an arbitrary depth level, below ∂D_0), and R is the reflection response for a down-going incident wavefield at ∂D_0. The arbitrary depth levels are defined in the same way as in the work of Wapenaar et al. (2004a). In our case, we replace the transmission responses (in Equation 22 of Wapenaar et al. (2004a)) with the corresponding Green's functions, G or G_0, since the Green's function is the total transmitted wavefield from the focusing point to the surface. Note that this approach, $R \rightarrow R_0 \rightarrow G_0 \rightarrow G$, follows the tortuous path shown in Figure 2.1. We can, however, retrieve the Green's function in the presence of the free surface directly from the measured reflection data $R \rightarrow G$ (Figure 2.1, black dashed arrow).Therefore, $R \rightarrow G$ avoids SRME and the retrieval of G_0. We generalize the formulation of Wapenaar et al. (2013a) ($R_0 \rightarrow G_0$) to include free-surface multiples ($R \rightarrow G$); the detailed mathematics of this retrieval is documented in the appendix. The reflections from the free surface are included in the focusing scheme, similar to the treatment by Wapenaar et al. (2004a) of free-surface multiples.

We define our spatial coordinates by their horizontal and depth components, for instance $\mathbf{x_0} = (\mathbf{x_H}, x_{3,0})$, where $\mathbf{x_H}$ denotes the horizontal coordinates (x_1, x_2) at a depth $x_{3,0}$. We define solutions of the wave equation that focus at a point in a medium, and refer to these as the focusing functions f_1 and f_2. The f_1 function involves waves that focus at $\mathbf{x_i'}$ at a defined depth level (∂D_i) for incoming and outgoing waves at the acquisition surface (∂D_0) at $\mathbf{x_0}$ (Figure 2.2(a)). The function f_2 is a solution for waves that focus just above ∂D_0 at $\mathbf{x_0''}$ for incoming and outgoing waves at ∂D_i (Figure 2.2(b)).

The focusing functions are auxiliary wavefields which exist in a reference medium that has the same material properties as the actual inhomogeneous medium between ∂D_0 and ∂D_i and that is homogeneous above ∂D_0 and reflection-free below ∂D_i (Slob et al., 2014). Therefore, the boundary conditions on ∂D_0 and ∂D_i in the reference medium, where the focusing function exists, are reflection-free.

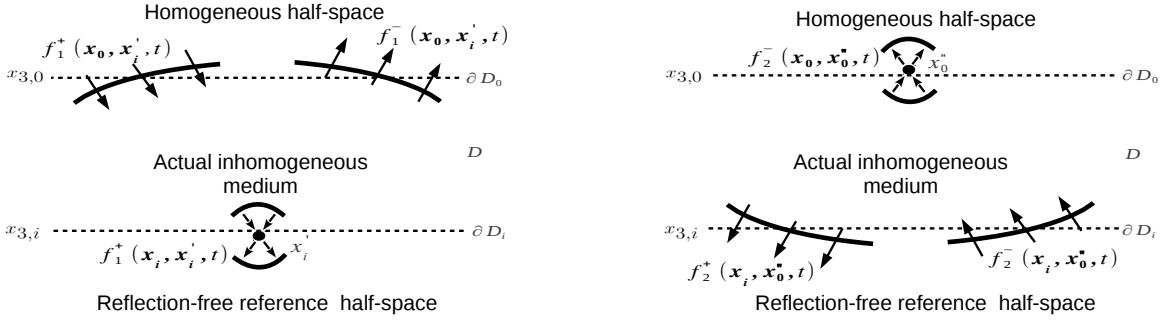

Figure 2.2: (a) Focusing function f_1 that focuses at $\mathbf{x_i'}$. and (b) Focusing function f_2 that focuses at $\mathbf{x_0''}$.

Note that this boundary condition need not be the same as the actual medium. The focusing functions can be separated into up-going and down-going waves; the first focusing function in the frequency domain reads

$$f_1(\mathbf{x}, \mathbf{x_i'}, \omega) = f_1^+(\mathbf{x}, \mathbf{x_i'}, \omega) + f_1^-(\mathbf{x}, \mathbf{x_i'}, \omega), \tag{2.2}$$

while the second focusing function reads

$$f_2(\mathbf{x}, \mathbf{x}''_{\mathbf{0}}, \omega) = f_2^+(\mathbf{x}, \mathbf{x}''_{\mathbf{0}}, \omega) + f_2^-(\mathbf{x}, \mathbf{x}''_{\mathbf{0}}, \omega). \tag{2.3}$$

In this paper the superscript $(+)$ refers to down-going waves and $(-)$ to up-going waves at the observation point $\mathbf{x}$.

Table 2.1 and Figure 2.2(a) show the one-way wavefields for the f_1 function at the depth levels ∂D_0 and ∂D_i, which we define in wave state A. We call these waves one-way because locally these fields are strictly up- or down-going at the observation point however their coda will include both up- and down-going waves.

Table 2.1: One-way wavefields of the focusing function f_1 at the acquisition surface ∂D_0 and the level where f_1 focuses, ∂D_i. $p_A^{\pm}$ symbolizes one-way wavefields in the frequency domain, at arbitrary depth levels in the reference medium, see Figure 2.2(a).

On ∂D_0:	$p_A^+ =$	$f_1^+(\mathbf{x_0}, \mathbf{x'_i}, \omega)$,	
	$p_A^- =$	$f_1^-(\mathbf{x_0}, \mathbf{x'_i}, \omega)$.	
On ∂D_i:	$p_A^+ =$	$f_1^+(\mathbf{x_i}, \mathbf{x'_i}, \omega)$	$= \delta(\mathbf{x}_H - \mathbf{x}'_H)$,
	$p_A^- =$	$f_1^-(\mathbf{x_i}, \mathbf{x'_i}, \omega)$	$= 0$.

The focusing function $f_1^+(\mathbf{x}, \mathbf{x'_i}, t)$ is shaped such that $f_1(\mathbf{x}, \mathbf{x'_i}, t)$ focuses at $\mathbf{x'_i}$ at $t = 0$. At the focusing depth level ∂D_i of f_1, we define $f_1(\mathbf{x}, \mathbf{x'_i}, t)$ as $\delta(\mathbf{x}_H - \mathbf{x}'_H)\delta(t)$, a two-dimensional (2D) and 1D Dirac delta function in space and time respectively, see Figure 2.2(a) and Table 2.1. Below the focusing depth level, $f_1(\mathbf{x}, \mathbf{x'_i}, t)$ continues to diverge as a down-going field $f_1^+(\mathbf{x}, \mathbf{x'_i}, t)$ into the reflection-free reference half-space.

Similarly, Table 2.2 and Figure 2.2(b) show the one-way wavefields for the f_2 function at the depth levels ∂D_0 and ∂D_i.

In this case, $f_2^-(\mathbf{x}, \mathbf{x}''_{\mathbf{0}}, t)$ is shaped such that the function $f_2(\mathbf{x}, \mathbf{x}''_{\mathbf{0}}, t)$ focuses at $\mathbf{x}''_{\mathbf{0}}$ at $t = 0$. At the focusing depth level ∂D_0 of f_2, we define $f_2(\mathbf{x}, \mathbf{x}''_{\mathbf{0}}, t)$ as $\delta(\mathbf{x}_H - \mathbf{x}''_H)\delta(t)$, see Figure 2.2(b) and Table 2.2. After focusing, $f_2(\mathbf{x}, \mathbf{x}''_{\mathbf{0}}, t)$ continues to diverge as an up-going field $f_2^-(\mathbf{x}, \mathbf{x}''_{\mathbf{0}}, t)$ into the homogeneous upper half-space.

Table 2.2: One-way wavefields of the focusing function f_2 at the depth level ∂D_0 and ∂D_i. $p_A^{\pm}$ symbolizes one-way wavefields in the frequency domain, at arbitrary depth levels in the reference medium, see Figure 2.2(b).

On ∂D_0:	$p_A^+ =$	$f_2^+(\mathbf{x_0}, \mathbf{x_0''}, \omega) \quad = 0,$
	$p_A^- =$	$f_2^-(\mathbf{x_0}, \mathbf{x_0''}, \omega) \quad = \delta(\mathbf{x}_H - \mathbf{x}_H'').$
On ∂D_i:	$p_A^+ =$	$f_2^+(\mathbf{x_i}, \mathbf{x_0''}, \omega),$
	$p_A^- =$	$f_2^-(\mathbf{x_i}, \mathbf{x_0''}, \omega).$

The focusing functions are independent of the surface boundary condition of the actual medium as these functions reside only in the reference medium. If the medium were homogeneous, the focusing function f_2 would consist of the time-reversed direct wave between the focal point and ∂D_i. However, in an inhomogeneous medium the focusing function f_2 consists of the time-reversed direct wave and the coda M following the time-reversed direct wave. The coda M consists of the scattered waves that result when the time-reversed direct wave transmits through the medium to the focus point.

In the frequency domain, the focusing function f_2 is related to the Green's function G_0 of the actual inhomogeneous medium without a free surface by (Wapenaar et al., 2013a):

$$G_0(\mathbf{x_i}', \mathbf{x_0''}, \omega) = f_2(\mathbf{x_i}', \mathbf{x_0}'', \omega)^* + \int_{\partial D_0} f_2(\mathbf{x_i}', \mathbf{x_0}, \omega) R_0(\mathbf{x_0}, \mathbf{x_0}'', \omega) d\mathbf{x_0}, \tag{2.4}$$

where * represents the complex conjugate. In the situation without the free surface, we ignore the downward reflected waves at the acquistion level i.e., the free surface multiples. In the actual inhomogeneous medium, in the presence of a free surface, we account for the waves reflecting from the free surface (details are given in the Appendix; as shown in equation A.5). For this situation, the one-way wavefields are shown in Table 2.3 and Figure 2.3. We define wave state B as the acoustic state with the wavefields of the actual medium (Wapenaar et al., 2013a).

We can use the one-way reciprocity theorems of the convolution and correlation type for flux-normalized one-way wave fields (Wapenaar and Grimbergen, 1996)

$$\int_{\partial D_0} [p_A^+ p_B^- - p_A^- p_B^+] d\mathbf{x_0} = \int_{\partial D_i} [p_A^+ p_B^- - p_A^- p_B^+] d\mathbf{x_i},$$

Table 2.3: One-way wavefields in the actual inhomogeneous medium in the presence of a free surface at the depth level ∂D_0 and ∂D_i. $p_B^{\pm}$ symbolizes one-way wavefields at arbitrary depth levels in the inhomogeneous medium, while r is the reflection coefficient of the free surface, see Figure 2.3.

On ∂D_0:	$p_B^+ =$	$G^+(\mathbf{x_0}, \mathbf{x_0''}, \omega) =$	$\delta(\mathbf{x_H} - \mathbf{x_H''}) + rR(\mathbf{x_0}, \mathbf{x_0''}, \omega),$
	$p_B^- =$	$G^-(\mathbf{x_0}, \mathbf{x_0''}, \omega) =$	$R(\mathbf{x_0}, \mathbf{x_0''}, \omega).$
On ∂D_i:	$p_B^+ =$	$G^+(\mathbf{x_i}, \mathbf{x_0''}, \omega),$	
	$p_B^- =$	$G^-(\mathbf{x_i}, \mathbf{x_0''}, \omega).$	

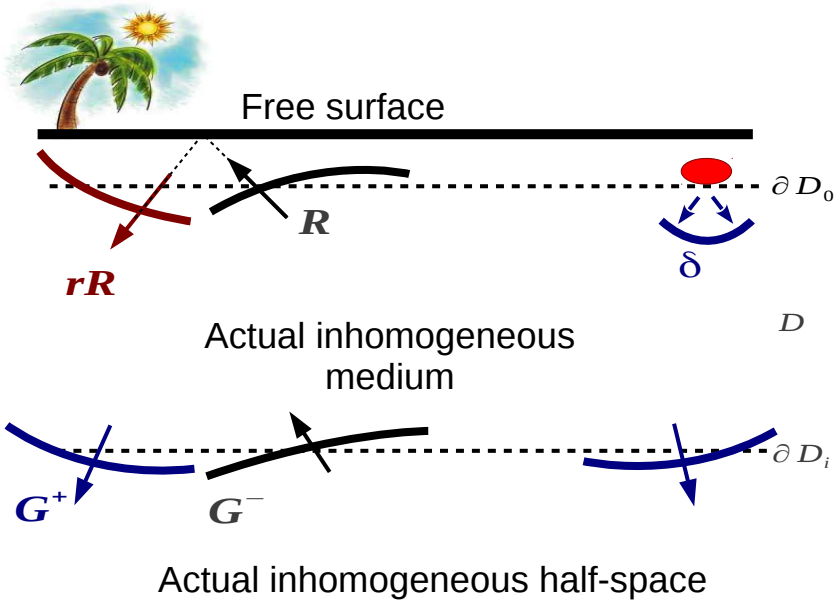

Figure 2.3: One-way Green's functions in the actual inhomogeneous medium in the presence of a free surface at the acquisition surface ∂D_0 and the arbitrary surface ∂D_i. These are the quantities that are used in the reciprocity theorems. The tree indicates the presence of the free surface.

$$\int_{\partial D_0} [(p_A^+)^* p_B^+ - (p_A^-)^* p_B^-] d\mathbf{x_0} = \int_{\partial D_i} [(p_A^+)^* p_B^+ - (p_A^-)^* p_B^-] d\mathbf{x_i}, \tag{2.5}$$

respectively, to relate the one-way wavefields between the two focusing functions (f_1 and f_2) and the one-way wavefields between the focusing functions and the actual medium. $p_A^{\pm}$ and $p_B^{\pm}$ are the one-way wavefields of the focusing functions and the actual medium respectively, in the frequency domain. As shown in the appendix, the corresponding two-way Green's function in the presence of the free surface is related to the focusing function f_2 by

$$\begin{aligned} G(\mathbf{x_i}', \mathbf{x_0}'', \omega) = f_2(\mathbf{x_i}', \mathbf{x_0}'', \omega)^* + & \int_{\partial D_0} f_2(\mathbf{x_i}', \mathbf{x_0}, \omega) R(\mathbf{x_0}, \mathbf{x_0}'', \omega) d\mathbf{x_0} \\ & + r \int_{\partial D_0} f_2(\mathbf{x_i}', \mathbf{x_0}, \omega)^* R(\mathbf{x_0}, \mathbf{x_0}'', \omega) d\mathbf{x_0}, \end{aligned} \tag{2.6}$$

where, for simplicity, we assume the reflection coefficient of the free surface satisfies $r = -1$. The two-way Green's function is defined as the superposition of the down- and up-going fields, according to

$$G(\mathbf{x}, \mathbf{x_0}'', \omega) = G^+(\mathbf{x}, \mathbf{x_0}'', \omega) + G^-(\mathbf{x}, \mathbf{x_0}'', \omega). \tag{2.7}$$

Using reciprocity, the Green's functions on the left-hand sides of equations 2.4 and 2.6 can be interpreted as the response to a virtual source at $\mathbf{x_i}'$ for the situation without and with a free-surface, respectively. To yield equations 2.4 and 2.6 we use one-way reciprocity relations (details are given in the appendix for the retrieval of G, equation A.5). Note the up-going Green's function (G^-) in the actual inhomogeneous medium at ∂D_0 is the reflection response R for a downward radiating source at ∂D_0.

Equation 2.6 differs from equation 2.4 in two ways. First, the last term on the right hand side of equation 2.6 accounts for the waves that are reflected off the free surface. Second, equation 2.6 contains the reflection response R for a medium with a free surface, while expression 2.4 contains the reflection response R_0 for a medium without a free surface.

Similar to our treatment of the focusing function f_2, we can define another focusing function g_2 such that

$$g_2(\mathbf{x}, \mathbf{x_0''}, \omega) = f_2^+(\mathbf{x}, \mathbf{x_0''}, \omega) - f_2^-(\mathbf{x}, \mathbf{x_0''}, \omega). \tag{2.8}$$

We use g_2 to obtain a difference Green's function $\widetilde{G}$ which is similar to expression 2.6

$$\begin{aligned}\widetilde{G}(\mathbf{x_i'}, \mathbf{x_0''}, \omega) = -g_2(\mathbf{x_i'}, \mathbf{x_0''}, \omega)^* + & \int_{\partial D_0} g_2(\mathbf{x_i'}, \mathbf{x_0}, \omega) R(\mathbf{x_0}, \mathbf{x_0''}, \omega) d\mathbf{x_0} \\ - \ r & \int_{\partial D_0} g_2(\mathbf{x_i'}, \mathbf{x_0}, \omega)^* R(\mathbf{x_0}, \mathbf{x_0''}, \omega) d\mathbf{x_0}.\end{aligned} \tag{2.9}$$

We call $\widetilde{G}$ the difference Green's function since

$$\widetilde{G}(\mathbf{x_i'}, \mathbf{x_0''}, \omega) = G^+(\mathbf{x_i'}, \mathbf{x_0''}, \omega) - G^-(\mathbf{x_i'}, \mathbf{x_0''}, \omega), \tag{2.10}$$

and it is used to obtain the up- and down-going Green's functions by combining it with G in equation 2.7.

To yield the up-going Green's function, we subtract equations 2.7 and 2.10:

$$G^-(\mathbf{x_i'}, \mathbf{x_0''}, \omega) = \frac{1}{2}[G(\mathbf{x_i'}, \mathbf{x_0''}, \omega) - \widetilde{G}(\mathbf{x_i'}, \mathbf{x_0''}, \omega)]. \tag{2.11}$$

Similarly, we obtain the down-going Green's function by adding equations 2.6 and 2.10:

$$G^+(\mathbf{x_i'}, \mathbf{x_0''}, \omega) = \frac{1}{2}[G(\mathbf{x_i'}, \mathbf{x_0''}, \omega) + \widetilde{G}(\mathbf{x_i'}, \mathbf{x_0''}, \omega)]. \tag{2.12}$$

These up- and down-going (G^- and G^+) Green's functions at the focal point are used for imaging (Marchenko imaging) and include primaries and all multiples. Up- and down-going Green's functions have been used for imaging the subsurface, (Behura et al., 2012; Broggini et al., 2012, 2014; Wapenaar et al., 2011). However, their Green's functions only contain primaries and internal multiples. In this paper, the up- and down-going Green's functions also include free-surface multiples.

The use of up- and down-going wavefields for imaging is not a new principle. Claerbout (1971), Wapenaar et al. (2000) and Amundsen (2001) have shown that one can get the reflection response below an arbitrary depth level once the up- and down-going wavefields are available. The

governing equation that relates the up- and down-going Green's function is

$$G^{-}(\mathbf{x_i}^{'}, \mathbf{x_0}^{''}, t) = \int_{\partial D_i} d\mathbf{x_i} \int_{-\infty}^{\infty} G^{+}(\mathbf{x_i}, \mathbf{x_0}^{''}, t - t') R_0(\mathbf{x_i}^{'}, \mathbf{x_i}, t') dt', \tag{2.13}$$

where ∂D_i is an arbitrary depth level, and R_0 is the reflection response of the medium below ∂D_i. In addition, R_0 at ∂D_i contains no reflections from above this depth level. We can think of R_0 as the reflection response of a truncated medium; where the truncated medium is the same as the true medium below ∂D_i and reflection free above. Equation 2.13 states that G^{-} is represented by the convolution of G^{+} with R_0 and integration along all source positions $\mathbf{x}'$ of R_0.

We solve for R_0 by multidimensional deconvolution (van der Neut et al., 2011) as the time integral is a convolution. The subsurface image is subsequently obtained by taking the zero lag of R_0, i.e. taking $t = 0$ at each depth level in the model and at zero offset, $\mathbf{x_i} = \mathbf{x_i'}$, (for each ∂D_i), this is called the zero-offset imaging condition. Alternatively, once we obtain R_0 at an arbitrary ∂D_i we can also apply a standard imaging procedure, for instance, downward continuation, to image below ∂D_i. This is because R_0 is the reflection response of the truncated medium below ∂D_i for sources and receivers at ∂D_i.

2.3 Numerical Examples

We use three numerical examples that show the retrieval of the Green's functions and imaging using the associated Green's functions.

We first consider a 1D model that has a high impedance layer generic to salt models as shown in Figure 2.4. A receiver at the surface records the reflected waves. To retrieve the Green's function in 1D, one needs the travel time of the first arriving wave from the virtual source to the surface. The travel time of the first arriving wave is used to temporally separate the Green's function from the focusing solution f_2 in the time-domain representation of equation 2.6. To obtain the focusing function f_2, we evaluate expression 2.6 for a time earlier than the first arriving wave and setting the left-hand side of equation 2.6 to zero. The remaining expression is an equation for f_2 which is solved iteratively (details are given in the appendix, equations A.6 to A.10).

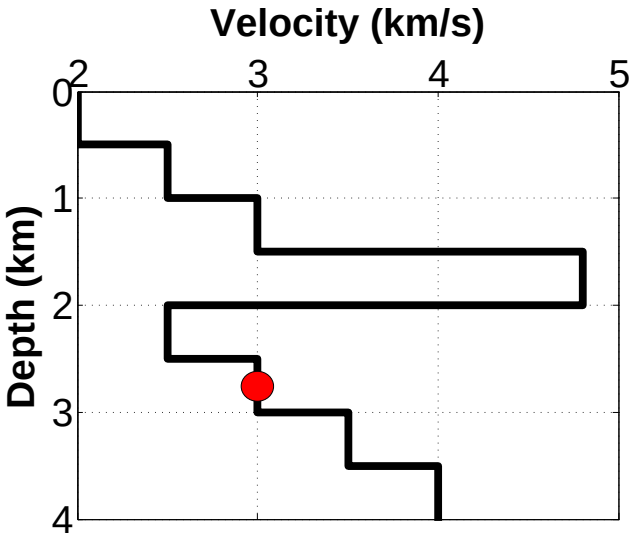

Figure 2.4: Velocity model with high impedance layer at 1.5 km; the dot is the position of the virtual source.

Once the focusing solution has been found (see Figure 2.5), it is substituted in equation 2.6 to retrieve the Green's function (for this example, the Green's function is the response to the virtual source at a depth of 2.75 km, [dot in Figure 2.4], recorded at the surface), Figure 2.6. This Green's function G, arbitrarily scaled to its maximum amplitude (see Figure 2.6), is the response at the surface ∂D_0 to the virtual source.

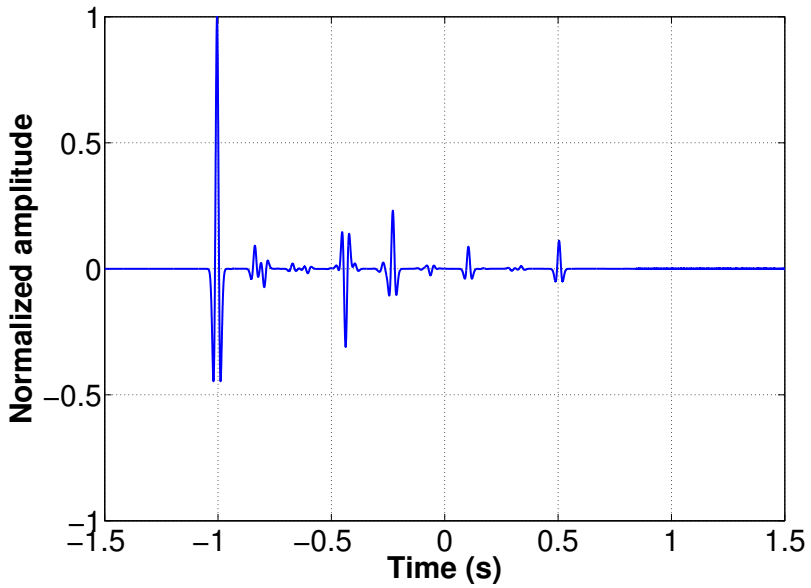

Figure 2.5: Focusing function f_2 at depth 2.75 km for the velocity model in Figure 2.4

.

We also model the Green's function using finite differences to verify that the Green's function retrieved from our algorithm is accurate, and superimposed this result on Figure 2.6. The vertical scale of Figure 2.6 is enlarged to better illustrate the model and retrieved Green's function. For this reason, the first arrival at time 1.0 s is clipped. The difference between the modeled and the retrieved Green's function is negligible relative to the average amplitude of the Green's function, as seen in Figure 2.6. The arrivals caused by the free surface are shown in Figure 2.7 compared to the arrivals in the absence of a free surface.

The corresponding image of the model in Figure 2.4 shown in Figure 2.8 illustrates the correct location of the reflectors as well as the correct scaled reflection coefficient. In 1D, the image we obtain is the deconvolution of the up- and down-going Green's function for $t = 0$ at each

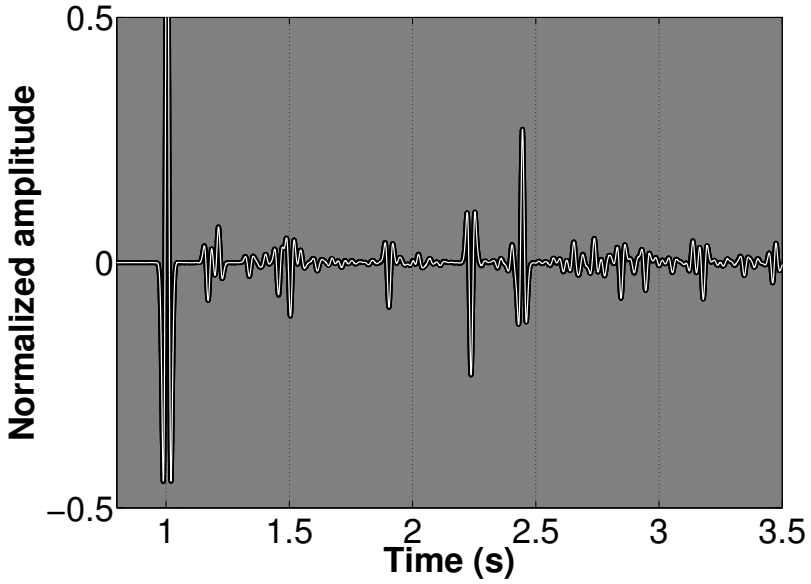

Figure 2.6: Retrieved Green's function (normalized by maximum amplitude), G, from a depth of 2.75 km to the surface (white). The modeled Green's function is displayed (in black) in the background. The Green's functions are associated to the model in Figure 2.4.

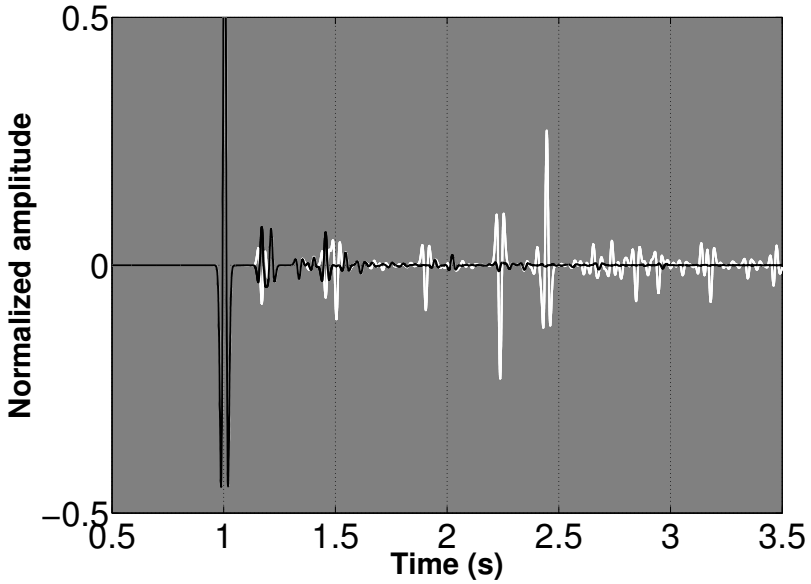

Figure 2.7: Impact of the free surface. Black line: the Green's function in a medium without a free surface G_0, and white line is the difference between G and G_0, therefore the white line shows events that are caused by the presence of the free surface.

image point, Claerbout (1985). There are some anomalous amplitudes in the Marchenko image (especially around 200 m) but they are small compared to the actual reflectors' amplitude and are attributed to the deconvolution imaging condition.

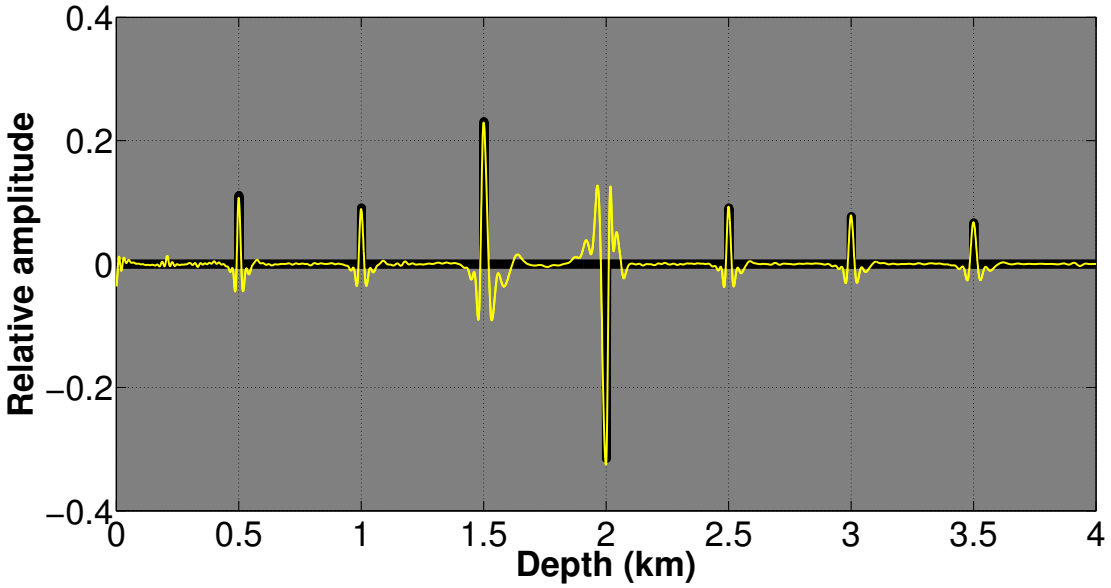

Figure 2.8: Marchenko imaging of Figure 2.4 in white, with the true reflectivity (in black) in the background.

The model for the next example is taken from Weglein and Dragoset (2007), where the second primary event cancels with the free surface multiple from the first reflector. We demonstrate with this numerical example the retrieval of the Green's function (as well as its associated up- and down-going Green's function) at depth 1000m for the model shown in Figure 2.9. Figure 2.10 illustrates some of the reflected events corresponding to this model. The associated reflected waves at the acquisition level, shown in Figure 2.11, are recorded 5m below the free surface. As is shown in Figure 2.11 and Figure 2.10, the second primary event P_2 is canceled by the free-surface multiple F_1 at 1.0 s, and the other events (internal multiples and free surface multiples) interfere destructively with each other at later times.

The Green's function for a source at depth 1000m is shown in Figure 2.12. The corresponding up- and down-going Green's function at depth 1000 m is illustrated in Figure 2.13 and Figure 2.14, respectively. The computed travel times for this simple model of the up- and down-going Green's

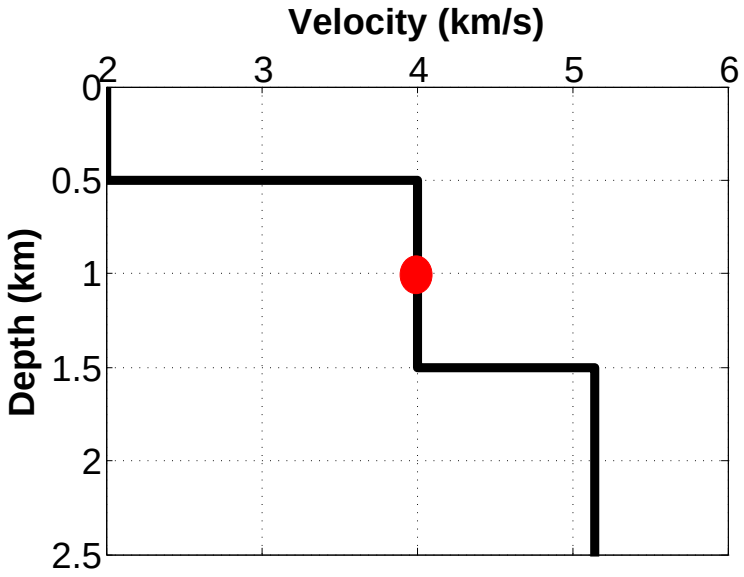

Figure 2.9: Simple velocity model where the dot indicates the position of one virtual source at depth 1000 m.

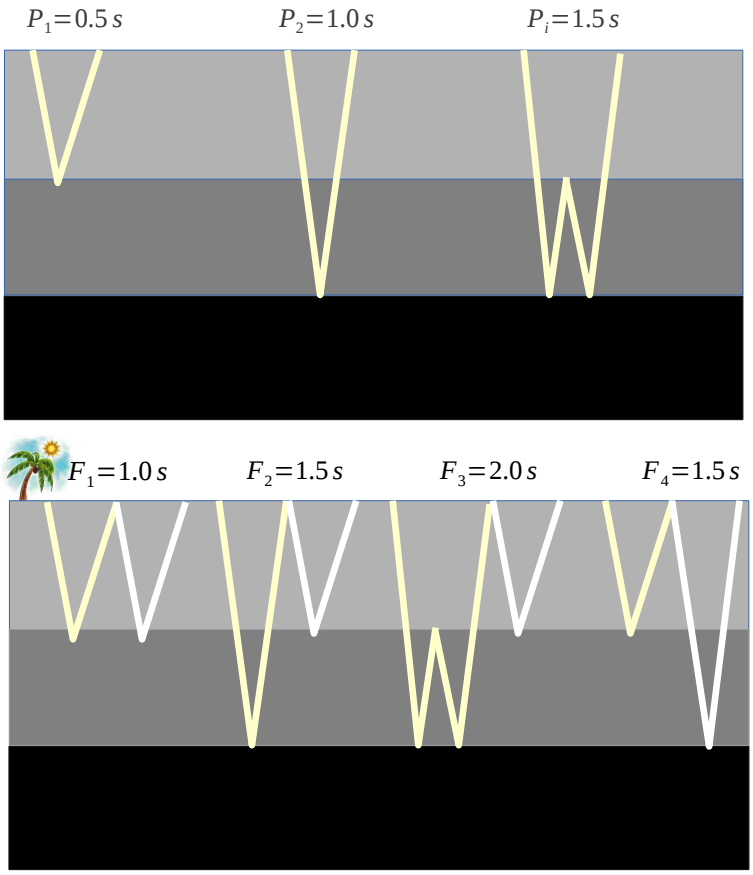

Figure 2.10: Sketch of some events that occur in the velocity model in Figure 2.9.

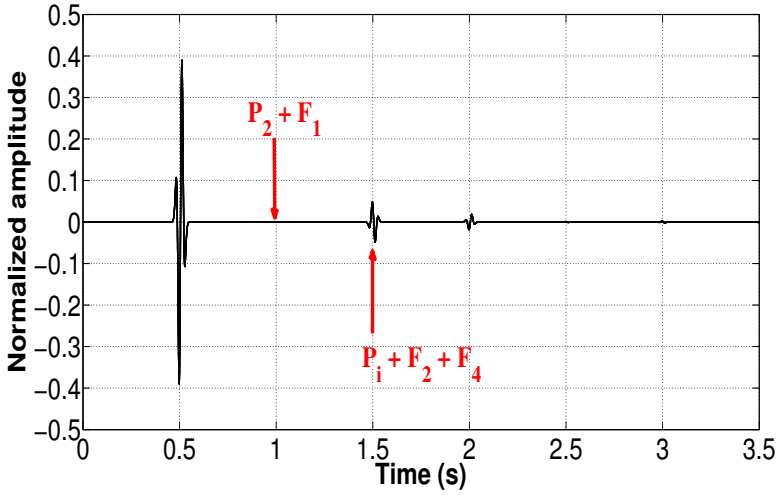

Figure 2.11: Reflection response with the direct waves removed (The events are scaled by the direct wave magnitude), labels are referenced to Figure 2.10.

function in Figure 2.15 correspond to the travel times of the events in the retrieved up- and down-going Green's functions; hence confirming our decomposition of the Green's function into its associated up- and down-going wavefields.

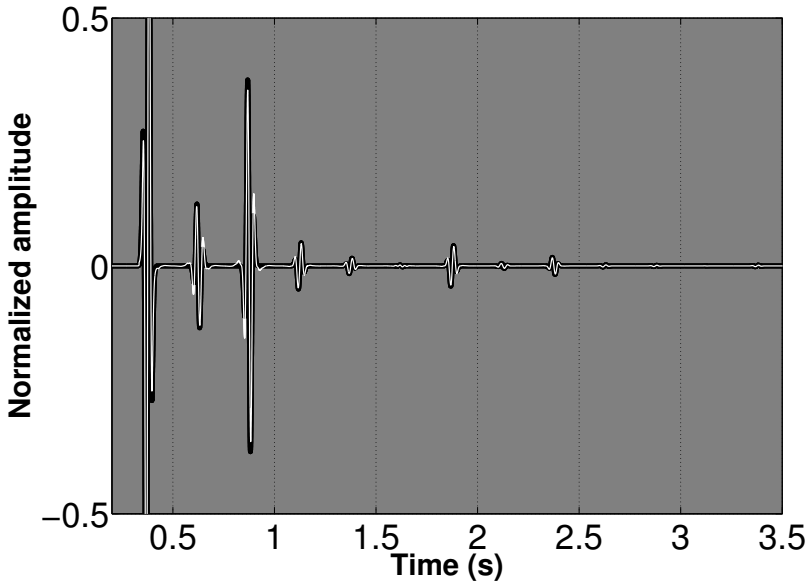

Figure 2.12: Green's function with virtual source at depth 1000 m and recording at the surface. The black thicker line is the modeled Green's function, superimposed on it is the retrieved Green's function. The plot limits are chosen between 0.5 to -0.5 normalized amplitude to visualize the smaller amplitude events better.

Figure 2.12 has an event at 0.6 seconds, which is the reflection of the virtual source field from the second layer recorded at the surface. Hence, the Green's function retrieval algorithm correctly detects the missing reflector in the recorded waves. In the 1D model considered here, equation 2.13, reduces to the deconvolution of the up-going Green's function with the down-going Green's function at every point in the velocity model yielding the correct positioning of the reflectors (see Figure 2.16) as well as the correct scaled reflection coefficient. Furthermore, the image is free of artifacts originating from surface-related and internal multiples. Importantly, the difference between the analysis of Weglein and Dragoset (2007) and our work is that they removed the multiples at the surface, while we derived the Green's function for a virtual source in the subsurface and, subsequently, a multiple-free image.

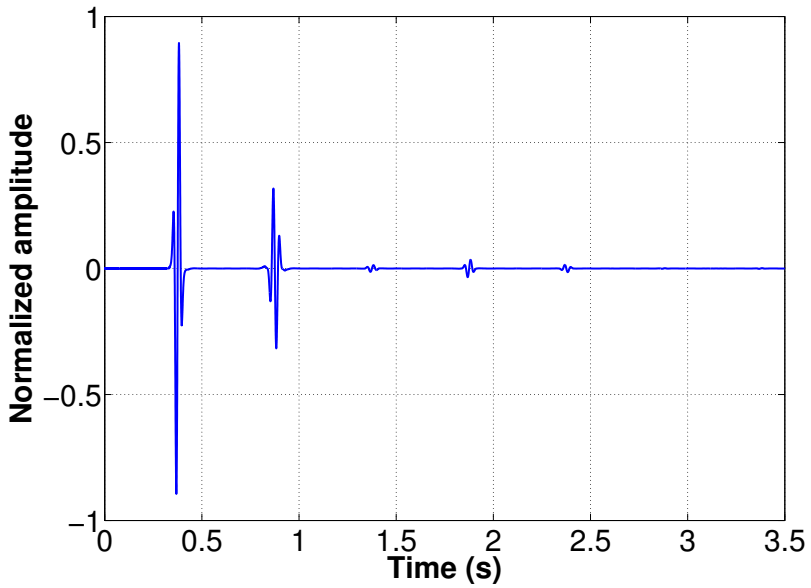

Figure 2.13: The Green's function for up-going waves at the virtual source location (1000 m) and recording at the surface for the velocity in model in Figure 2.9.

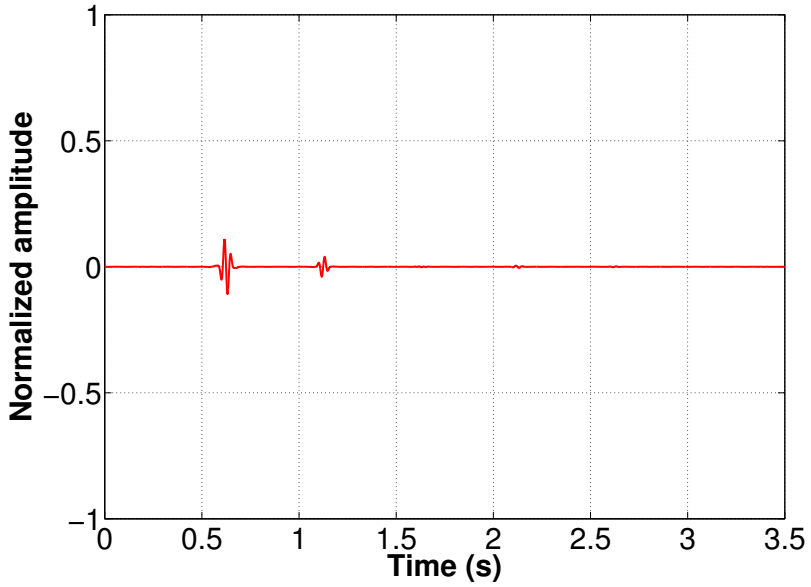

Figure 2.14: The Green's function for down-going wave at the virtual source location (1000 m) and recording at the surface for the velocity in model in Figure 2.9.

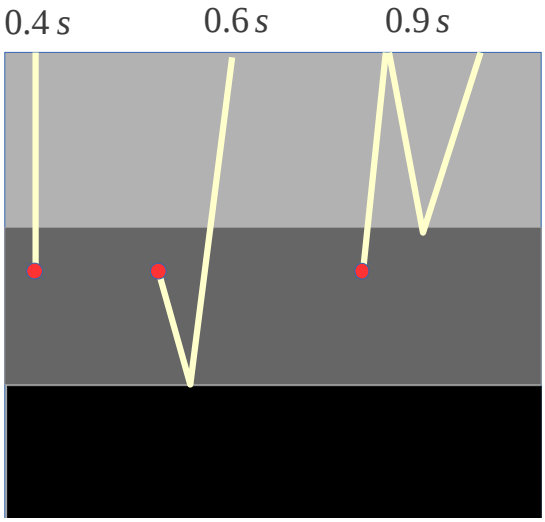

Figure 2.15: Sketch of some events that are present in the Green's function from the virtual source (grey dot) at 1000m and recorded at the surface for the velocity in model in Figure 2.9.

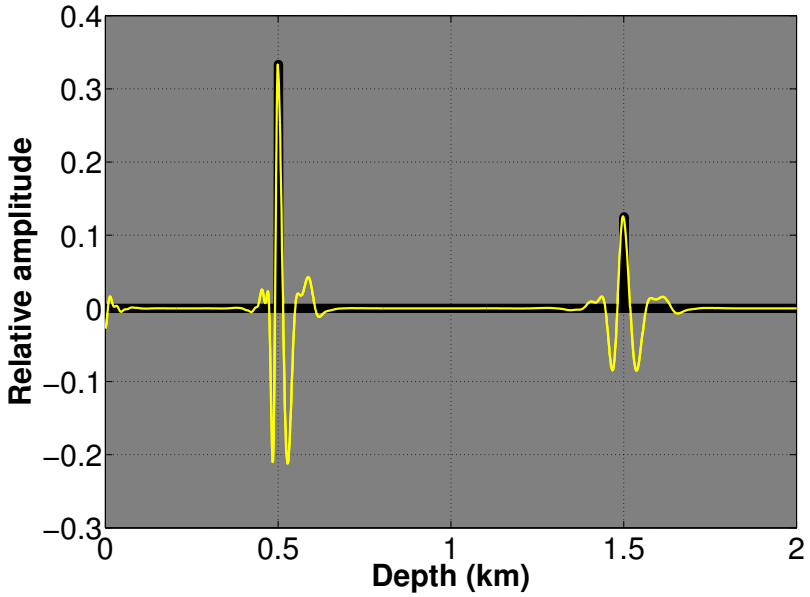

Figure 2.16: Image of the velocity model, Figure 2.9, after Marchenko imaging with the reflectivity overlain (in black).

2.4 Discussion

The new feature of our Green's function retrieval scheme compared to the earlier presented schemes is that we include the free-surface multiples in our Green's function. Hence we do not need to remove the free-surface multiples from our reflection response. For our 1D numerical examples, we can identify the events that are caused by the presence of the free surface (black line in Figure 2.7) by computing the difference of G and G_0.

The arrivals that are caused by the free surface (black line in Figure 2.7) have higher amplitude and greater waveform complexity compared to the events in the response without a free surface G_0 (white line in Figure 2.7). This supports our conjecture that using the additional events and energy that free-surface reflections provide, can benefit imaging of the subsurface, i.e. imaging using G rather than G_0.

In our scheme to retrieve the Green's function we require that the wavelet is removed from the reflection response (which can be done by deconvolution). In addition, we assume that the reflection response is due to a down-going source. However in the marine case the source is generally placed a few meters below the surface, therefore there is not only a down-going component of the source, but also an up-going component. In such situations, we consider the source wavelet to also include the up-going component of the source. Consequently, the wavelet with which we deconvolve the reflection response at the surface is no longer that of a monopole source but of a dipole source.

Although we show 1D examples, all equations are multidimensional. In 2D or 3D media, a smooth version of the slowness (1/velocity) can be used to get an estimate of the direct arriving wave from the virtual source to the surface, but the small scale details of the velocity and density need not be known. The direct arriving wave can be obtained using finite-difference modeling of the waveforms. In 1D, a velocity model is not necessary unless we want a depth image as in the examples we show in this paper.

We have also briefly investigated Marchenko imaging when the reflection response is corrupted with noise. In such noisy cases, the noise level in the reflection response and the Marchenko image

are similar although our Green's function retrieval algorithm is non-linear. However, further investigation is needed to properly understand the accuracy of Marchenko imaging when the reflection response is corrupted with noise.

2.5 Conclusion

We extended the retrieval of the Green's function to include the presence of a free surface. This function includes primaries, internal multiples, and now also free-surface multiples. Significantly, our proposed method does not require any surface-related multiple removal of the reflection response. The resulting images of the subsurface are free of any artifacts of the free surface multiples and internal multiples, this is because Marchenko imaging is a natural way to use primaries and multiples in imaging.

2.6 Acknowledgments

This work was funded by the sponsor companies of the Consortium Project on Seismic Inverse Methods for Complex Structures. We are grateful to Diane Witters for her help in preparing this manuscript. We thank Johan Robertsson, Matteo Ravasi and two anonymous reviewers for their critical feedback.

CHAPTER 3

INCORPORATING FREE-SURFACE MULTIPLES IN MARCHENKO IMAGING

Imagine placing a receiver at any location in the Earth and recording the response at that location to sources on the surface. In such a world, we could place receivers around our reservoir to better image the reservoir and understand its properties. Realistically, this is not a feasible approach for understanding the subsurface. Here, we present an alternative and realizable approach to obtaining the response of a buried virtual receiver for sources at the surface. This method is capable of retrieving the Green's function for a virtual point in the subsurface to the acquisition surface. In our case, a physical receiver is not required at the subsurface point; instead, we require the reflection measurements or sources and receivers at the surface of the Earth and a macro-model of the velocity (no small-scale details of the model are necessary). We can interpret the retrieved Green's function as the response to sources at the surface for a virtual receiver in the subsurface. We obtain this Green's function by solving the Marchenko equation, an integral equation pertinent to inverse scattering problems. Our derivation of the Marchenko equation for the Green's function retrieval takes into account the free-surface reflections present in the reflection response (in previous work we considered a response without free-surface multiples). We decompose the Marchenko equation into up- and down-going fields and solve for these fields iteratively. The retrieved Green's function not only includes primaries and internal multiples similar to previous methods, but also includes free-surface multiples. We use these up- and down-going fields to obtain a 2D image of our area of interest, in this case, below a synclinal structure. This methodology is called Marchenko imaging.

3.1 Introduction

Traditionally, to image the subsurface using standard imaging methods like reverse time migration (RTM) or Kirchhoff migration, one assumes the first-order Born approximation. This assumption only allows us to use primary reflections in conventional imaging (singly-scattered waves). However, the assumption of the first Born approximation leads to artifacts in the presence

of multiples. In order to implement conventional imaging and to ensure the assumption of single scattering holds, one has to remove multiply reflected waves. Multiples consist of internal and free-surface multiples. The removal of free-surface multiples is generally a priority in the recorded reflection response since free surface multiples are, in general, stronger than internal multiples.

To remove surface multiples from the reflection response, there are model-based methods (Lokshtanov, 1999; Wiggins, 1988), inverse-scattering based methods (Weglein et al., 1997), data-driven methods (Amundsen, 2001; Berkhout and Verschuur, 1997; Verschuur et al., 1992; Ziolkowski et al., 1999) and recently, inversion methods (van Groenestijn and Verschuur, 2009; Ypma and Verschuur, 2013). The data-driven technique proposed by Verschuur et al. (1992), surface-related multiple elimination (SRME), is a popular method for attenuating multiples because it has been proven to be effective on many real data examples. Although internal multiples are weaker, there are data driven methods (Berkhout and Verschuur, 1997; Verschuur and Berkhout, 2005) and inverse scattering methods (Ramírez et al., 2005) that remove them from the reflection response. Removing the multiples is not always a simple task; in addition, removal does not allow us to use the valuable information provided by these multiples. Multiples provide redundant as well as new information that is still useful to improve our image. Using multiples can increase the illumination and lead to better vertical resolution in the image (Jiang et al., 2007; Muijs et al., 2007a,b; Schuster et al., 2003).

A method to use the information embedded in multiples is proposed by Reiter et al. (1991), who use a ray-equation Kirchhoff depth migration to image with free-surface multiple reflections and primaries. In the final image, they achieve extended lateral coverage and an increased signal-to-noise ratio compared to imaging with primaries. However, their method requires reliable separation of free-surface multiples and primaries. In addition, ray-based algorithms, such as that given in Reiter et al. (1991), might fail in complex geologic structures.

One-way wave equation migration of multiples is proposed by Guitton et al. (2002), Muijs et al. (2007a), and Malcolm et al. (2009) to overcome the shortfalls of ray-based methods. One-way wave equation migration limits imaging of steep angle reflectors. Berkhout and Verschuur

(2006) modify the principle of SRME to transform multiples into primaries. Accordingly, these new primaries can be subjected to the same imaging criteria as normal primaries. Ong et al. (2002) incorporate RTM (two-way wave equation) into imaging multiples by using the source and receiver wavefield as the primary and multiple response, respectively. Although the subsurface image produced by the modified RTM of multiples gives better illumination and spatial resolution, there are imaging artifacts caused by high-order multiples correlating with the primaries, which place spurious reflectors incorrectly deeper (Ong et al., 2002).

In this paper, we do not investigate the advantages of imaging with multiples; we show that the artifacts caused by multiples are largely reduced compared to standard imaging techniques. We propose to use an inverse scattering approach for suppressing artifacts caused by multiples. The physical basis for exact inverse scattering is focusing and time reversal (Rose, 2002a,b), which yield the Marchenko equation. This equation is an integral equation that determines the wavefield for a (virtual) source at any point $\mathbf{x}$, given the single-sided reflection response.

Broggini et al. (2012) extend the work of Rose (2002a) to geophysics for retrieving the Green's function from reflected waves at the surface. These Green's functions include only primaries and internal multiples (Broggini et al., 2012, 2014). They use the Green's function to image the subsurface (Marchenko imaging), whereby they minimize the artifacts produced by internal multiples. Marchenko imaging uses the up- and down-going Green's function for imaging. We have incorporated the free-surface multiples in the Green's function retrieval algorithm (Singh et al., 2015); therefore our retrieved Green's functions also include free-surface multiples with the internal multiples and primaries. The major differences between our previous work (Singh et al., 2015) and this work are: (1) we show 2D imaging examples, (2) we use pressure-normalized wavefields compared to flux-normalized wavefields to obtain the Marchenko-type equations, and (3) we solve the Marchenko equations using the f_1 focusing functions (more details on normalized wavefields and focusing functions are given in the theory section). The new focusing functions, f_1, directly solve for the up- and down-going Green's functions; and these Green's functions are used in our imaging scheme.

There is another approach to imaging using inverse scattering proposed by Weglein et al. (2003), who uses a non-closed or series solution called the inverse scattering series. Unlike Weglein et al. (2003), our inverse solution to the wave equation is in the form of Fredholm integral equations of the second kind (Marchenko-type equations).

In this paper, we derive the retrieval of the Green's function by solving Marchenko-type equations using pressure-normalized wavefields. The reason for using pressure-normalized fields are given in the theory section. We show numerical examples of imaging the subsurface using the Green's functions at different depths. Note that the Green's function includes primaries, internal multiples, and free-surface multiples. We call imaging with these Green's functions Marchenko imaging. The distinction between our work and the previous papers of Wapenaar et al. (2014a), Slob et al. (2014) and Wapenaar et al. (2014b) is that we 1) include free-surface multiples in the Green's function retrieval 2) do not require the multiples to be removed from the surface reflection response 3) and subsequently minimize the artifacts caused by the free-surface multiples in the imaging. Although, the retrieval of the Green's function and hence the imaging is currently an acoustic technique; work has already begun on making the procedure elastodynamic (da Costa Filho et al., 2014; Wapenaar and Slob, 2014).

3.2 Theory

Retrieving the Green's function in the presence of a free surface, using Marchenko-type equations, is derived in multi-dimensions by Singh et al. (2015), but their numerical examples are one dimensional. The reflection response R that Singh et al. (2015) use to retrieve these functions is flux-normalized, which facilitates the derivation of the 3D Marchenko equations (Wapenaar et al., 2014a). Similarly, the retrieval of the Green's function without a free surface also uses flux-normalized wavefields, (Broggini et al., 2012; Wapenaar et al., 2013a). However, the Green's function retrieval is not restricted to flux-normalized fields and can be modified to pressure-normalized fields. Wapenaar et al. (2014a) derive the retrieval of the Green's function using pressure-normalized fields in the absence of a free surface.

In this paper, we demonstrate an alternative approach to Singh et al. (2015) by using pressure-normalized fields to retrieve the Green's function in the presence of a free surface. Like previous papers on Green's function retrieval, we obtain these Green's functions by solving Marchenko-type equations (Slob et al., 2014; Wapenaar et al., 2014a,b). We show 2D numerical examples of the retrieval and its application to imaging the subsurface. More details on flux- and pressure-normalized wavefields can be obtained from Ursin (1983), Wapenaar and Grimbergen (1996), and Wapenaar (1998).

Acoustic pressure p and vertical particle velocity v_3 are related to any type of one-way normalized fields (down-going p^+ and up-going p^-) in the space-frequency domain according to

$$\begin{pmatrix} p \\ v_3 \end{pmatrix} = \begin{pmatrix} \mathcal{L}_1 & \mathcal{L}_1 \\ \mathcal{L}_2 & -\mathcal{L}_2 \end{pmatrix} \begin{pmatrix} p^+ \\ p^- \end{pmatrix}; \tag{3.1}$$

conversely, the p^+ and p^- are related to p and v_3 by

$$\begin{pmatrix} p^+ \\ p^- \end{pmatrix} = \frac{1}{2} \begin{pmatrix} \mathcal{L}_1^{-1} & \mathcal{L}_2^{-1} \\ \mathcal{L}_1^{-1} & -\mathcal{L}_2^{-1} \end{pmatrix} \begin{pmatrix} p \\ v_3 \end{pmatrix}. \tag{3.2}$$

Here, $\mathcal{L}_1$, $\mathcal{L}_2$, and their inverses are pseudo-differential operators (Wapenaar, 1998). For pressure normalization, $\mathcal{L}_1 = \mathcal{I}$ (identity operator), while for flux-normalization, equation 3.2 becomes

$$\begin{pmatrix} p^+ \\ p^- \end{pmatrix} = \begin{pmatrix} \mathcal{L}_2^t & \mathcal{L}_1^t \\ \mathcal{L}_2^t & -\mathcal{L}_1^t \end{pmatrix} \begin{pmatrix} p \\ v_3 \end{pmatrix}, \tag{3.3}$$

where superscript t denotes operator transposition.

In a laterally invariant medium, equations 3.1 and 3.2 become, in the wavenumber-frequency domain,

$$\begin{pmatrix} \widetilde{p} \\ \widetilde{v}_3 \end{pmatrix} = \begin{pmatrix} \widetilde{\mathcal{L}}_1 & \widetilde{\mathcal{L}}_1 \\ \widetilde{\mathcal{L}}_2 & -\widetilde{\mathcal{L}}_2 \end{pmatrix} \begin{pmatrix} \widetilde{p}^+ \\ \widetilde{p}^- \end{pmatrix}, \tag{3.4}$$

and

$$\begin{pmatrix} \widetilde{p}^+ \\ \widetilde{p}^- \end{pmatrix} = \frac{1}{2} \begin{pmatrix} \widetilde{\mathcal{L}}_1^{-1} & \widetilde{\mathcal{L}}_2^{-1} \\ \widetilde{\mathcal{L}}_1^{-1} & -\widetilde{\mathcal{L}}_2^{-1} \end{pmatrix} \begin{pmatrix} \widetilde{p} \\ \widetilde{v}_3 \end{pmatrix}, \tag{3.5}$$

respecitively. Here, $\widetilde{\mathcal{L}}_1$, $\widetilde{\mathcal{L}}_2$, and their inverses are scalar functions (not operators). Equations 3.4 and 3.5 hold for any type of normalization. For pressure normalization, we have $\widetilde{\mathcal{L}}_1 = 1$ and

$\widetilde{\mathcal{L}}_2 = k_3/\omega\rho$, where $k_3 = \sqrt{\omega^2/c^2 - |\mathbf{k}|^2}$, with $\mathbf{k} = (k_1, k_2)$. For flux-normalization, we have $\widetilde{\mathcal{L}}_1 = \sqrt{\omega\rho/2k_3}$ and $\widetilde{\mathcal{L}}_2 = \sqrt{k_3/2\omega\rho}$.

We use pressure-normalized wavefields since the relationship between the two-way Green's function and the pressure-normalized one-way Green's functions is much simpler than with flux normalization. The sum of the one-way pressure-normalized fields is equal to the pressure. The flux-normalized up- and down-going Green's functions $\overline{G}^+$ and $\overline{G}^-$ are related in the space domain to the two-way Green's function by (equation 3.1)

$$G = \mathcal{L}_1(x_{3,i})\mathcal{L}_1(x_{3,0})\left(\overline{G}^+ + \overline{G}^-\right), \tag{3.6}$$

where $\mathcal{L}_1(x_{3,0})$ and $\mathcal{L}_1(x_{3,i})$ are the operators at the depth levels $x_3 = x_{3,0}$ and $x_3 = x_{3,i}$, respectively.

Therefore, in order to obtain the two-way Green's function of the pressure recording for a source of volume-injection type using flux-normalized one-way wavefields, one must apply $\mathcal{L}_1$ at $x_3 = x_{3,0}$ and $x_3 = x_{3,i}$ to the sum of $\overline{G}^+$ and $\overline{G}^-$. However, to obtain this same two-way Green's function using pressure-normalized wavefields, we simply add the up- and down-going retrieved Green's functions. Although the pressure-normalized wavefields are simpler to obtain compared to flux-normalized wavefields, their use in the derivation of the retrieval of the Green's function is more involved.

We begin the derivation of the Green's function retrieval with the frequency-domain one-way reciprocity theorems of the convolution and correlation type (Slob et al., 2014; Wapenaar et al., 2014a), which hold for lossless media between ∂D_0 (acquisition surface) and ∂D_i (arbitrary depth level):

$$\int_{\partial D_0} \rho^{-1}(\mathbf{x})[(\partial_3 p_A^+)p_B^- + (\partial_3 p_A^-)p_B^+]d\mathbf{x_0} = -\int_{\partial D_i} \rho^{-1}(\mathbf{x})[p_A^+(\partial_3 p_B^-) + p_A^-(\partial_3 p_B^+)]d\mathbf{x_i}, \tag{3.7}$$

$$\int_{\partial D_0} \rho^{-1}(\mathbf{x})[(\partial_3 p_A^+)^* p_B^+ + (\partial_3 p_A^-)^* p_B^-]d\mathbf{x_0} = -\int_{\partial D_i} \rho^{-1}(\mathbf{x})[(p_A^+)^*(\partial_3 p_B^+) + (p_A^-)^*(\partial_3 p_B^-)]d\mathbf{x_i}. \tag{3.8}$$

The asterisk * denotes complex conjugation, and the subscripts A and B denote two wave states. Equations 3.7 and 3.8 are the reciprocity theorems for pressure-normalized one-way wavefields. Equation 3.8 does not account for evanescent and horizontally propagating waves. The spatial coordinates are defined by their horizontal and depth components, for instance $\mathbf{x_0} = (\mathbf{x_{H,0}}, x_{3,0})$, where $\mathbf{x_{H,0}}$ are the horizontal coordinates at a depth $x_{3,0}$. These one-way reciprocity theorems hold for up- and down-going pressure-normalized fields.

3.2.1 One-way wavefields

The reciprocity theorems are used to solve for the Green's function. We define the Green's function as the response to an impulsive point source of volume injection rate at $\mathbf{x_0''}$ just above ∂D_0. This Green's function obeys the scalar wave equation

$$\rho\nabla.\left(\frac{1}{\rho}\nabla G\right) - \frac{1}{c^2}\frac{\partial^2 G}{\partial t^2} = -\rho\delta(\mathbf{x}-\mathbf{x_0''})\frac{\partial\delta(t)}{\partial t}. \tag{3.9}$$

We include the time derivative on the right hand side because we consider the source to be of volume injection rate. Using the Fourier convention, $p(\mathbf{x},\omega) = \int_{-\infty}^{\infty} p(\mathbf{x},t)\exp(-j\omega t)dt$, in the frequency domain, equation 3.9 becomes

$$\rho\nabla.\left(\frac{1}{\rho}\nabla G\right) + \frac{\omega^2}{c^2}G = -j\omega\rho\delta(\mathbf{x}-\mathbf{x_0''}). \tag{3.10}$$

Since we are using one-way reciprocity theorems, equations 3.7 and 3.8, we define our Green's function (two-way) as a sum of the up- and down-going pressure-normalized one-way Green's functions:

$$G(\mathbf{x},\mathbf{x_0''},\omega) = G^{+,q}(\mathbf{x},\mathbf{x_0''},\omega) + G^{-,q}(\mathbf{x},\mathbf{x_0''},\omega), \tag{3.11}$$

where $\mathbf{x}$ is the observation point. Defined this way, the one-way Green's functions are decomposed at the observation point $\mathbf{x}$ denoted by the first superscript $+$ or $-$. We consider downwards to be positive, hence the superscript $+$ represents down-going waves and $-$ up-going waves. The second superscript (q) refers to the volume-rate injection source at $\mathbf{x_0''}$. For instance, $G^{-,q}(\mathbf{x},\mathbf{x_0''},\omega)$ is the pressure-normalized up-going Green's function at $\mathbf{x}$ due to a volume injection source at $\mathbf{x_0''}$ in the frequency domain.

Similar to equation A11 in Wapenaar et al. (2014a), we define the vertical derivative of the up-going Green's function at the acquisition surface ∂D_0, just below the free surface, as

$$\partial_3 G^{-,q}(\mathbf{x}, \mathbf{x_0''}, \omega)|_{x_3=x_{3,0}} = \frac{1}{2} j\omega\rho(\mathbf{x_0}) R(\mathbf{x_0''}, \mathbf{x_0}, \omega). \tag{3.12}$$

However in our case, both $\partial_3 G^{-,q}$ and R include the free-surface multiples. Considering the downward component of the source and the surface-reflected waves, we define

$$\partial_3 G^{+,q}(\mathbf{x}, \mathbf{x_0''}, \omega)|_{x_3=x_{3,0}} = -\frac{1}{2} j\omega\rho(\mathbf{x_0})[\delta(\mathbf{x_H} - \mathbf{x_H''}) + rR(\mathbf{x_0''}, \mathbf{x_0}, \omega)], \tag{3.13}$$

where r denotes the reflection coefficient of the free surface (in the simple examples shown in this paper r is -1). For the down-going field $\partial_3 G^{+,q}$, at and below ∂D_0, we consider both the downward component of the source $-\frac{1}{2} j\omega\rho(\mathbf{x_0})\delta(\mathbf{x_H} - \mathbf{x_H''})$ and the reflections from the free surface $-\frac{1}{2} j\omega\rho(\mathbf{x_0}) rR(\mathbf{x_0''}, \mathbf{x_0}, \omega)$, similar to the Marchenko derivation with flux-normalized fields from Singh et al. (2015). At ∂D_i, the up- and down-going waves are $G^{-,q}$ and $G^{+,q}$, respectively. We define state A, shown in Figure 3.1, as the one-way pressure-normalized wavefields in the actual medium $p_A^{\pm}$ at ∂D_0 and ∂D_i, as shown in Table 3.1.

Similar to previous papers that derive Marchenko-type equations (Singh et al., 2015; Slob et al., 2014; Wapenaar et al., 2013a, 2014a), we also define focusing functions as state B (see Figure 3.2). The focusing function f_1 is a solution of the sourceless wave equation, for the waves that focus at a point at the bottom of the truncated medium. The truncated medium is called the reference medium as it is reflection free above ∂D_0 and below ∂D_i but is the same as the actual medium between ∂D_0 and ∂D_i (see Figure 3.2). The f_1 function is defined as waves that focus at $\mathbf{x_i'}$ at a defined depth level (∂D_i) for incoming f_1^+ and outgoing f_1^- waves at the acquisition surface (∂D_0) $\mathbf{x_0}$ (Figure 3.2).

The one-way wavefields for the f_1 function at the depth levels ∂D_0 and ∂D_i, which we define as State B, are shown in Figure 3.2 and Table 3.2. The one-way focusing function $f_1^+(\mathbf{x}, \mathbf{x_i'}, t)$ is shaped such that $f_1(\mathbf{x}, \mathbf{x_i'}, t)$ focuses at $\mathbf{x_i'}$ at $t = 0$. At the focusing point $\mathbf{x_i'}$ of f_1, we define $\partial_3 f_1(\mathbf{x}, \mathbf{x_i'}, t)$ as $-\frac{1}{2}\rho(\mathbf{x_i'})\delta(\mathbf{x}_H - \mathbf{x}_H')\partial\delta(t)/\partial t$, a two-dimensional (2D) and 1D Dirac delta function in space and time, respectively. After the focusing point, $f_1(\mathbf{x}, \mathbf{x_i'}, t)$ continues to diverge as a

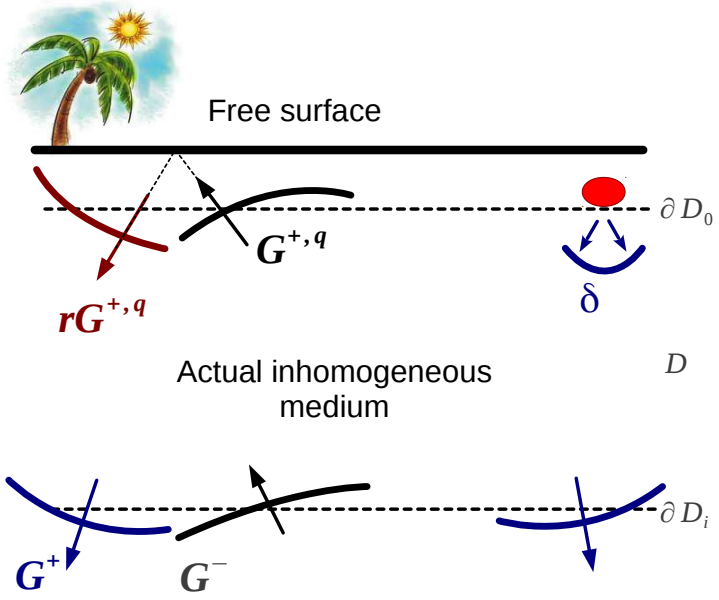

Figure 3.1: The one-way Green's functions in the actual inhomogeneous medium in the presence of a free surface at the acquisition surface ∂D_0 and the arbitrary surface ∂D_i. The tree indicates the presence of the free surface.

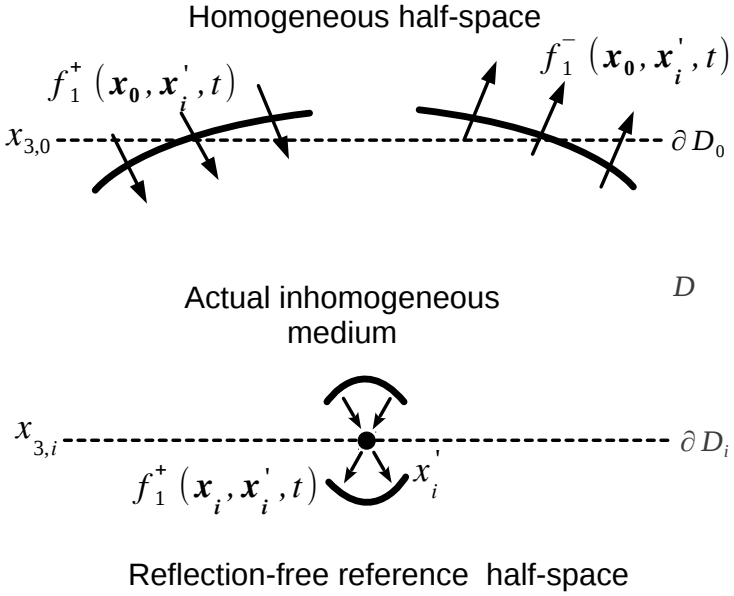

Figure 3.2: Focusing function f_1 that focuses at $\mathbf{x_i'}$ in the reference medium, where above ∂D_0 is homogeneous and below ∂D_i is reflection-free.

down-going field $f_1^+(\mathbf{x}, \mathbf{x_i'}, t)$ into the reflection-free reference half-space (Wapenaar et al., 2014a).

By substituting the one-way wavefields given in Table 3.1 (State A) and Table 3.2 (State B) into the convolution reciprocity theorem, equation 3.7, we get the up-going Green's function

$$G^{-,q}(\mathbf{x_i'}, \mathbf{x_0''}, \omega) = \int_{\partial D_0} [f_1^+(\mathbf{x_0}, \mathbf{x_i'}, \omega) R(\mathbf{x_0''}, \mathbf{x_0}, \omega) - r f_1^-(\mathbf{x_0}, \mathbf{x_i'}, \omega) R(\mathbf{x_0''}, \mathbf{x_0}, \omega)] d\mathbf{x_0} - f_1^-(\mathbf{x_0''}, \mathbf{x_i'}, \omega). \tag{3.14}$$

Likewise, substituting the one-way wavefields in Table 3.1 and Table 3.2 into the correlation reciprocity theorem, equation 3.8, we get the down-going Green's function

$$G^{+,q}(\mathbf{x_i'}, \mathbf{x_0''}, \omega) = - \int_{\partial D_0} [f_1^-(\mathbf{x_0}, \mathbf{x_i'}, \omega)^* R(\mathbf{x_0''}, \mathbf{x_0}, \omega) - r f_1^+(\mathbf{x_0}, \mathbf{x_i'}, \omega)^* R(\mathbf{x_0''}, \mathbf{x_0}, \omega)] d\mathbf{x_0} + f_1^+(\mathbf{x_0''}, \mathbf{x_i'}, \omega)^*. \tag{3.15}$$

Table 3.1: The pressure-normalized one-way wavefields in the actual inhomogeneous medium in the presence of a free surface at the depth level ∂D_0 and ∂D_i. $p_A^{\pm}$ symbolizes one-way wavefields at arbitrary depth levels in the inhomogeneous medium, while r is the reflection coefficient of the free surface.

On ∂D_0:	$\partial_3 p_A^+ =$	$\partial_3 G^{+,q}(\mathbf{x_0}, \mathbf{x_0''}, \omega) =$	$-\frac{1}{2} j\omega\rho(\mathbf{x_0}) \left(\delta(\mathbf{x_H} - \mathbf{x_H''}) + rR(\mathbf{x_0''}, \mathbf{x_0}, \omega)\right)$
	$\partial_3 p_A^- =$	$\partial_3 G^{-,q}(\mathbf{x_0}, \mathbf{x_0''}, \omega) =$	$\frac{1}{2} j\omega\rho(\mathbf{x_0}) R(\mathbf{x_0''}, \mathbf{x_0}, \omega)$
On ∂D_i:	$p_A^+ =$	$G^{+,q}(\mathbf{x_i}, \mathbf{x_0''}, \omega)$	
	$p_A^- =$	$G^{-,q}(\mathbf{x_i}, \mathbf{x_0''}, \omega)$	

Table 3.2: The one-way wavefields of the focusing function f_1 at the acquisition surface ∂D_0 and the level where f_1 focuses, ∂D_i. $p_B^{\pm}$ symbolizes one-way wavefields in the frequency domain, at arbitrary depth levels in the reference medium, see Figure 3.2.

On ∂D_0:	$p_B^+ =$	$f_1^+(\mathbf{x_0}, \mathbf{x_i'}, \omega)$	
	$p_B^- =$	$f_1^-(\mathbf{x_0}, \mathbf{x_i'}, \omega)$	
On ∂D_i:	$\partial_3 p_B^+ =$	$\partial_3 f_1^+(\mathbf{x_i}, \mathbf{x_i'}, \omega)$	$= -\frac{1}{2} j\omega\rho(\mathbf{x_i'})\delta(\mathbf{x}_H - \mathbf{x}_H')$
	$\partial_3 p_B^- =$	$\partial_3 f_1^-(\mathbf{x_i}, \mathbf{x_i'}, \omega)$	$= 0$

Equations 3.14 and 3.15 are identical to the equations for G^- and G^+ of Singh et al. (2015), however our Green's functions are pressure normalized. In addition, unlike Singh et al. (2015), there is no need to use equation 3.6 to obtain the two-way Green's function; one can simply use equation 3.11 to get G. Equations in 3.14 and 3.15 are the starting point for deriving the 3D Marchenko-type equations.

3.2.2 Marchenko Equations

Equations 3.14 and 3.15 are two equations for four unknowns ($G^{+,q}, G^{-,q}, f_1^+$, and f_1^-). After an inverse Fourier transform, we can separate these equations into two temporal parts: time earlier than the first arrival and time later than the first arrival of the Green's function at the virtual receiver location. We consider $t_d(\mathbf{x_i'}, \mathbf{x_0''})$ to be the first-arrival time of the Green's function. Hence, we can separate equations 3.14 and 3.15 for $t \geq t_d$ and $t < t_d$. These temporal constraints, along with the causality requirements give rise to two equations and two unknowns for $f^{\pm}$, after which we can retrieve $G^{\pm}$ by substitution into equations 3.14 and 3.15.

An estimate of the first arrival time $t_d(\mathbf{x_i'}, \mathbf{x_0''})$ is, for example, obtained by using finite-difference modeling of the waveforms in a smooth velocity model that acts as a macro-model. The time interval before t_d gives rise to

$$f_1^-(\mathbf{x_0''}, \mathbf{x_i'}, t) = \int_{\partial D_0} d\mathbf{x_0} \int_{-\infty}^{t} [f_1^+(\mathbf{x_0}, \mathbf{x_i'}, t') - r f_1^-(\mathbf{x_0}, \mathbf{x_i'}, t')] R(\mathbf{x_0''}, \mathbf{x_0}, t - t') dt', \tag{3.16}$$

$$f_1^+(\mathbf{x_0''}, \mathbf{x_i'}, -t) = \int_{\partial D_0} d\mathbf{x_0} \int_{-\infty}^{t} [f_1^-(\mathbf{x_0}, \mathbf{x_i'}, -t') - r f_1^+(\mathbf{x_0}, \mathbf{x_i'}, -t')] R(\mathbf{x_0''}, \mathbf{x_0}, t - t') dt', \tag{3.17}$$

because causality dictates that $G^{\pm}$ vanish for $t < t_d(\mathbf{x_i'}, \mathbf{x_0''})$.

In the reference medium where the focusing functions exist, we can define up- and down-going waves with respect to transmission responses $T(\mathbf{x_0}, \mathbf{x_i'}, t)$ at arbitrary depth levels (State C), as shown in Figure 3.3. Hence, $T(\mathbf{x_0}, \mathbf{x_i'}, t)$ is the transmission in the reference medium; which is the actual inhomogeneous medium, between ∂D_0 and ∂D_i, but homogeneous above and below ∂D_0

and ∂D_i. The up- and down-going waves in Figure 3.3 are defined in Table 3.3 according to the

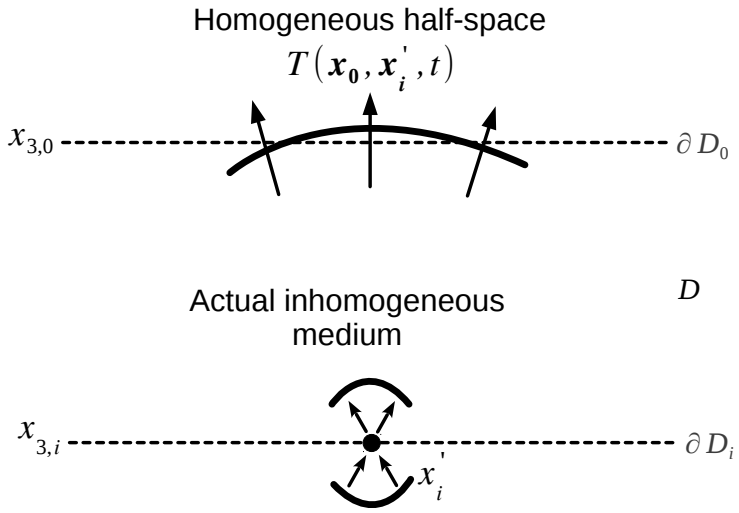

Figure 3.3: The transmission response $T(\mathbf{x_0}, \mathbf{x_i'}, t)$ in the reference configuration.

reciprocity relations:

Table 3.3: The one-way wavefields in the reference medium at the acquisition surface ∂D_0 and the level where f_1 focuses, ∂D_i. $p_C^{\pm}$ symbolizes one-way wavefields in the frequency domain, at arbitrary depth levels in the reference medium, see Figure 3.3. The source location is just below ∂D_i.

On ∂D_0:	$\partial_3 p_C^+ =$	$0,$
	$\partial_3 p_C^- =$	$\partial_3 T(\mathbf{x_0}, \mathbf{x_i'}, \omega),$
On ∂D_i:	$p_C^+ =$	$0,$
	$p_C^- =$	$\delta(\mathbf{x}_H - \mathbf{x}_H').$

Substituting the one-way wavefields represented in Table 3.2 and Table 3.3 into the one-way convolution reciprocity theorem, equation 3.7, yields

$$\delta(\mathbf{x_H''} - \mathbf{x_H'}) = \int_{\partial D_0} \frac{\partial_3 T(\mathbf{x_0}, \mathbf{x_i'}, \omega)}{-\frac{1}{2} j\omega\rho(\mathbf{x_0})} f_1^+(\mathbf{x_0}, \mathbf{x_i''}, \omega) d\mathbf{x_0}, \tag{3.18}$$

where we represent the source positions of the focusing function f_1^+ with double primes instead of single. For simplicity, we define $\mathcal{T}(\mathbf{x_0}, \mathbf{x_i'}, \omega) = \dfrac{\partial_3 T(\mathbf{x_0}, \mathbf{x_i'}, \omega)}{-\dfrac{1}{2} j\omega\rho(\mathbf{x_0})}$; hence in the time domain (from equation 3.18), f_1^+ is the inverse of the transmission response:

$$f_1^+(\mathbf{x_0}, \mathbf{x_i}^{'}, t) = \mathcal{T}^{inv}(\mathbf{x_0}, \mathbf{x_i'}, t). \tag{3.19}$$

Analogous to Wapenaar et al. (2014b), Slob et al. (2014), and Singh et al. (2015), we adopt the assumption for the pressure-normalized version of f_1^+ to be

$$f_1^+(\mathbf{x_0}, \mathbf{x_i}^{'}, t) = \mathcal{T}_d^{inv}(\mathbf{x_0}, \mathbf{x_i'}, t) + M(\mathbf{x_0}, \mathbf{x_i'}, t), \tag{3.20}$$

where $\mathcal{T}_d^{inv}$ is the inverse of the direct arrival of the transmission response, and M is the coda following $\mathcal{T}_d^{inv}$. We can approximate $\mathcal{T}_d^{inv}$ as the time-reversed direct arrival of the pressure-normalized Green's function (hence the need for a smooth velocity model as previously mentioned).

Substituting assumption 3.20 into the time-domain representation of equations 3.16 and 3.17 yields the following Marchenko equations for $t < t_d(\mathbf{x_i'}, \mathbf{x_0''})$:

$$\begin{aligned} f_1^-(\mathbf{x_0''}, \mathbf{x_i'}, t) = & \int_{\partial D_0} d\mathbf{x_0} \int_{-\infty}^{-t_d^\epsilon(\mathbf{x_i'}, \mathbf{x_0})} \mathcal{T}_d^{inv}(\mathbf{x_0}, \mathbf{x_i'}, t') R(\mathbf{x_0''}, \mathbf{x_0}, t - t') dt' \quad + \\ & \int_{\partial D_0} d\mathbf{x_0} \int_{-t_d^\epsilon(\mathbf{x_i'}, \mathbf{x_0})}^{t} M(\mathbf{x_0}, \mathbf{x_i'}, t') R(\mathbf{x_0''}, \mathbf{x_0}, t - t') dt' \quad - \\ & r \int_{\partial D_0} d\mathbf{x_0} \int_{-t_d^\epsilon(\mathbf{x_i'}, \mathbf{x_0})}^{t} f_1^-(\mathbf{x_0}, \mathbf{x_i'}, t') R(\mathbf{x_0''}, \mathbf{x_0}, t - t')] dt', \end{aligned} \tag{3.21}$$

$$\begin{aligned} M(\mathbf{x_0''}, \mathbf{x_i'}, -t) = & \int_{\partial D_0} d\mathbf{x_0} \int_{-t_d^\epsilon(\mathbf{x_i'}, \mathbf{x_0})}^{t} f_1^-(\mathbf{x_0}, \mathbf{x_i'}, -t') R(\mathbf{x_0''}, \mathbf{x_0}, t - t') dt' \quad - \\ & r \int_{\partial D_0} d\mathbf{x_0} \int_{-t_d^\epsilon(\mathbf{x_i'}, \mathbf{x_0})}^{\infty} M(\mathbf{x_0}, \mathbf{x_i'}, t') R(\mathbf{x_0''}, \mathbf{x_0}, t + t')] dt' \quad - \\ & r \int_{\partial D_0} d\mathbf{x_0} \int_{-t}^{-t_d^\epsilon(\mathbf{x_i'}, \mathbf{x_0})} \mathcal{T}_d^{inv}(\mathbf{x_0}, \mathbf{x_i'}, t') R(\mathbf{x_0''}, \mathbf{x_0}, t + t')] dt', \end{aligned} \tag{3.22}$$

with $t_d^{\epsilon}(\mathbf{x_i'}, \mathbf{x_0})$= $t_d(\mathbf{x_i'}, \mathbf{x_0}) - \epsilon$, where ϵ is a small positive constant to include the direct arrival in the integrals. We choose to solve the Marchenko equations (3.21 and 3.22) iteratively as follows:

$$\begin{aligned} f_{1,k}^{-}(\mathbf{x_0''}, \mathbf{x_i'}, t) = &\int_{\partial D_0} d\mathbf{x_0} \int_{-\infty}^{-t_d^{\epsilon}(\mathbf{x_i'}, \mathbf{x_0})} \mathcal{T}_d^{inv}(\mathbf{x_0}, \mathbf{x_i'}, t') R(\mathbf{x_0''}, \mathbf{x_0}, t - t') dt' \quad + \\ &\int_{\partial D_0} d\mathbf{x_0} \int_{-t_d^{\epsilon}(\mathbf{x_i'}, \mathbf{x_0})}^{t} M_{k-1}(\mathbf{x_0}, \mathbf{x_i'}, t') R(\mathbf{x_0''}, \mathbf{x_0}, t - t') dt' \quad - \\ &r \int_{\partial D_0} d\mathbf{x_0} \int_{-t_d^{\epsilon}(\mathbf{x_i'}, \mathbf{x_0})}^{t} f_{1,k-1}^{-}(\mathbf{x_0}, \mathbf{x_i'}, t') R(\mathbf{x_0''}, \mathbf{x_0}, t - t')] dt', \end{aligned} \tag{3.23}$$

$$\begin{aligned} M_k(\mathbf{x_0''}, \mathbf{x_i'}, -t) = &\int_{\partial D_0} d\mathbf{x_0} \int_{-t_d^{\epsilon}(\mathbf{x_i'}, \mathbf{x_0})}^{t} f_{1,k}^{-}(\mathbf{x_0}, \mathbf{x_i'}, -t') R(\mathbf{x_0''}, \mathbf{x_0}, t - t') dt' \quad - \\ &r \int_{\partial D_0} d\mathbf{x_0} \int_{-t_d^{\epsilon}(\mathbf{x_i'}, \mathbf{x_0})}^{\infty} M_{k-1}(\mathbf{x_0}, \mathbf{x_i'}, t') R(\mathbf{x_0''}, \mathbf{x_0}, t + t')] dt' \quad - \\ &r \int_{\partial D_0} d\mathbf{x_0} \int_{-t}^{-t_d^{\epsilon}(\mathbf{x_i'}, \mathbf{x_0})} \mathcal{T}_d^{inv}(\mathbf{x_0}, \mathbf{x_i'}, t') R(\mathbf{x_0''}, \mathbf{x_0}, t + t')] dt'. \end{aligned} \tag{3.24}$$

Note that we are not limited to solving the Marchenko equations iteratively; one can use a preferred integral solver such as conjugate gradients or least-squares inversion. The corresponding focusing function f_1^+ for each iteration reads (from equation 3.19)

$$f_{1,k}^{+}(\mathbf{x_0}, \mathbf{x_i'}, t) = \mathcal{T}_d^{inv}(\mathbf{x_0}, \mathbf{x_i'}, t) + M_{k-1}(\mathbf{x_0}, \mathbf{x_i'}, t). \tag{3.25}$$

3.2.3 Marchenko iterative scheme

We initialize the Marchenko iterative scheme by obtaining the direct arrival of the Green's function. The time-reversed version of this direct arrival can be used as an approximation for $\mathcal{T}_d^{inv}$ which takes into account travel times and geometric spreading but ignores transmission losses at the interfaces (Wapenaar et al., 1989, 2014a).

With this initialization, the iterative scheme for $k = 0$ is as follows:

$$f_{1,0}^{-}(\mathbf{x_0''}, \mathbf{x_i'}, -t) = \int_{\partial D_0} d\mathbf{x_0} \int_{-\infty}^{-t_d^{\epsilon}(\mathbf{x_i'}, \mathbf{x_0})} \mathcal{T}_d^{inv}(\mathbf{x_0}, \mathbf{x_i'}, t') R(\mathbf{x_0''}, \mathbf{x_0}, t - t^{'}) dt^{'}, \tag{3.26}$$

$$M_0(\mathbf{x_0''},\mathbf{x_i'},-t) = \int_{\partial D_0} d\mathbf{x_0} \int_{-t_d^{\epsilon}(\mathbf{x_i'},\mathbf{x_0})}^{t} f_{1,0}^{-}(\mathbf{x_0},\mathbf{x_i'},-t')R(\mathbf{x_0''},\mathbf{x_0},t-t')dt' \quad - \\ r\int_{\partial D_0} d\mathbf{x_0} \int_{-t}^{-t_d^{\epsilon}(\mathbf{x_i'},\mathbf{x_0})} \mathcal{T}_d^{inv}(\mathbf{x_0},\mathbf{x_i'},t')R(\mathbf{x_0''},\mathbf{x_0},t+t')]dt'. \tag{3.27}$$

Now the iterative scheme described in equations 3.23-3.25 can be initiated with equations 3.26 and 3.27 to solve for f_1^+ and f_1^-. These focusing functions can then be substituted in equations 3.11, 3.14 and 3.15 to obtain the retrieved two-way pressure-normalized Green's function, and the up- and down-going one-way pressure-normalized Green's function, respectively.

3.2.4 Marchenko imaging

Behura et al. (2012); Broggini et al. (2012, 2014); Singh et al. (2015); Slob et al. (2014); Wapenaar et al. (2011, 2014b) have all used the retrieved one-way Green's functions to produce an image. Marchenko imaging is built on the concept of obtaining the reflection response from the up- and down-going wavefields at an arbitrary depth level. The use of up- and down-going wavefield for imaging is not a new principle. Claerbout (1971), Wapenaar et al. (2000) and Amundsen (2001) have shown that one can get the reflection response below an arbitrary depth level once the up- and down-going wavefields are available.

The governing equation for imaging with such one-way wavefields is (Wapenaar et al., 2008a)

$$G^{-,q}(\mathbf{x_i'},\mathbf{x_0''},t) = \int_{\partial D_i} d\mathbf{x_i} \int_{-\infty}^{\infty} G^{+,q}(\mathbf{x_i},\mathbf{x_0''},t-t')R_0(\mathbf{x_i'},\mathbf{x_i},t')dt', \tag{3.28}$$

where ∂D_i is an arbitrary depth level and R_0 is the reflection response of the medium below ∂D_i. Note that equation 3.28 holds for outgoing and incoming wavefields normal to the surface ∂D_i. However, the retrieved Green's functions (current methods) are strictly up- and down-going wavefields at arbitrary depth levels, which corresponds to a flat surface ∂D_i. The reflection response R_0, in equation 3.28, is the response as if everything above ∂D_i is transparent. Therefore, R_0 is a virtual reflection response as if there were receivers and sources at ∂D_i, in the absence of a free-surface at ∂D_i. Significantly, the response R_0 is blind to the actual overburden above ∂D_i.

Wapenaar et al. (2014b) have shown the retrieval of this virtual reflection below a complex overburden. In this paper, any variable with a subscript 0 (e.g., R_0) indicates that no free-surface is present.

We choose to solve for R_0 in equation 3.28 by multidimensional deconvolution (MDD) (van der Neut et al., 2011). Details of solving equation 3.28 using retrieved Green's functions are given in Wapenaar et al. (2014b). The significant difference between our work and the previous Marchenko imaging papers is that our Green's functions include information of the actual medium with the free-surface and include all (free-surface and internal) multiples. This corresponds to minimizing the artifacts caused by free-surface multiples and internal multiples in the imaging. Once we obtain R_0 at each image point, our subsurface image is the contribution of R_0 at zero offset and zero time, i.e., $R_0(\mathbf{x_i}, \mathbf{x_i}, 0)$.

3.3 Numerical examples

Our numerical model has variable velocity and density, as shown in Figure 3.4 and Figure 3.5 respectively. We use a 2D inhomogeneous subsurface model with a syncline structure. The horizontal range of the model is -3000 m to 3000 m. Our goal is to show: (1) the retrieval of the Green's function $G(\mathbf{x}_\mathbf{i}', \mathbf{x}_\mathbf{0}'', t)$ for a virtual receiver at $\mathbf{x_i} = (0, 1100)$ m and the corresponding variable source locations at $\mathbf{x}_\mathbf{0}''$; (2) the subsurface image below the syncline structure. To obtain the Green's function, we need the pressure-normalized reflection response $R(\mathbf{x}_\mathbf{0}'', \mathbf{x_0}, \omega)$ and a macro-model (no small-scale details of the model are necessary). The reflection response is computed by finite differences (Thorbecke and Draganov, 2011) with vertical-force sources and particle-velocity receiver recordings, both at the surface. The receiver spacing is 10 m and the source is a Ricker wavelet with a central frequency of 20 Hz. We use this finite-difference response and equation 3.2 to get the pressure-normalized reflection response $R(\mathbf{x}_\mathbf{0}'', \mathbf{x_0}, \omega)$ which we deconvolve with the source wavelet. See Figure 3.6 for an example of a single shot at $\mathbf{x}_\mathbf{0}'' = (0, 0)$ m with the direct arrivals from source to receivers removed. The macro-model is a smooth version of the velocity model which we use to compute the travel times of the direct arrival (see Figure 3.7). No density

information is required.

We use the macro-model to obtain the first-arrival from the virtual source at $\mathbf{x_i} = (0, 1100)$ m to the surface (by an eikonal solver). This first arrival is time-reversed to initialize the iterative scheme with $\mathcal{T}_d^{inv}$ as well as to guide us in choosing the time windows for equations 3.14-3.17. Figure 3.8 shows $\mathcal{T}_d^{inv}$, which is equivalent to $f_{1,0}^{+}$.

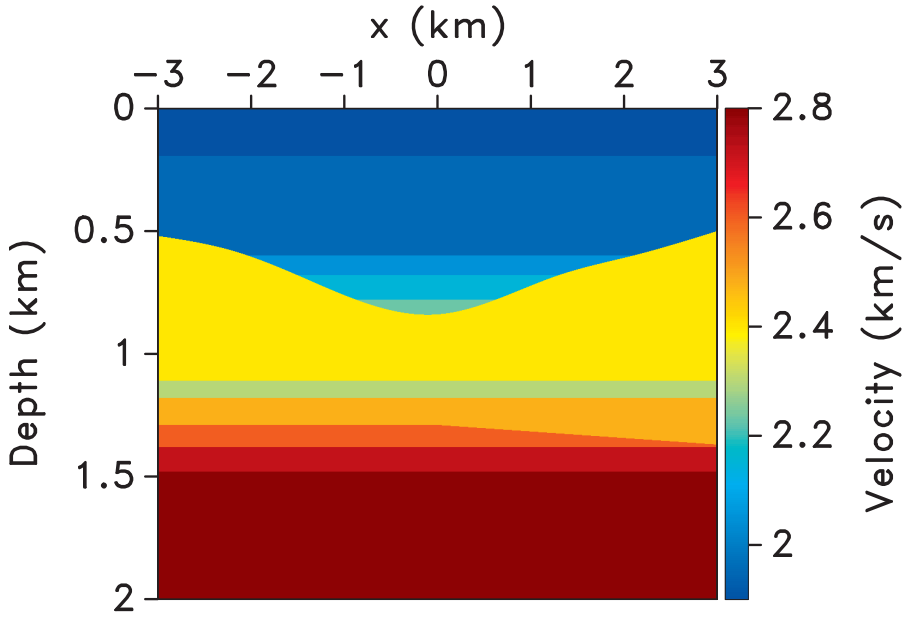

Figure 3.4: The velocity model ranging from velocities 1.9 to 2.8 km/s as shown in the color bar.

3.3.1 Focusing functions

We build the focusing functions $f_{1,k}^{+}$ and $f_{1,k}^{-}$ using the iterative scheme in equations 3.23-3.25. Figure 3.9 shows the functions $f_{1,k}^{+}$ and $f_{1,k}^{-}$ for iteration index $k = 0, 1, 5$. Note that these one-way focusing functions reside in the time-window $-t_d < t < t_d$.

The integrals that we use to solve for the focusing function, equations 3.16 and 3.17, have spatial limits between $-\infty$ and ∞, which means we require infinite aperture. In our implementation, we truncate the spatial integral. This truncation requires tapering at the edges of the reflection response, which corresponds to the reduced amplitudes of the focusing functions at the far offsets.

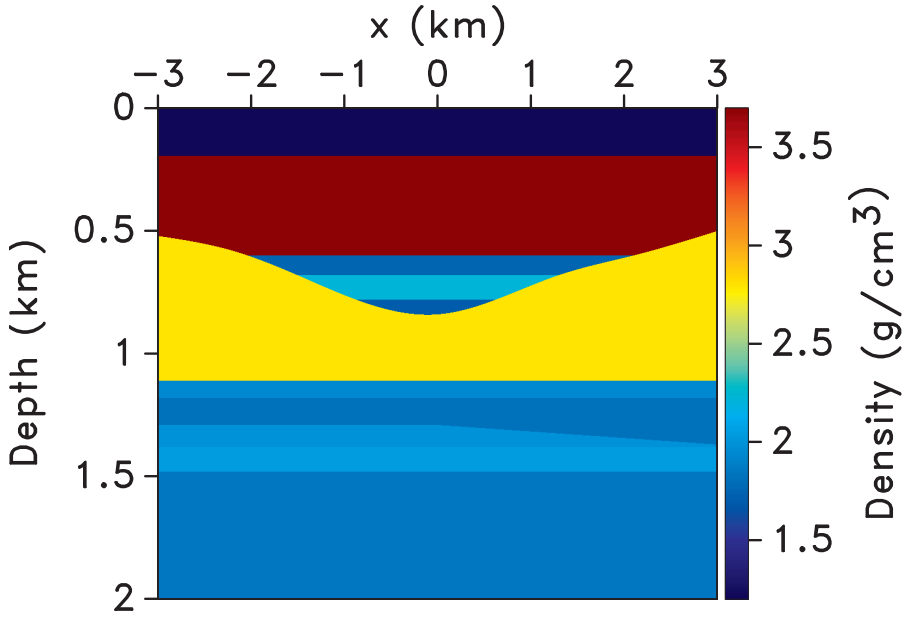

Figure 3.5: The density model ranging from densities 1 to 3.5 g/cm^3 as shown in the color bar.

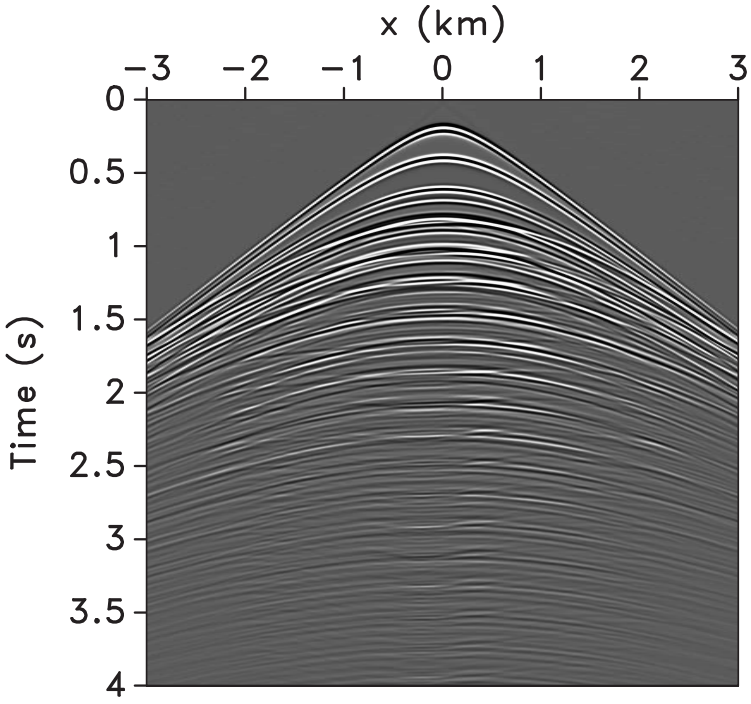

Figure 3.6: The reflection response corresponding to the inhomogeneous velocity and density model in Figure 3.4 and Figure 3.5.

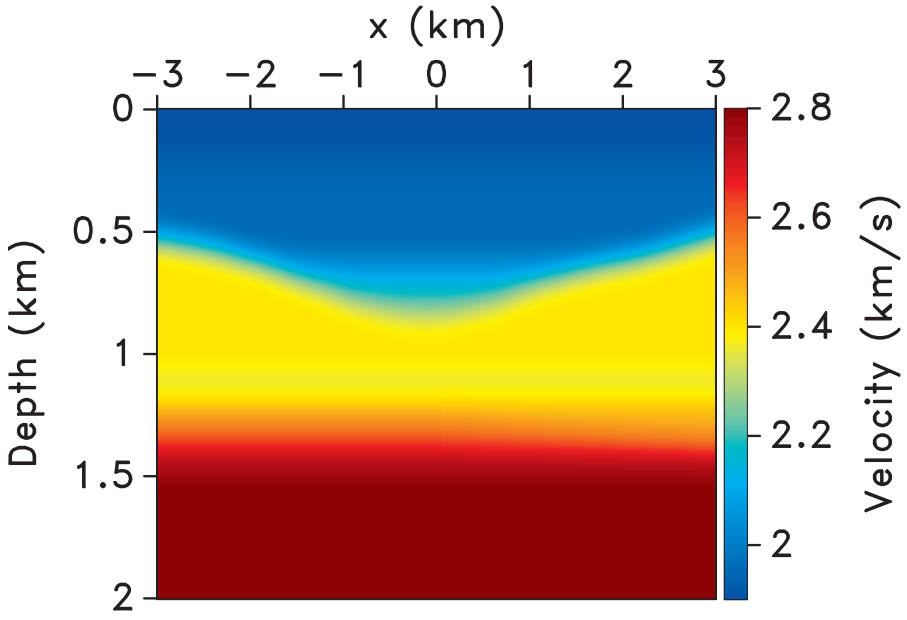

Figure 3.7: Macro-model, i.e. smooth version of Figure 3.4, used to compute the first arrivals from the virtual source location to the surface.

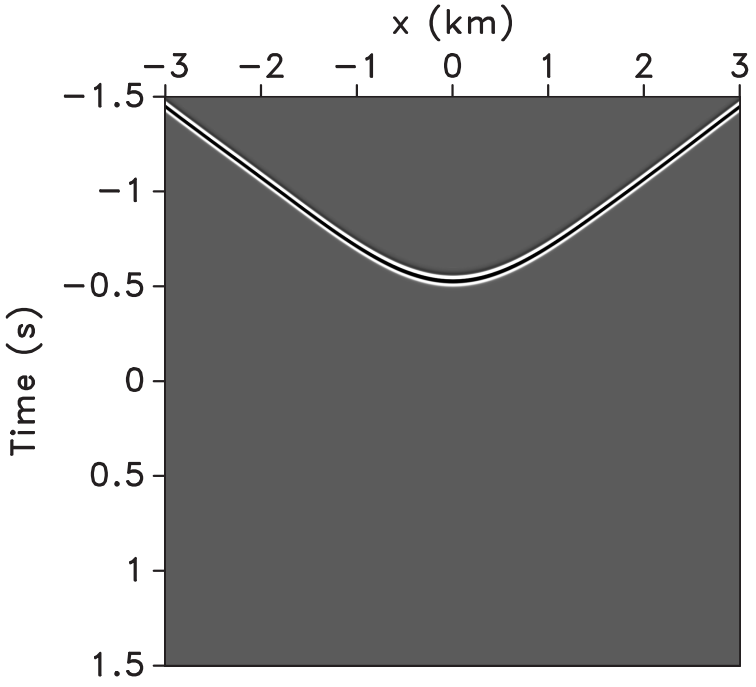

Figure 3.8: The time-reversed first arrival for a virtual source at $\mathbf{x_i} = (0, 1100)$ m and receivers at the surface. This event is used to initialize the Marchenko iterative scheme ($\mathcal{T}_d^{inv}$).

From iteration index $k = 0$ to $k = 1$, new events are generated in the focusing function. Even the focusing function $f^-_{1,k}$ at $k = 0$ already has the main features that are obtained after five iterations. In iteration $k = 1$ to $k = 5$, the focusing functions look kinematically similar. Higher-order iterations generally correct the amplitude errors in the focusing functions.

3.3.2 Green's function retrieval

By substituting the focusing functions in equations 3.14 and 3.15, we obtain the one-way pressure-normalized Green's functions, as shown in Figure 3.10. These up- and down-going Green's functions are the response for a receiver at $\mathbf{x}'_\mathbf{i} = (0, 1100)$ m and variable source locations $\mathbf{x}''_\mathbf{0}$. To see the internal multiples and the free-surface multiples in Figure 3.10, we display the Green's functions with a time-dependent gain of $\exp(1.5 * t)$.

The two-way Green's function is given as the summation of the up- and down-going Green's functions. A comparison of this retrieved two-way Green's function with the modeled Green's function (modeled with the exact small-scale variations in the velocity and density) is shown in Figure 3.11. For display, we apply a gain of $\exp(1.5 * t)$ to the Green's functions in Figure 3.11 to better see the internal multiples and free-surface multiples at larger travel-times. The retrieved and modeled Green's functions match almost perfectly, as shown in Figure 3.11. As expected, the far-offsets do not provide a good match because we are truncating the spatial integrals in the Marchenko equations.

3.3.3 Comparison of Green's functions with and without the free surface

Previous formulations of Green's function retrieval, mentioned in the introduction of this paper, require the reflection response without free-surface multiples. This means that an additional processing step to remove the surface reflections is required before implementing the Green's function retrieval algorithm for past formulations. For such an implementation, the Green's function does not include free-surface multiples; hence the imaging procedure does not take these multiples into account. Figure 3.12 shows the up- and down-going one-way Green's function without free surface multiples. The Green's functions in Figure 3.12 are retrieved using the Marchenko

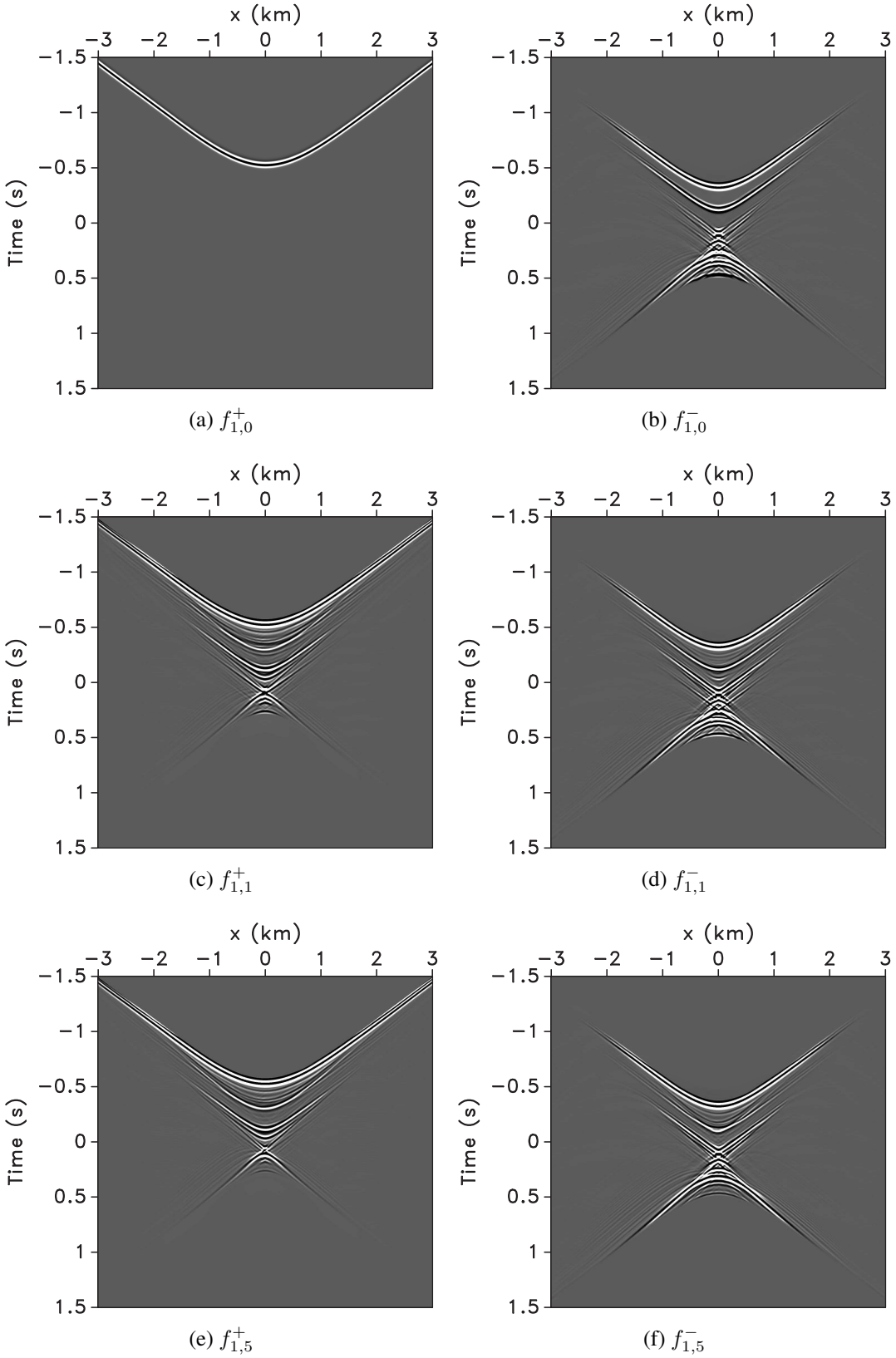

(a) $f^+_{1,0}$ (b) $f^-_{1,0}$

(c) $f^+_{1,1}$ (d) $f^-_{1,1}$

(e) $f^+_{1,5}$ (f) $f^-_{1,5}$

Figure 3.9: One-way focusing functions $f^+_{1,k}$ and $f^-_{1,k}$ that focus at $\mathbf{x}'_\mathbf{i}$ for iteration index $k = 0, 1, 5$.

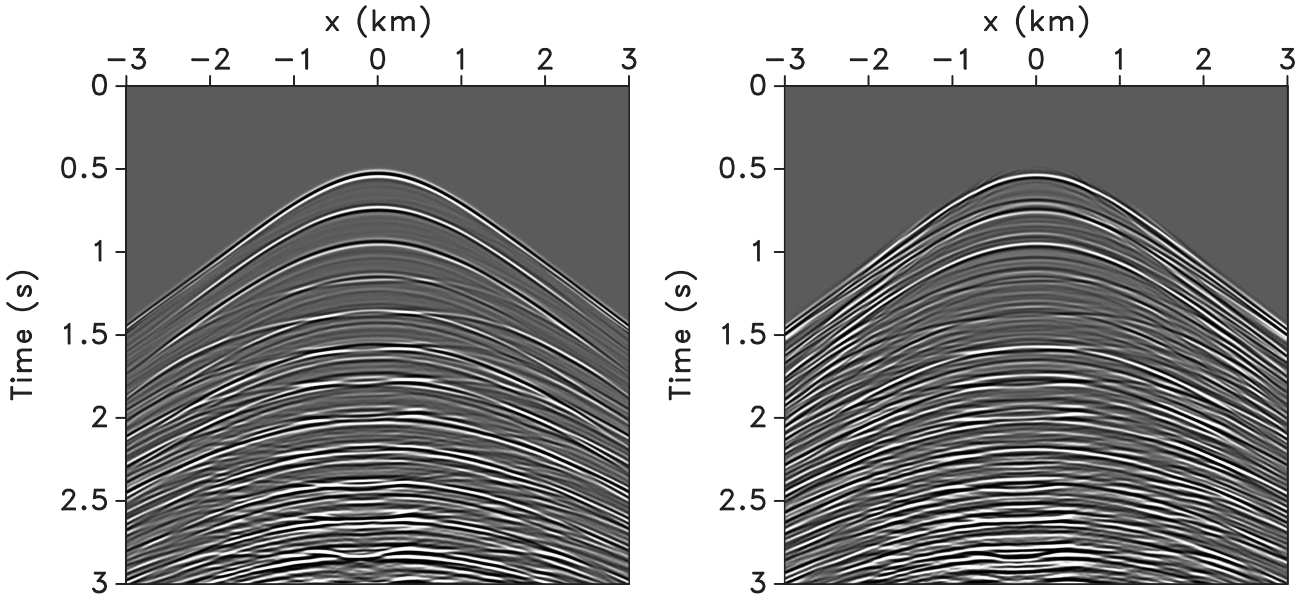

(a) G^{+} (b) G^{-}

Figure 3.10: One-way pressure-normalized Green's functions G^{+} (down-going) and G^{-} (up-going) for a virtual receiver position $\mathbf{x}_{\mathbf{i}}' = (0, 1100)$ m and a range of source positions $\mathbf{x}_{\mathbf{0}}''$. These Green's functions include free-surface multiples.

method that does not take into account free-surface multiples (Broggini et al., 2014; Wapenaar et al., 2014a); we remove the free-surface multiples from the reflection response before retrieving these Green's functions.

The Green's functions in Figure 3.12 are the response for a virtual receiver position $\mathbf{x}_{\mathbf{i}}' = (0, 1100)$ m and variable source positions $\mathbf{x}_{\mathbf{0}}''$. For display, we also apply a time-dependent gain of $\exp(1.5 * t)$ to the Green's functions. As expected, the Green's functions with the free-surface G^{+} and G^{-} have greater waveform complexity and higher amplitudes than the Green's functions in the absence of the free surface G_0^{+} and G_0^{-}. This is obvious for times larger than 1.5 seconds for both Figure 3.10 and Figure 3.12.

The events in the one-way Green's functions $G^{\pm}$ may be stronger than in $G_0^{\pm}$. For time larger than 1 second, the free-surface multiples (in red) dominate in Figure 3.13. In addition, we avoid SRME on the reflection response by using the Marchenko equations for Green's function retrieval that includes free-surface multiples (our work). It remains to be investigated to what extent these

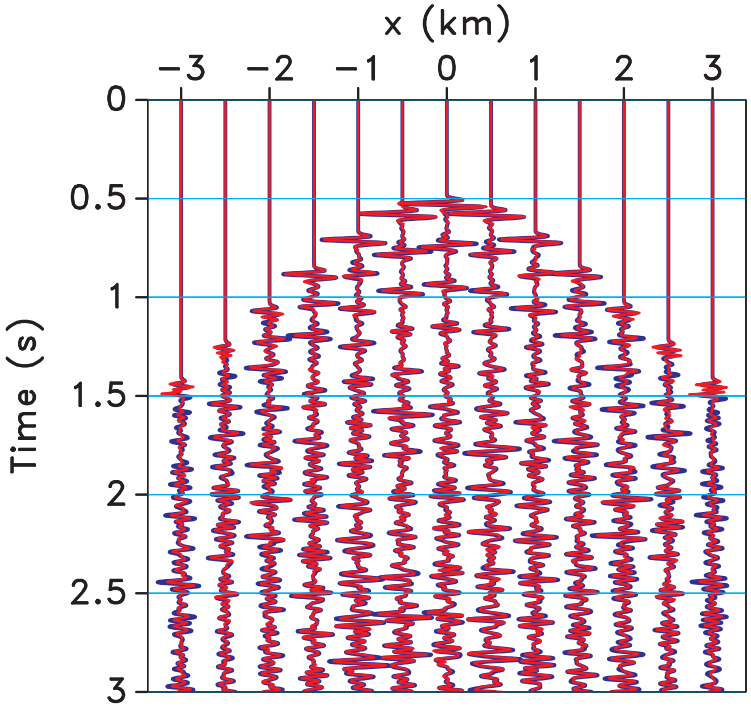

Figure 3.11: The retrieved two-way Green's function (in red) superimposed on the modeled Green's function (in blue, computed by finite differences with the small-scale details in the velocity and density model included) for a virtual receiver position $\mathbf{x}_i' = (0, 1100)$ m and a range of source positions $\mathbf{x}_0''$.

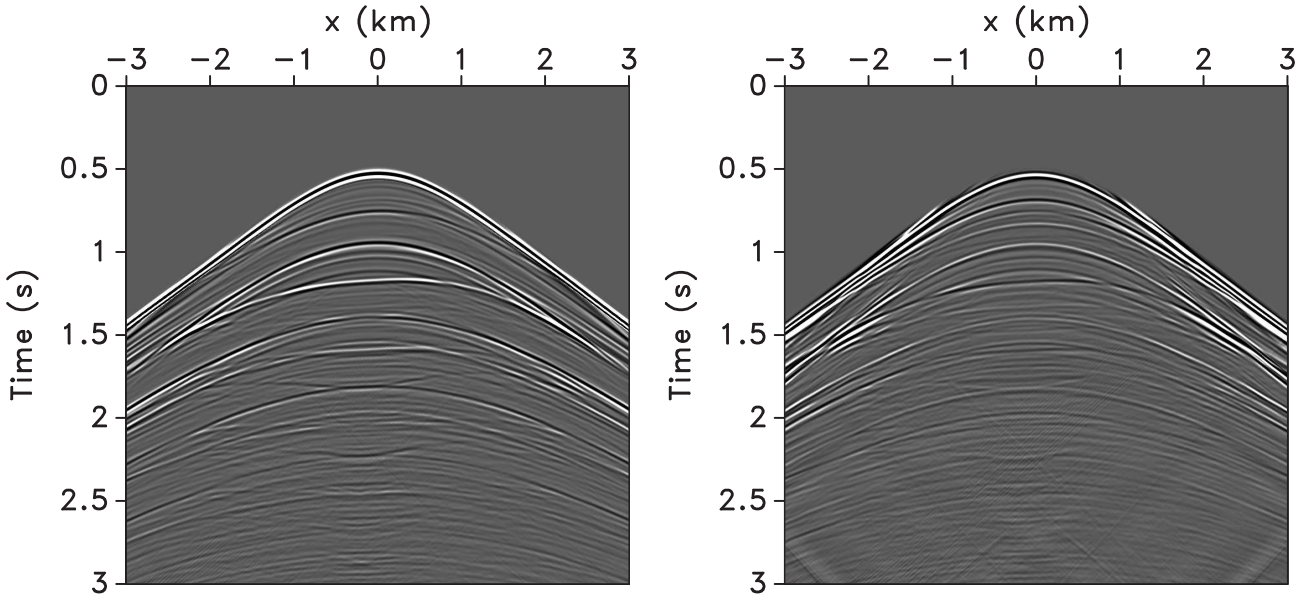

(a) G_0^+ (b) G_0^-

Figure 3.12: One-way pressure-normalized Green's functions G_0^+ (down-going) and G_0^- (up-going) for a virtual receiver position $\mathbf{x_i'} = (0, 1100)$ m and a range of source positions $\mathbf{x_0''}$. These Green's functions do not include free-surface multiples.

retrieved multiples will improve the image quality.

3.3.4 Marchenko imaging – Target oriented

Target-oriented Marchenko imaging entails retrieving the up- and down-going Green's functions in the target area and using them to construct the target image in Figure 3.14. Figure 3.15 shows the Marchenko imaging of the model in Figure 3.14. To compute this image, we retrieve the up- and down-going Green's functions $G^{\pm,q}(\mathbf{x_i'}, \mathbf{x_0''}, t)$ at the virtual receiver locations $\mathbf{x_i'} = (\mathbf{x_H'}, x_{3,i})$ ranging from $\mathbf{x'_{H,i}} = -2$ to 2 km and $x_{3,i} = 1$ to 2 km. We sample $\mathbf{x'_{H,i}}$ and $x_{3,i}$ every 40 m and 10 m, respectively, to retrieve the Green's function. These functions are used to invert for $R_0(\mathbf{x_i}, \mathbf{x_i'}, t)$ as explained in the theory section. The contribution to the image is $R_0(\mathbf{x_i}, \mathbf{x_i}, 0)$, which is R_0 at zero-offset and zero time for the range of $\mathbf{x_i}$.

The target-oriented Marchenko image, Figure 3.15, has its artifacts caused by the internal multiples and free-surface multiples in the overburden largely suppressed. If the free-surface multiples

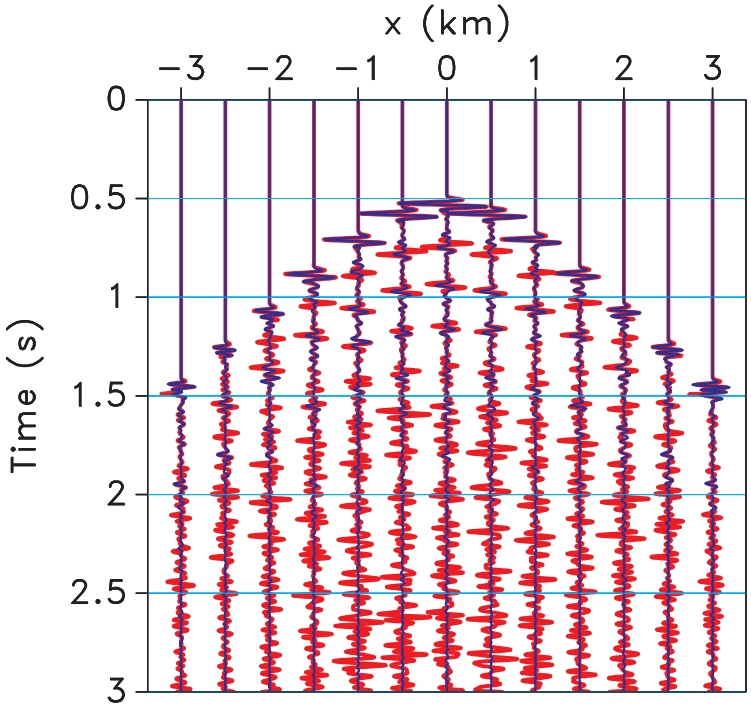

Figure 3.13: Green's function G_0 without the free surface (blue) and the Green's function G with the free surface (red) for a virtual receiver at $\mathbf{x}_\mathbf{i}' = (0, 1100)$ m and a range of source positions $\mathbf{x}_\mathbf{0}''$.

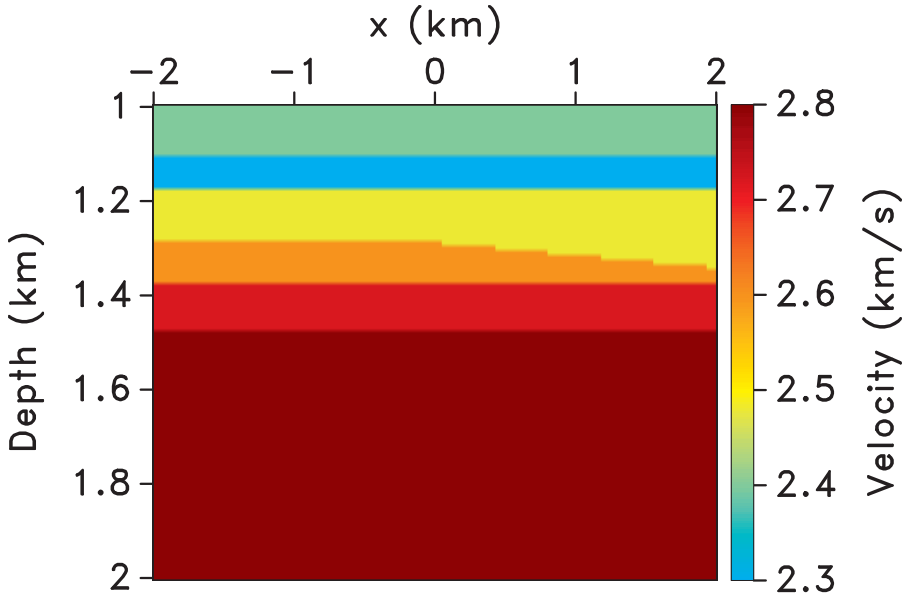

Figure 3.14: Region of the velocity model targeted for imaging. Note we do not use this model to implement Marchenko imaging, we use a smooth version of the velocity model (Figure 3.7) only. This model ranges from -2 to 2 km in the x_1-coordinate and 1 to 2 km in the x_2-coordinate.

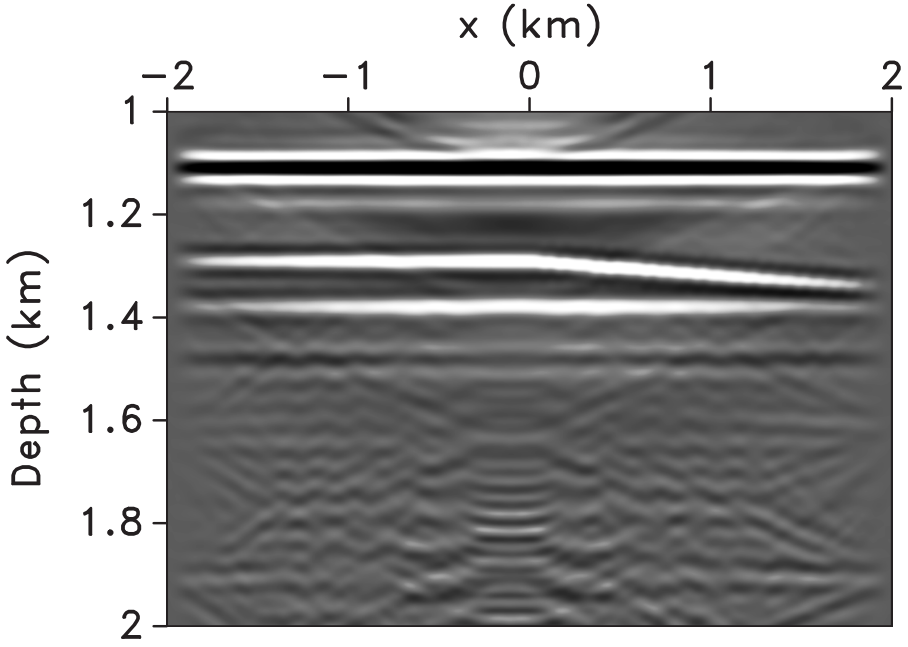

Figure 3.15: Target-oriented Marchenko imaging of the model in Figure 3.14 below the syncline structure. The image is $R_0(\mathbf{x_i}, \mathbf{x_i}, 0)$ for $\mathbf{x_i}$ ranging from $\mathbf{x_H} = -2$ to 2 km and $x_{3,i} = 1$ to 2 km.

were not handled correctly by Marchenko imaging then the associated multiples caused by the syncline and the layers within the syncline would be present in our image. However, Marchenko imaging removes the artifacts related to the multiples caused by these interfaces. To understand the adverse effects the multiples have on the subsurface image, we show a reverse time migration image, which we know does not place multiples at the correct depth level, Figure 3.16. The reverse time migration image shown in Figure 3.16 is zoomed in to the target location after the entire image was constructed. Figure 3.16 includes many artifacts introduced by the multiples such that the actual reflectors in the model are masked by these artifacts.

We also remove the free-surface from the reflection response and again conduct reverse time migration, Figure 3.17. Note that the reverse time migration image still has artifacts because the reflection response has internal multiples which are not correctly handled by reverse time migration. These artifacts can be seen by comparing the target model in Figure 3.14 with the reverse time migration examples. The artifacts are either non-existent or quite minimal in the target-oriented Marchenko-imaging, Figure 3.15.

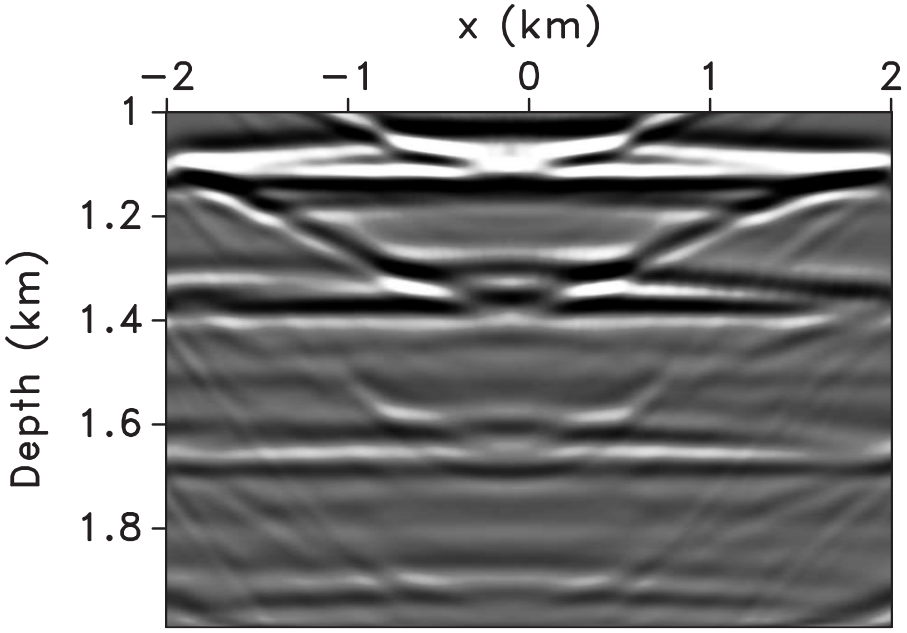

Figure 3.16: Zoomed in image of the reverse time migration for the model in Figure 3.14 below the syncline structure. The surface-reflection response used for imaging includes primaries, internal multiples and free-surface multiples.

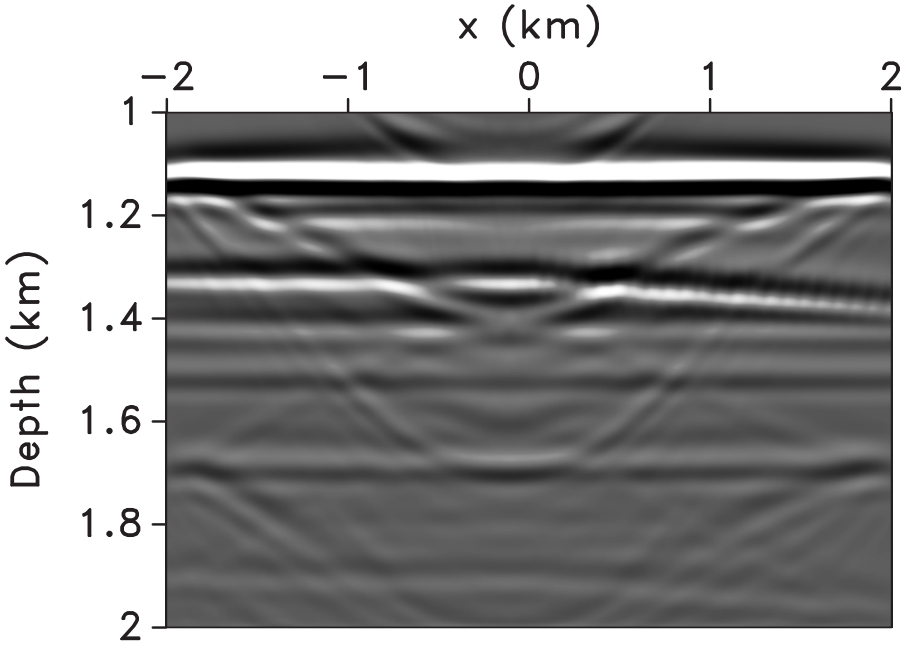

Figure 3.17: Zoomed in image of the reverse time migration for the model in Figure 3.14 below the syncline structure. The surface-reflection response used for imaging includes primaries and internal multiples, the free-surface multiples are removed.

3.4 Conclusion

We have shown that we can retrieve the Green's function at any location in the subsurface without any knowledge of the small-scale variations of the subsurface once we have sufficient aperture coverage on the surface over the virtual source location. These Green's functions include not only primaries and internal multiples but also free-surface multiples. To retrieve the Green's function, we require the reflection response at the surface and a macro-model of the subsurface overburden velocity (at least between the surface and the virtual source depth level). In comparison to previous work on the Green's function retrieval by the Marchenko equation, our reflection response at the surface includes free-surface multiples and therefore, obviates the need to remove free-surface multiples in the reflection response.

The reflection response is required to be well sampled at the surface. The more densely sampled our reflection response, the more accurately we can solve the Marchenko equations. The accuracy of our Green's function retrieval is also dependent on the kinematic accuracy of the macro-model. Another limitation of the Green's function retrieval scheme is that we assume all waves can be decomposed into up- and down-going events; hence, horizontally propagating waves are not included in our current method.

Once we know the Green's function at the surface and the virtual receiver locations, we should be able to infer what is inside the medium (volume). We can form the image in two ways: (1) downward continuation to a given reference level at the top of the target zone, and then conventional imaging in the target; (2) target-oriented imaging at all depth levels in the target. In this paper we follow the second approach. We construct a target-oriented image by deconvolution of the up- and down-going Green's function, evaluated at zero offset and zero time.

In the numerical examples, we observe no significant artifacts in the Marchenko image, due to misplaced multiples, even though the reflection response includes multiples (no preprocessing is done to remove the multiples). How the multiples improve the image is yet to be investigated; however, Marchenko imaging largely suppresses the artifacts caused by internal and free-surface multiples.

Significantly, the inputs for Marchenko imaging and for the current state-of-the-art imaging techniques are the same: the reflection response and a macro-model. However, in Marchenko imaging, we accurately handle not only the primaries but also the multiples.

3.5 Acknowledgments

This work was funded by the sponsor companies of the Consortium Project on Seismic Inverse Methods for Complex Structures. We are grateful to Diane Witters for her help in preparing this manuscript. The numeric examples in this paper are generated with the Madagascar open-source software package freely available from http://www.ahay.org. We would also like to thank Ivan Vasconcelos (Schlumberger Gould Research), Esteban Diaz (CWP) and Vladimir Li (CWP) for fruitful discussions.

CHAPTER 4

STRATEGIES FOR IMAGING WITH MARCHENKO-RETRIEVED GREEN'S FUNCTIONS

Recent papers show that imaging with the retrieved Green's function constructed by the Marchenko equations, called Marchenko imaging, reduces the artifacts from internal and free-surface multiples compared to standard imaging techniques. Even though the artifacts are reduced, they can still be present in the image, depending on the imaging condition used. We show that when imaging with the up- and down-going Green's functions, the Multidimensional Deconvolution (MDD) imaging condition yields better images compared to correlation and deconvolution. *Better* in this case means improved resolution, fewer artifacts and a closer match with the true reflection coefficient of the model. The MDD imaging condition only uses the primaries to construct the image, while the multiples are implicitly subtracted in th imaging step. Consequently, combining the first arrival of the down-going Green's function with the complete up-going Green's function produces superior (or at least equivalent) images than using the one-way Green's functions since the first arrival of the down-going Green's function excludes all the down-going multiply reflected waves. We also show that standard imaging algorithms which use the redatumed reflection response, constructed with the one-way Green's functions, produce images with reduced artifacts from multiples compared to standard imaging conditions which use surface reflection data. All imaging methods that rely on the Marchenko equations require the same inputs as standard imaging techniques: the reflection response at the surface and a smooth version of the velocity.

4.1 Introduction

The Marchenko equations can be used to retrieve the up- and down-going Green's function between an arbitrary virtual receiver in the subsurface and a source on the surface. However these equations do not prescribe how to use the Green's function in imaging. The purpose of this paper is to explain and compare different strategies for imaging with these up- and down-going Green's functions. Imaging with these Green's functions is called Marchenko imaging. Standard

imaging techniques assume single scattering, and therefore misposition multiple-reflection events in the image. However, imaging with the Marchenko-retrieved Green's functions significantly reduces (if not eliminates) the artifacts associated with multiple reflections (Singh et al. (2015); Slob et al. (2014); Wapenaar et al. (2014b) and Singh et al. (2016)). There are many types of imaging conditions that can be used to image the subsurface with the Marchenko Green's functions; they are, however, mostly restricted to imaging with Green's functions that include only primaries and internal multiples and they have never been systematically compared for imaging artifacts.

Broggini et al. (2011) show that one can retrieve at the surface the up- and down-going Green's function in 1D at a point (virtual source) in the subsurface. These Green's functions include primaries and internal multiples. Wapenaar et al. (2012) extended the Green's function retrieval to 3D by solving the Marchenko equations in multidimensions. Imaging using the Marchenko-retrieved Green's functions was first proposed in 1D by Wapenaar et al. (2011), using deconvolution of the associated up- and down-going Green's functions at zero lag. Behura et al. (2012) applied the Marchenko Green's functions to image 2D models, at specific target locations in the model, using a correlation imaging condition. This correlation imaging condition is the correlation of the up- and down-going Green's function at each image point in the subsurface at zero lag and zero-offset.

Broggini et al. (2014) show that the image constructed by multidimensional deconvolution (MDD) (van der Neut et al., 2011; Wapenaar et al., 2008b) of the up- and down-going Green's function, compared to the correlation image (Behura et al., 2012), produced a similar image of the subsurface; however the MDD image better matched the true reflectivity of the model. Imaging with MDD has significantly reduced imaging artifacts compared to standard imaging techniques like reverse time migration (RTM) and downward continuation (Broggini et al., 2014; Slob et al., 2014; Wapenaar et al., 2014b). These imaging artifacts are due to the presence of internal multiples in the data that are not properly handled.

Singh et al. (2015, 2016) modified the Marchenko equations to not only include primaries and internal multiples, but also free-surface multiples. These modified Marchenko equations obviate the need to remove the free-surface multiples from the reflection response before computing the

Green's functions. The free surface is the strongest reflector in the Earth, and free-surface multiples are generally stronger than internal multiples. Free-surface multiples can even be as strong as primaries (Weglein and Dragoset, 2007). For models with free-surface multiples, Singh et al. (2016) show that the MDD image with Marchenko Green's functions has reduced imaging artifacts due to the multiples compared to reverse time migration.

In this paper, we investigate different imaging conditions for the Green's functions that include primaries, internal multiples, and free-surface multiples (see Table Table 4.1). In addition to correlation and deconvolution imaging algorithms using the up- and down-going Green's function $G^{\pm}$, we also image the subsurface with the first arrival of the down-going Green's function G_f^+ and the up-going Green's function G^-. Bakulin and Calvert (2006) and Mehta et al. (2007) show that muting the wavefield recording at the virtual source location, so that it is limited to its first arrival, improves the virtual source method. This muting suppresses spurious events in the virtual source gather. We use the same concept of muting the first arrival of G^+ to further reduce the imaging artifacts from multiples in the Marchenko image.

For simplicity, we separate our investigation on Marchenko imaging strategies into 1D and 2D. In our 1D investigation we consider both analytical and numerical examples that investigate the strengths and weaknesses of each imaging condition given in Table Table 4.1. We also compare each imaging condition using either the up- and down-going Green's functions or the up- and first arrival of the down-going Green's functions. The conclusions of our 1D analysis is applicable to the 2D scenario. In our 2D investigation we compare imaging with a standard imaging technique, reverse time migration, and Marchenko imaging.

4.2 1D strategies for imaging

In this section we restrict our imaging and theory to 1D. The ideas, conclusions, and analysis are, however applicable, for the most part, to multidimensions . The imaging conditions analyzed in this section are 1) correlation 2) deconvolution. We also compare the application of these imaging conditions to either the up-going Green's function G^- and down-going Green's function G^+

Table 4.1: Summary of the imaging conditions we use in this paper. All imaging conditions, be it correlation, deconvolution or multidimensional deconvolution, are taken at zero-time and zero offset to construct the image. G^+, G^-, and G_f^+ are the down-going, up-going and first arrival of the down-going Green's function at the image point, respectively. The ticks (✓) means that the condition at the top of the column holds while **X** means that the condition is not satisfied.

	True reflectivity image		**Correct position of interfaces = No False interfaces**		**Correct Redatum reflection response**	
Imaging	G^+ *with* G^-	G_f^+ *with* G^-	G^+ *with* G^-	G_f^+ *with* G^-	G^+ *with* G^-	G_f^+ *with* G^-
Correlation	✘	✘	✘	✔	✘	✘
Deconvolution for 1D image	✔	✔	✔	✔	✔	✘
Deconvolution for 2D image	✘	✘	✘	✔	✘	✘
Multidimensional deconvolution	✔	✔	✔	✔	✔	✘

or to the up-going Green's function G^- and first arrival of the down-going Green's function G_f^+. In addition, we investigate the retrieval of the redatumed reflection response using correlation and deconvolution. A summary of our findings are shown in Table Table 4.1. For completeness and simplicity, we analyze each imaging condition in 1D; in two parts: an analytical investigation and a numerical investigation. Our analytical model is shown in Figure 4.1 while our numerical model is shown in Figure 4.2.

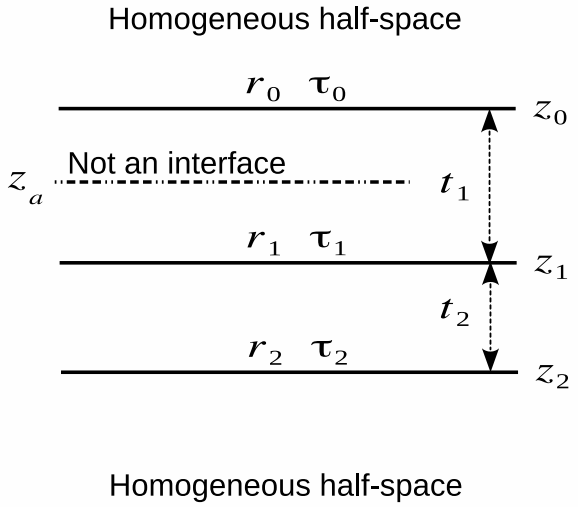

Figure 4.1: Analytical 1D model for retrieval of the Green's functions and imaging. The model is used to compute the reflection response for sources and receivers just as the first layer z_0.

Note that our analytical model and numerical model are different. The numerical model has a free surface at the acquisition surface in contrast to the transparent surface of our analytical model. Omitting the free surface in the analytical model in Figure 4.1 greatly simplifies the mathematics and interpretation. The details of the Green's function retrieval for our analytical model is given in the Appendix B.

For our 1D models, we denote the depth as z_i, where the subscript $i = 0, 1, 2, ...$ corresponds to the depth in 1D; for instance z_0 is the acquisition surface. Superscript $(+)$ refers to down-going

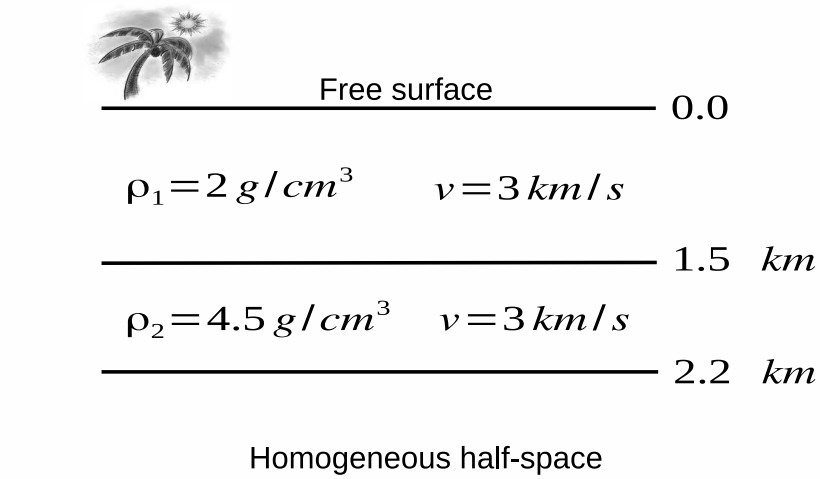

Figure 4.2: Numerical 1D model with a free surface and constant velocity of 3 km/s. The Green's functions are retrieved at each position in space to create snapshots of the wavefields propagating thorough this model. We use this model in our 1D strategies for imaging section to describe our numerical investigation in 1D.

waves and $(-)$ to up-going waves at the depth z. Any variable with a subscript 0 that is not the coordinate field z, (e.g., R_0) indicates that no free surface is present. We start with an overview of the analytical and numerical investigation before evaluating each imaging condition in 1D.

Analytical investigation

We use a three-interface (two layer) model with the first interface just below the acquisition surface. The analytical expression for the reflection response for such a model (see Figure 4.1) is given by Goupillaud (1961), equation B.1. The analytical model does not include a free surface; however, the ideas for this simple model can be extended to models with a free surface. In the Appendix B, we discuss, in detail, the retrieval of the Green's function for the analytical model in Figure 4.1.

We retrieve the Green's function at a virtual receiver in the subsurface using equations B.4 and B.5 (Broggini and Snieder, 2012; Broggini et al., 2012; Singh et al., 2015, 2016; Slob et al., 2014; Wapenaar et al., 2013a, 2014b). In our **analytical investigation**, we retrieve the Green's functions at two virtual receiver locations: 1) in the middle of the first layer ($z = z_a$) and 2) just above the second interface ($z = z_1$), in Figure 4.1. The expressions for the up- and down-going Green's functions $G^{\pm}$ at $z = z_a$ and $z = z_1$ is shown in the Appendix B, equations B.9, B.8, B.15, and B.14. The choice for the location of the virtual receivers at z_a and z_1 will become apparent later in this section. Note that at z_a there is no interface while at z_1 there is an interface with reflection coefficient r_1, as shown in Figure 4.1.

Numerical investigation

Unlike the analytical investigation, we use the model in Figure 4.2, which has variable density and constant velocity, to numerically image the subsurface using the Marchenko retrieved Green's functions. Although we are using a constant velocity model for our numerical investigation, the Marchenko equations and the corresponding imaging is not limited to a constant velocity. Our analytical work is restricted to imaging at only two locations in Figure 4.1 while our numerical investigation computes the image at 5 m intervals in the numerical model in Figure 4.2. Each image point corresponds to a virtual receiver location of the Green's function. We compute the up-

and down-going Green's functions at each virtual receiver location in the subsurface for sources on the surface.

We build our intuition of imaging with these Green's functions by analyzing snapshots of these Green's functions (see Figure 4.3) at all virtual receiver locations. For example in Figure 4.3(a) and Figure 4.3(b), when G^+ reaches the first interface at 1.5 km, it generates an up-going wave in the Green's function G^-. In Figure 4.3(b), G^+ and G^- are kinematically equivalent at the interface and we exploit this kinematic equivalence to determine the position and reflection coefficient of the interface.

Additionally, a multiple (labeled A) is generated at the free surface in Figure 4.3(e). This multiple can also become kinematically equivalent with other reflections in G^- (labeled B) in Figure 4.3(f), which can cause imaging artifacts (false interfaces) depending on the imaging condition. However, this free-surface multiple in G^+ (labeled A in Figure 4.3(e) and Figure 4.3(f)) also interacts with the interfaces and creates an associated up-going wave in G^-.

This intuition of kinematic similarity between waves at interfaces is related to the work of Claerbout (1985), who has shown that the up- and down-going wavefields at an arbitrary datum can be used for imaging. Hence, we can use the up- and down-going retrieved Green's function at the virtual receiver location to image the subsurface. The governing equation for imaging with up- and down-going wavefields in 1D is

$$G^-(z_i, z_0, t) = \int_{-\infty}^{\infty} G^+(z_i, z_0, t - t') R_0(z_i, z_i, t') dt', \tag{4.1}$$

where z_i is an arbitrary depth level and R_0 is the reflection response of the medium below z_i (Amundsen, 2001; Claerbout, 1985; Wapenaar et al., 2008b). In this expression $R_0(z_i, z_i, t)$ is the reflection response for sources and receivers at z_i, with the medium above z_i being homogeneous.

The image of the subsurface is $R_0(z_i, z_i, t = 0)$, the reflection response R_0 at zero time. Intuitively, for a source and a receiver coincident at an interface z_i, the zero time response $R_0(z_i, z_i, t = 0)$ at that location is the contribution to the image corresponding to the interface. Similarly, in the absence of an interface at z_i, the contribution of $R_0(z_i, z_i, t = 0)$ at zero time is zero.

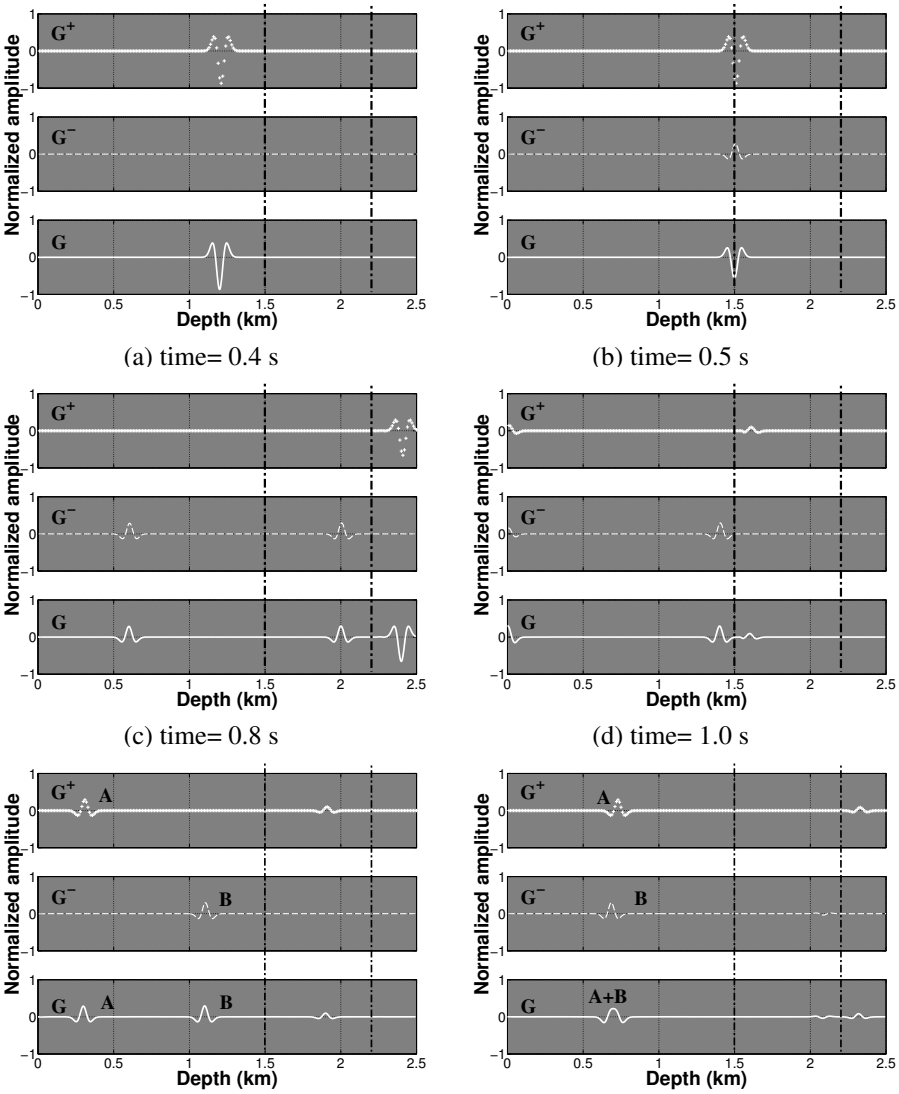

(a) time= 0.4 s

(b) time= 0.5 s

(c) time= 0.8 s

(d) time= 1.0 s

(e) time= 1.1 s

(f) time= 1.24 s

Figure 4.3: Snapshots of the Green's functions: down-going $G^{+}(z, z_0, t)$ (top), up-going $G^{-}(z, z_0, t)$ (middle), and total $G(z, z_0, t)$ (bottom), with virtual receivers ranging from $z = (0 - 2.5)\ km$. We start at 0.4 seconds for the model given in Figure 4.2. The vertical black lines at 1.5 km and 2.2 km are the interfaces.

We now investigate the Marchenko imaging conditions as summarized in Table Table 4.1: 1) correlation 2) deconvolution. The last column of Table Table 4.1, obtaining the correct redatumed reflection response, is investigated as a separate subsection 4.2.3 in this 1D imaging strategies segment.

4.2.1 Imaging Condition- Correlation

The contribution at the zero-lag correlation of two 1D signals is due to kinematically similar events in the signals. For this reason standard imaging techniques, for example Reverse Time Migration (RTM), generally use the correlation at zero lag as the contribution to the image (Baysal et al., 1983; McMechan, 1989; Whitmore, 1983). As discussed in the previous section, kinematically similar events in the up- and down-going Green's function are generally the location of the interfaces. However, unlike the Marchenko wavefields, the fields used in conventional RTM assumes the Born approximation and therefore RTM has artifacts in the presence of multiples (Glogovsky et al., 2002; O'Brien and Gray, 1996).

In the time domain, the zero-lag correlation-imaging condition in 1D for the retrieved up- and down-going Green's function is

$$C(z_i, z_0, t = 0) = \int_{-\infty}^{\infty} G^{-}(z_i, z_0, t')G^{+}(z_i, z_0, t')dt'. \tag{4.2}$$

Equation 4.2 means that the correlation image is the time integral of the up- and down-going Green's function.

Analytical investigation

In this subsection of correlation imaging, we investigate mathematically the correlation imaging condition, equation 4.2, applied to the 1D model in Figure 4.1. To illustrate the properties of the correlation image at the center of the first layer $z = z_a$ and the top of the second interface $z = z_1$ for our analytical example in Figure 4.1, we first perform a series expansion of the respective up- and down-going Green's function given in the Appendix B, equations B.9, B.8, B.15, and B.14. We first analyze the image at the center of the first layer $z = z_a$, where there is no interface.

The series expansion of the down-going Green's functions G^+ equation B.8 at the center of the first layer is

$$G^-(z_a, z_0, \omega) = \tau_0(r_1 e^{-\frac{3}{2}i\omega t_1} + r_2 e^{-i\omega(\frac{3}{2}t_1+2t_2)} + ...), \tag{4.3}$$

where r_1, r_2, t_1 and t_2 are the reflection coefficients and one-way travel times of the first and second layers, respectively; τ_0 is the transmission coefficient of the first interface (see Figure 4.1) and ... are the higher order terms in the reflection coefficients of the series. The series expansion of 4.3 follows from the geometric series rule $1/1 - r = \sum_{k=0}^{\infty} r^k$. The inverse Fourier transform of equation 4.3 is

$$G^-(z_a, z_0, t) = \tau_0\{r_1\delta(t-\frac{3}{2}t_1) + r_2\delta(t-\frac{3}{2}t_1 - 2t_2) + ...\}, \tag{4.4}$$

Additional terms in the series are given in the Appendix B (equation B.11) and we verify these terms in Figure B.1.

For the up-going Green's function G^+, the series expansion yields

$$G^+(z_a, z_0, \omega) = \tau_0\{e^{-\frac{1}{2}i\omega t_1} + r_1 r_2 e^{-i\omega(\frac{5}{2}t_1+2t_2)} - r_0 r_1 e^{-\frac{5}{2}i\omega t_1} + ...\}. \tag{4.5}$$

In the time domain, equation 4.5 becomes

$$G^+(z_a, z_0, \omega) = \tau_0\{\delta(t - \frac{1}{2}t_1) + r_1 r_2\delta(t - \frac{5}{2}t_1 - 2t_2) - r_0 r_1\delta(t - \frac{5}{2}t_1) + ...\}. \tag{4.6}$$

For a model where $t_2 = t_1/2$, the second and third terms of the series in equations 4.4 and 4.6, respectively, coincide in time, as shown in Figure 4.4. Hence, from equation 4.2, there is a contribution to the correlation image at $z = z_a$, although there is no interface at this depth. This contribution to the correlation image at $z = z_a$ is an artifact (false interface) (see Table Table 4.1) from an internal multiple in the first layer and a reflection from the second layer, as shown in Figure 4.4.

At $z = z_1$, the location of the interface, the series expansion of the up- and down-going Green's functions $G^{\pm}$ in equation B.15 and B.14 yields (in the time domain)

$$G^-(z_1, z_0, t) = \tau_0\{r_1\delta(t - t_1) + r_2\delta(t - t_1 - 2t_2) + ...\},$$

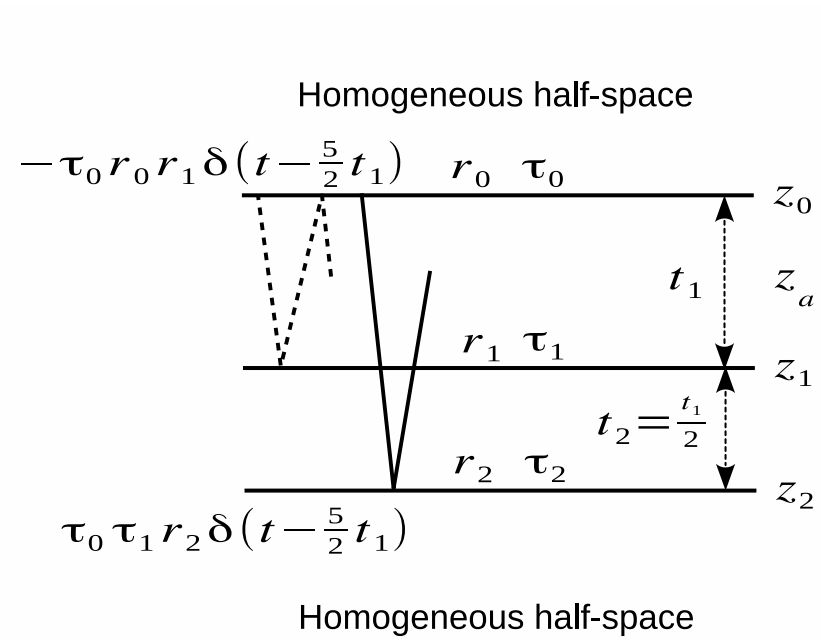

Figure 4.4: Schematic of a event in the up- and down-going Green's function at z_a for the one-way travel time $t_2 = t_1/2$. The reflected wave shown by the solid line represents the second term in equation 4.3, while the dotted line is the third term in equation 4.5. These events occur at the same time at z_a in their corresponding Green's function, hence they contribute to the correlation image.

$$G^{+}(z_1, z_0, t) = \tau_0\{\delta(t - t_1) + r_1 r_2 \delta(t - t_1 - 2t_2) + ...\}. \tag{4.7}$$

In equation 4.7, the events in the up- and down-going Green's functions occur at the same time; hence they contribute to the image. The higher order terms in the series expansion of equations B.14 and B.15 also have similar times in both the up- and down-going Green's functions and also contribute to the image at z_1. Therefore, at the interface, all events in the up- and down-going Green's functions are kinematically equivalent. These events (kinematically the same) are summed together (integral over time dt' in equation 4.2) to produce the correlation image. The contribution to the correlation image at z_1 for the terms in equation 4.7 is $\tau_0^2(r_1 + r_1 r_2^2 + ...)$. The reflection coefficient r_1 does not match the correlation image at the interface z_1 but this should come as no surprise since we are not solving equation 4.1 exactly for R_0 (as shown in Table Table 4.1: **x** at true reflectivity image for correlation imaging).

Numerical investigation

We apply the correlation imaging condition at each virtual receiver location for the associated G^{+} and G^{-}; the corresponding image is shown in Figure 4.5.

For the actual model in Figure 4.2, the reflection coefficient of the first layer at 1.5 km is 0.33 while the second interface at 2.2 km is 0.38. Comparing the parameters for the actual model to the correlation image in Figure 4.5 shows that: 1) the reflection coefficients of the actual model do not match the correlation image, however the two interfaces are correctly positioned at 1.5 km and 2.2 km, respectively; 2) we obtain an spurious event at 0.7 km in the correlation image that does not match the interfaces in the actual model (refer to Table Table 4.1 in the correlation imaging row) 3) the relative amplitudes of the interfaces in the correlation image are also incorrect.

The presence of the false interface is explained in Figure 4.3(f), where a free surface multiple in G^{+} (labeled A) interacts with the up-going reflection (labeled B) from the second layer in G^{-} at approximately 0.7 km. At this depth of 0.7 km, G^{+} and G^{-} have kinematically similar events (waves A and B) and hence an incorrect contribution to the correlation image. This false event at 0.7 km are due to free-surface multiples in G^{+} correlating at zero lag with, not only, the second

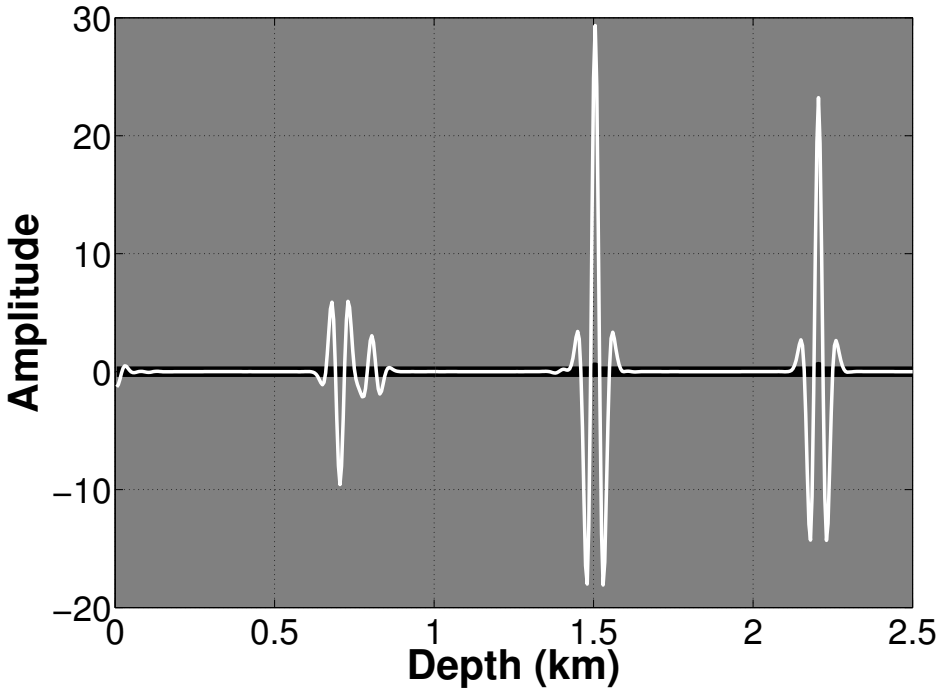

Figure 4.5: Correlation-imaging condition constructed from the up- and down-going retrieved Green's functions between virtual sources in the subsurface to the surface. We construct these Green's functions at virtual source positions every 5 m in the subsurface.

layer primary event but other multiples at later times.

4.2.2 Imaging Condition- Deconvolution

In the frequency domain, the reflection response R_0 (equation 4.1) in 1D is a deconvolution

$$R_0(z_i, z_i, \omega) = \frac{G^-(z_i, z_0, \omega)}{G^+(z_i, z_0, \omega)} \Rightarrow \frac{G^-(z, \omega) G^+(z, \omega)^*}{|G^+(z, \omega)|^2 + \epsilon}, \tag{4.8}$$

where * represents the complex conjugate and ϵ is a regularization parameter to avoid division by zero (Clayton and Wiggins, 1976). The deconvolution imaging condition similar to the correlation imaging condition is R_0 at zero time at the location of the Green's function virtual receiver z_i.

Analytical investigation

Since we obtain the up- and down-going Green's function at a point in the subsurface analytically (no noise), solving equation 4.8 is simply a division of these functions in the frequency domain. We first analyze R_0 at the center of the first layer z_a for the model given in Figure 4.1. The division of the up-going with the down-going Green's function at z_a, given in equations B.8 and B.9, respectively, yields

$$\begin{aligned} R_0(z_a, z_a, \omega) &= \frac{G^-(z_a, z_0, \omega)}{G^+(z_a, z_0, \omega)}, \\ &= \frac{r_1 e^{-\frac{3}{2} i\omega t_1} + r_2 e^{-i\omega(\frac{3}{2} t_1 + 2t_2)}}{e^{-\frac{1}{2} i\omega t_1} + r_1 r_2 e^{-i\omega(\frac{1}{2} t_1 + 2t_2)}}, \\ &= \frac{r_1 e^{-i\omega t_1} + r_2 e^{-i\omega(t_1 + 2t_2)}}{1 + r_1 r_2 e^{-2i\omega t_2}}, \\ &= \{r_1 e^{-i\omega t_1} + r_2 e^{-i\omega(t_1+2t_2)}\}\{1 + \sum_{n=1}^{\infty} (-r_1 r_2 e^{-2i\omega t_2})^n\} \end{aligned} \tag{4.9}$$

Note that the denominators in G^+ and G^- in equations B.8 and B.9, respectively, cancel by the spectral division in equation 4.9. The denominator of these Green's functions are the multiple scattered contributions in the Green's function after a series expansion.

The time domain expression for the series expansion of equation 4.9 is

$$R_0(z_a, t) = r_1 \delta(t - t_1) + E(t > t_1), \tag{4.10}$$

where $E(t > t_1)$ are the events in R_0 that occur for $t > t_1$. Equation 4.10 tells us that the contribution to the image after applying the deconvolution imaging condition $R_0(z_a, t = 0)$ is zero at z_a, as there are no contributions at zero time. This vanishing contribution to the image is expected since we do not have any interface at z_a.

We now consider R_0 at the second interface z_1 in Figure 4.1. The reflection response R_0 given by the division of equations B.14 and B.15 yields

$$\begin{aligned} R_0(z_1, z_1, \omega) &= \frac{G^-(z_1, z_0, \omega)}{G^+(z_1, z_0, \omega)}, \\ &= \frac{r_1 + r_2 e^{-2i\omega t_2}}{1 + r_1 r_2 e^{-2i\omega t_2}}. \end{aligned} \tag{4.11}$$

Similarly, the time domain expression for the series expansion of equation 4.11 is

$$R_0(z_1, z_1, t) = r_1 \delta(t) + E(t > 0), \tag{4.12}$$

where $E(t > 0)$ are the events in R_0 that occur for $t > 0$. Therefore, considering equation 4.12, the contribution to the deconvolution imaging $R_0(z_1, z_1, t = 0)$ at the second interface z_1 is r_1. This imaging condition result $R_0(z_1, z_1, t = 0)$= r_1 corresponds to the actually reflection coefficient at the second interface r_1.

Note that the multiples reflections that are embedded in the denominator of equations B.14 and B.15 are removed by the spectral division of G^- and G^+ (equation 4.11) to produce the image, while at zero time only the first term in the expansion contribute to the image. This is in agreement with the conclusions of Snieder (1990a,b) that the multiples are removed in the inversion to produce the image, while only the first Born approximation term, i.e. the primary reflections, contribute to the image. We emphasize that for R_0 at the interface and at zero time, the primary reflections alone, contribute to the construction of the image.

Numerical investigation

Using equation 4.8, we apply the deconvolution-imaging condition to the up- and down-going Green's function for the numerical model given in Figure 4.2. The corresponding image is shown in Figure 4.6. and matches the true reflectivity of the actual model (solid black line).

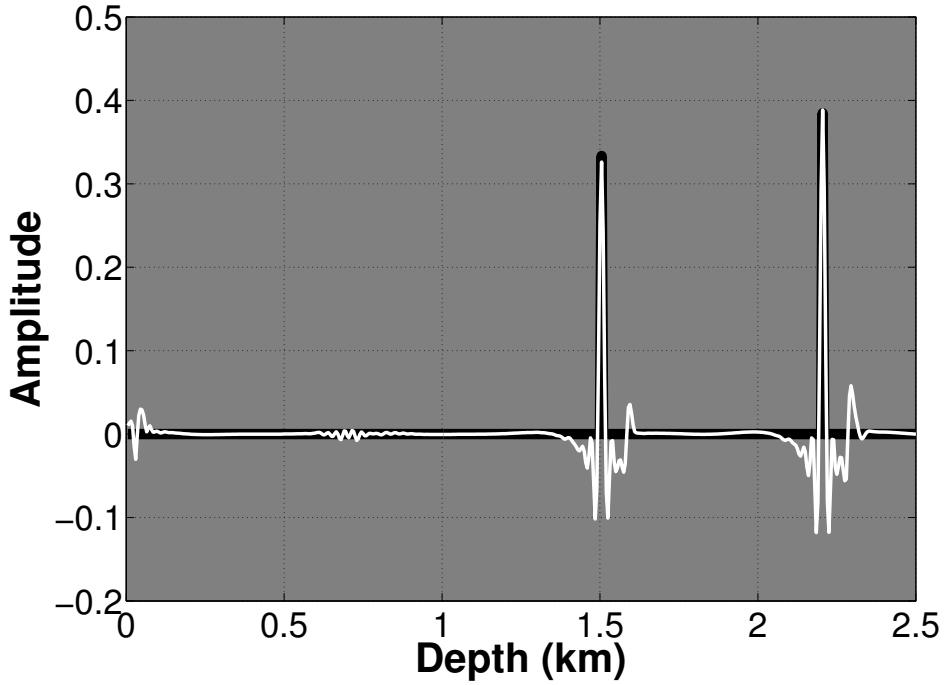

Figure 4.6: Deconvolution-imaging condition constructed from the same up- and down-going retrieved Green's functions used in the correlation imaging section. The black line represents the exact reflection coefficient of the model in Figure 4.2.

Figure 4.6 conforms well to the conclusions we have made in the analytical work of this section: 1) there are no artifacts in Figure 4.6 due to kinematically similar events in the up- and down-going Green's function at 0.7 km compared to the correlation image in Figure 4.5 2) the deconvolution image obtains the correct reflection coefficients at the two interfaces of the model, Figure 4.2, as we exactly solve for R_0 in 1D. There is a weak artifact in the deconvolution image at 0.7 km; however these relatively negligible events, compared to the events at the interface, are due to deconvolution numerical error and the finite recording time of the reflection response at the surface. Therefore, in Table Table 4.1 there are ticks (✓) under *true reflectivity imaging* and *no false interfaces* for deconvolution imaging in 1D, which is corroborated by the analytical and numerical investigation.

4.2.3 Imaging Condition- Marchenko Redatuming

We obtain the reflection response in 1D, below an arbitrary point in the model by also solving equation 4.1 for R_0, as previously stated. We call this reflection response the redatumed reflection response $R_0(z_i, z_i, t)$ since we can interpret $R_0(z_i, z_i, t)$, at depth z_i, as the reflection response for a source at z_i and for receivers at z_i, while above z_i the medium is homogeneous. Since the redatumed response $R_0(z_i, z_i, t)$ contains the reflection events below the arbitrary chosen datum, we can use this response to image below an arbitrary datum z_i; thus ignoring the overburden reflection. R_0 include internal multiples from reflections below z_i; therefore RTM imaging with R_0 will still have artifacts due to the presence of internal multiples generated below z_i.

Analytical investigation

The redatumed response is obtained by solving equation 4.1. In our 1D analytical model, we solve for R_0 using deconvolution, equation 4.8. At z_a (center of first layer), equation 4.10, including some higher order terms, gives the redatumed response $R_0(z_a, z_a, t)$ at depth z_a:

$$\begin{aligned} R_0(z_a, z_a, t) = & \, r_1\delta(t - t_1) + r_2\delta(t - t_1 - 2t_2) \\ & - r_1^2 r_2\delta(t - t_1 - 2t_2) - r_1 r_2^2\delta(t - t_1 - 4t_2) \\ & + r_1^3 r_2^2\delta(t - t_1 - 4t_2) + E(t > t_1 - 4t_2) \\ = & \, r_1\delta(t - t_1) + \tau_1^2 r_2\delta(t - t_1 - 2t_2) + \tau_1^2 r_1 r_2^2\delta(t - t_1 - 4t_2) + E(t > t_1 - 4t_2). \end{aligned} \tag{4.13}$$

In the last line of equation 4.13, the first three events on the right-hand side are verified in the schematic in Figure 4.7; notice that we account for transmission through the interfaces.

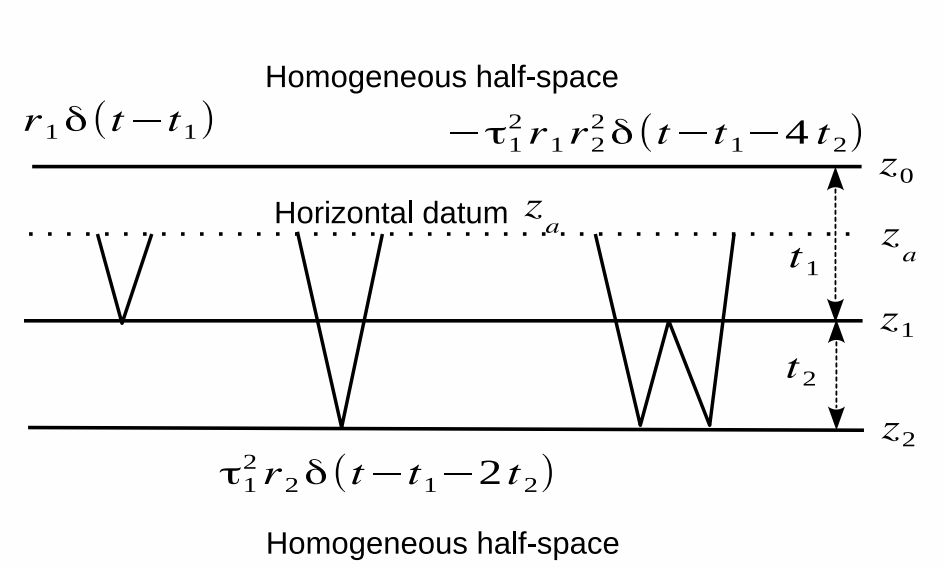

Figure 4.7: Schematic of a few events in the redatumed reflection response, equation 4.13 at z_a for the model in Figure 4.1.

$R_0(z_a, z_a, t)$ (equation 4.13) not only includes the primary events but also the internal multiples and these reflection events have the correct amplitudes (see Figure 4.7). Therefore, we can use this redatumed reflection response $R_0(z_a, z_a, t)$ for imaging, which ignores the reflections from above z_a.

Numerical investigation

For our numerical model in Figure 4.2, we compute the redatumed reflection response at $z = 1.75$ km in Figure 4.8. This response is the deconvolution of the up- and down-going Green's functions at the virtual receiver and source at $z = 1.75$ km, below the first layer in Figure 4.2, i.e. $R_0(z, z, t)$. Below the virtual source at $z = 1.75$ km, our model has one interface at $z = 2.2$ km with a reflection coefficient of 0.38, which is retrieved in the redatumed response in Figure 4.8 at 0.35 seconds. We can now use R_0 to image the interface at 2.2 km from above, i.e. at 1.75 km,

using any imaging technique that uses reflection recordings to construct an image of the subsurface. Therefore, we obtain the redatumed reflection response (with correct amplitudes and kinematics of

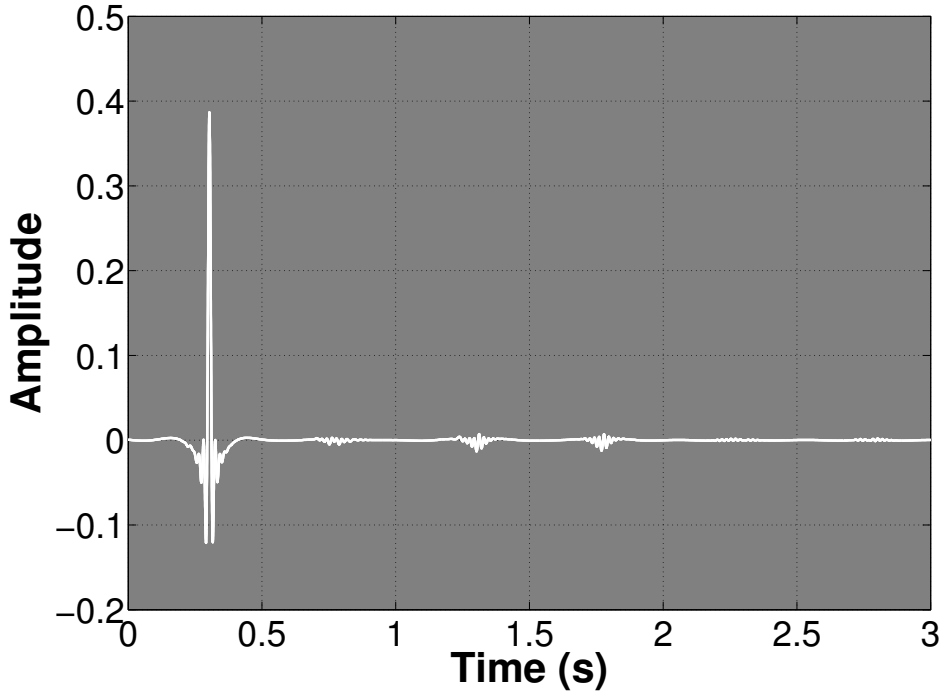

Figure 4.8: Redatumed reflection response at $1.75\ km$ for the model in Figure 4.2. Note that below $1.75\ km$ is one interface with a reflection coefficient of 0.38.

events) below an arbitrary datum by using deconvolution but not correlation, see Table Table 4.1.

4.2.4 Imaging Condition- First arrival of G^+ with G^-

In this subsection we propose using the first arrival of G^+ (defined as G_f^+) and G^- for imaging the subsurface. We begin our analysis with Figure 4.3 to analyze the snapshots of the Green's function. Up to 0.8 seconds (Figure 4.3(b) and Figure 4.3(c)), the first arrival of G^+ (G_f^+) interacts with the two interfaces to generate up-going reflections, i.e. G^-, (G_f^+ and G^- kinematically similar at the interface). Therefore when G_f^+ reaches the interface, we get a contribution to the image. We can use both the correlation imaging condition and the deconvolution imaging condition for imaging the subsurface with G_f^+ and G^-.

Analytical investigation

For the analytical model given in Figure 4.1, at z_a (center of first layer), the first arrival of G^+ is $G_f^+ = \tau_0 \delta(t - \frac{1}{2}t_1)$. Since there are no events with similar times in $G_f^+(z_a, z_0, t)$ and $G^-(z_a, z_0, t)$ in equation 4.4, the contribution to the correlation image at z_a is zero. The other events in G^+, apart from the first arrivals, are the internal multiples or free-surface multiples. In the correlation imaging section, these multiples in G^+ contribute to false interfaces in the image (for example, at 0.7 km in Figure 4.4).

The deconvolution of $G^-(z_a, z_0, t)$ (equation B.8) with $G_f^+(z_a, z_0, t)$ in the frequency domain yields

$$\begin{aligned}\widetilde{R_0}(z_a, z_a, \omega) &= \frac{G^-(z_a, z_0, \omega)}{G_f^+(z_a, z_0, \omega)} = \frac{\tau_0 \dfrac{r_1 e^{-\frac{3}{2}i\omega t_1} + r_2 e^{-i\omega(\frac{3}{2}t_1 + 2t_2)}}{1 + r_0 r_1 e^{-2i\omega t_1} + r_0 r_2 e^{-2i\omega(t_1+t_2)} + r_1 r_2 e^{-2i\omega t_2}}}{\tau_0 e^{-\frac{1}{2}i\omega t_1}} \\ &= \frac{r_1 e^{-i\omega t_1} + r_2 e^{-i\omega(t_1+2t_2)}}{1 + r_0 r_1 e^{-2i\omega t_1} + r_0 r_2 e^{-2i\omega(t_1+t_2)} + r_1 r_2 e^{-2i\omega t_2}}, \end{aligned} \tag{4.14}$$

where $\widetilde{R_0}(z_a, z_a, \omega)$ is not equal to $R_0(z_a, z_a, \omega)$ (equation 4.9); we are not solving equation 4.8 since we limit the down-going Green's function to its first arrival. The time domain series expansion of equation 4.14 is

$$\begin{aligned}\widetilde{R_0}(z_a, z_a, t) = {} & r_1\delta(t - t_1) + r_2\delta(t - t_1 - 2t_2) + \\ & - r_0 r_1^2 \delta(t - 3t_1) - r_0 r_1 r_2 \delta(t - 3t_1 - 2t_2) \\ & - r_0 r_1 r_2 \delta(t - 3t_1 - 2t_2) + \dots . \end{aligned} \tag{4.15}$$

The deconvolution imaging of $\widetilde{R_0}(z_a, z_a, t = 0)$ (equation 4.15) is zero since there are no terms at zero time, which matches perfectly with the analytical model (no interface). $\widetilde{R_0}(z_a, z_a, t)$, for non-zero times, includes spurious events when compared to the correct redatumed response R_0 given in equation 4.13. Consequently, standard imaging with $\widetilde{R_0}$ as the reflection response would include these spurious events as false interfaces.

At z_1, the first arrival of $G^+(z_1, z_0, t) = G_f^+(z_1, z_0, t) = \tau_0 \delta(t - t_1)$. The correlation image of the analytical model with $G_f^+(z_1, z_0, t)$ and with $G^-(z_1, z_0, t)$ has a contribution at z_1. This contribution is due to the fact that the first term in $G^-(z_1, z_0, t)$ (equation 4.7) is at the same time as

$G_f^+(z_1, z_0, t)$. (Kinematically similar events correspond to a contribution to the correlation image). The amplitude of this contribution is $\tau_0^2 r_1$ which differs from the true reflectivity at $z_1 = r_1$, see Table Table 4.1.

Similarly, we can apply deconvolution, equation 4.8, to $G_f^+(z_1, t)$ and $G^-(z_1, t)$, in the frequency domain, this reads

$$\begin{aligned}\widetilde{R_0}(z_1, z_1, \omega) &= \frac{G^-(z_1, z_0, \omega)}{G_f^+(z_1, z_0, \omega)}, \\ &= \frac{r_1 + r_2 e^{-i\omega 2t_2}}{1 + r_0 r_1 e^{-2i\omega t_1} + r_0 r_2 e^{-2i\omega(t_1+t_2)} + r_1 r_2 e^{-2i\omega t_2}}. \end{aligned} \tag{4.16}$$

Following a similar procedure in the deconvolution imaging section, the time domain expansion of equation 4.16 is

$$\widetilde{R_0}(z_1, z_1 t) = r_1 \delta(t) + E(t > 0). \tag{4.17}$$

Consequently, the deconvolution image, $\widetilde{R_0}$ at zero time at z_1 is r_1, the true reflectivity at this location, as shown in Table Table 4.1. Thus, although we are not solving for the true reflection response R_0, our deconvolution image, using $G_f^+(z_1, t)$ and $G^-(z_1, t)$, at $\mathbf{time = 0}$ seconds is correct.

Since $G_f^+(z_1, t)$ excludes the multiples in G^+, we are producing the image at zero time with only the first-order Born terms. We already know that all the multiples are subtracted in the inversion to obtain the image (Snieder, 1990a,b), therefore it should come as no surprise that we produce similar images when using $G_f^+(z_1, t)$ and $G^-(z_1, t)$ or the complete $G^+(z_1, t)$ and $G^-(z_1, t)$.

Numerical investigation

Our imaging fields for the model in Figure 4.2 are the first arrivals of the retrieved down-going Green's functions G_f^+ and the up-going Green's functions G^-. A smooth version of the velocity model can be used, in general, to mute G^+ to get its first arrival, G_f^+.

We follow the correlation and deconvolution imaging procedures for imaging with G_f^+ and G^-. Figure 4.9 and Figure 4.10 shows the corresponding correlation image and deconvolution image, respectively.

Note that the correlation image, Figure 4.9, has no false interfaces around 0.7 km compared to Figure 4.5, because G_f^+ does not include any multiples only the first arrival of G^+. The free-surface multiple labeled A in Figure 4.3(e), no longer exist in G_f^+ and therefore do no contribute to a false interface. However, the amplitudes of the reflectors for the correlation image still do not match the true reflectivity even though the image do not include false interfaces, as illustrated in Table Table 4.1.

The deconvolution image, Figure 4.10, matches the true reflectivity of the model (solid black line), despite approximating G^+ with G_f^+. We do not get the artifacts at 0.7 km in Figure 4.10 compared to Figure 4.6 (deconvolution image with G^+ and G^-). Therefore imaging with G_f^+ and G^- removes the false interface at 0.7 km and gives the correct reflectivity of the subsurface. However, we do not reconstruct the correct redatumed response $R_0(z, z, t)$, as summarized in Table Table 4.1.

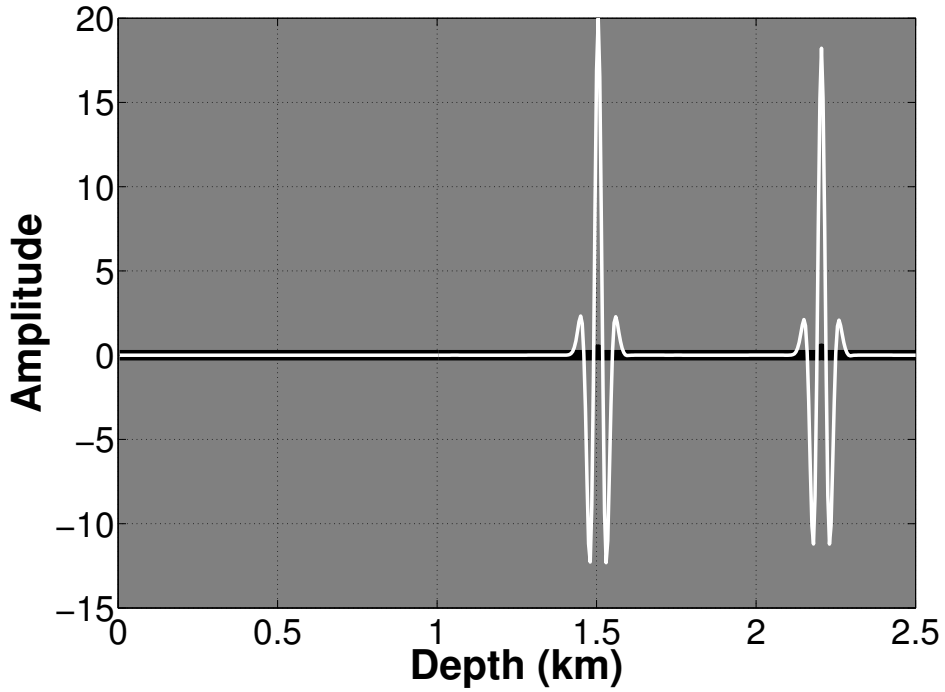

Figure 4.9: Correlation-imaging of the first arrival of the down-going Green's function with the up-going Green's function for the model in Figure 4.2.

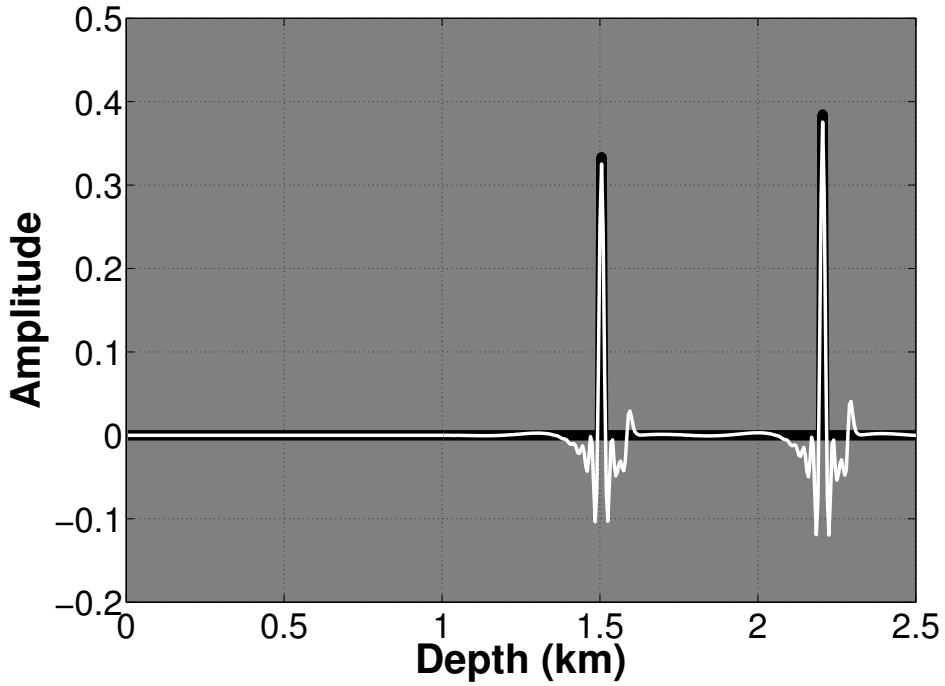

Figure 4.10: Deconvolution-imaging of the first arrival of the down-going Green's function with the up-going Green's function for the model in Figure 4.2.

4.3 2D strategies for imaging

The equations that govern imaging of the retrieved Green's functions in multidimensions are similar to the imaging equations in 1D, except in 2D they have an additional horizontal space variable. In 2D, an analytical investigation of Marchenko imaging with the different imaging conditions are not feasible, thus we restrict our analysis to a numerical investigation.

In this section, the spatial coordinates are defined by their horizontal and depth components; for instance $\mathbf{x_0} = (\mathbf{x_{H,0}}, x_{3,0})$, where $\mathbf{x_{H,0}}$ are the horizontal coordinates at a depth $x_{3,0}$. Similar to the 1D section superscript $(+)$ refers to down-going waves and $(-)$ to up-going waves at the observation point $\mathbf{x}$.

The governing equation for imaging with up- and down-going wavefields in 2D is

$$G^{-}(\mathbf{x_i'}, \mathbf{x_0''}, t) = \int_{\partial D_i} d\mathbf{x_i} \int_{-\infty}^{\infty} G^{+}(\mathbf{x_i}, \mathbf{x_0''}, t - t') R_0(\mathbf{x_i'}, \mathbf{x_i}, t') dt', \tag{4.18}$$

where ∂D_i is an arbitrary depth level and R_0 is the reflection response of the medium below ∂D_i (Amundsen, 2001; Claerbout, 1985; Wapenaar et al., 2008b). Unlike the 1D equation 4.1, there is an additional integration over space $\mathbf{x_i}$. Note that $R_0(\mathbf{x_i'}, \mathbf{x_i}, t)$ is the reflection response for sources and receivers on ∂D_i, with the medium above ∂D_i being homogeneous. The image of the subsurface in 2D is not only the reflection response R_0 at zero time but also zero offset $R_0(\mathbf{x_i}, \mathbf{x_i}, t = 0)$. Note that the summary in Table Table 4.1 holds for both 1D and multidimensions, so we will not repeat the imaging analysis in the previous section (where the 1D imaging section rigorously analyzed Marchenko imaging with different imaging conditions) but instead, we compare Marchenko imaging with conventional RTM.

We utilize the velocity and density models in Figure 4.11 and Figure 4.12, respectively, to compute the reflection response R at the surface. The reflection response R includes primaries, internal and free-surface multiples. We use the reflection response at the surface as inputs for all imaging examples in this section. Our goal is to image a target area in the subsurface, which is enclosed by the box in Figure 4.11; the zoomed in area of the velocity, is shown in Figure 4.13.

We first show the image we obtain from RTM in Figure 4.14. We construct the RTM image by evaluating the correlation of the back propagated reflection response and forward propagated source function in the smooth velocity model given in Figure 4.15 at zero time and zero-offset. We call this the RTM correlation imaging condition; which is different from the correlation imaging condition previously mentioned that uses the up- and down-going Green's functions. The RTM image in Figure 4.14 is a zoomed-in version of the entire image at the target area. The free-surface multiples generated by the syncline above the target area as well as internal multiples contaminate the image in Figure 4.14 when compare to the model of the target area in Figure 4.13.

We now investigate Marchenko imaging of the target area in Figure 4.13 with the following imaging conditions: 1) correlation, 2) multidimensional deconvolution, 3) deconvolution. We compare the images generated by these imaging conditions constructed with either G^+ and G^- or with G_f^+ and G^-. In addition, we include subsection 4.3.4 that uses the redatumed reflection response to image the subsurface. Note that the associated Marchenko images are constructed

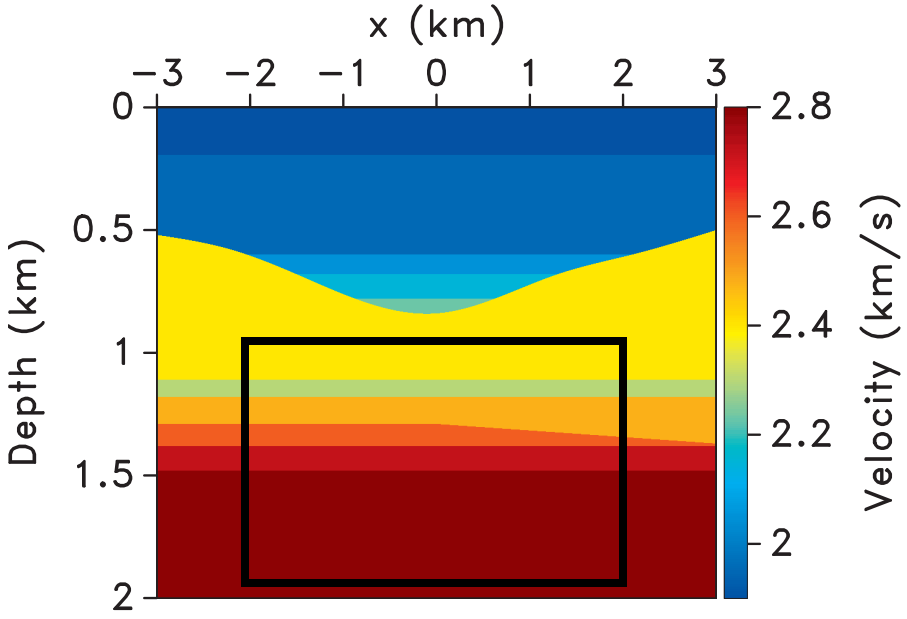

Figure 4.11: The velocity model used in the 2D imaging section. The black box bounds the target area.

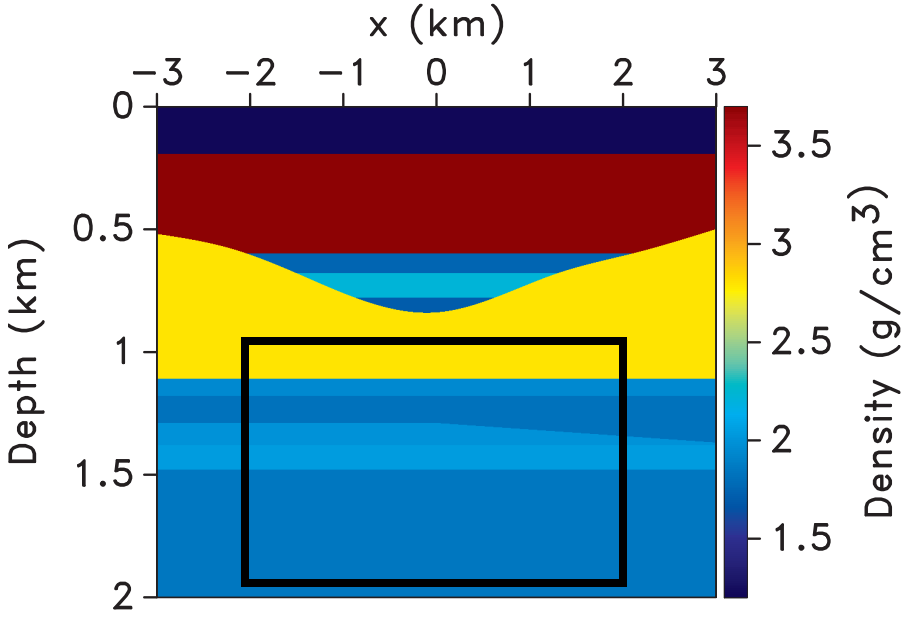

Figure 4.12: The density model ranging used in the 2D imaging section. The black box bounds the target area.

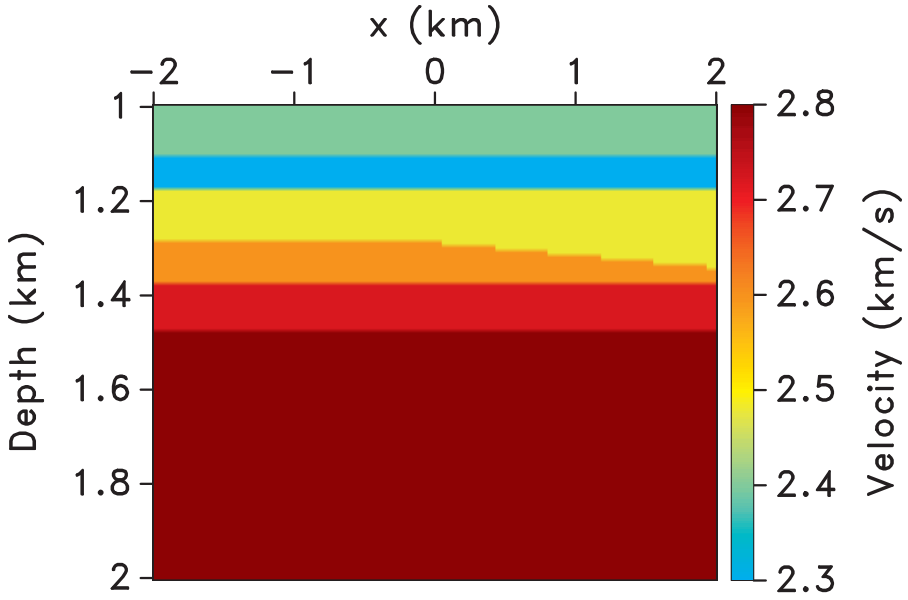

Figure 4.13: Target zone in the numerical model (velocity) where we conduct imaging. Note we do not use this model to implement Marchenko imaging, we use a smooth version of the velocity model (Figure 4.11) only.

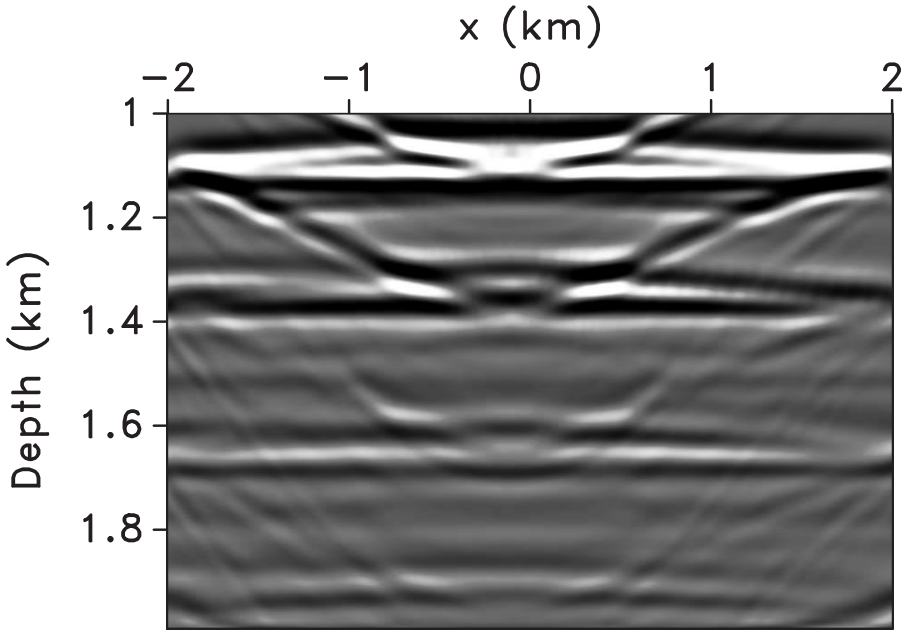

Figure 4.14: Zoomed in image of the reverse time migration for the model in Figure 4.13 below the syncline structure (in the target area). The reflection response used for imaging includes primaries, internal multiples and free-surface multiples.

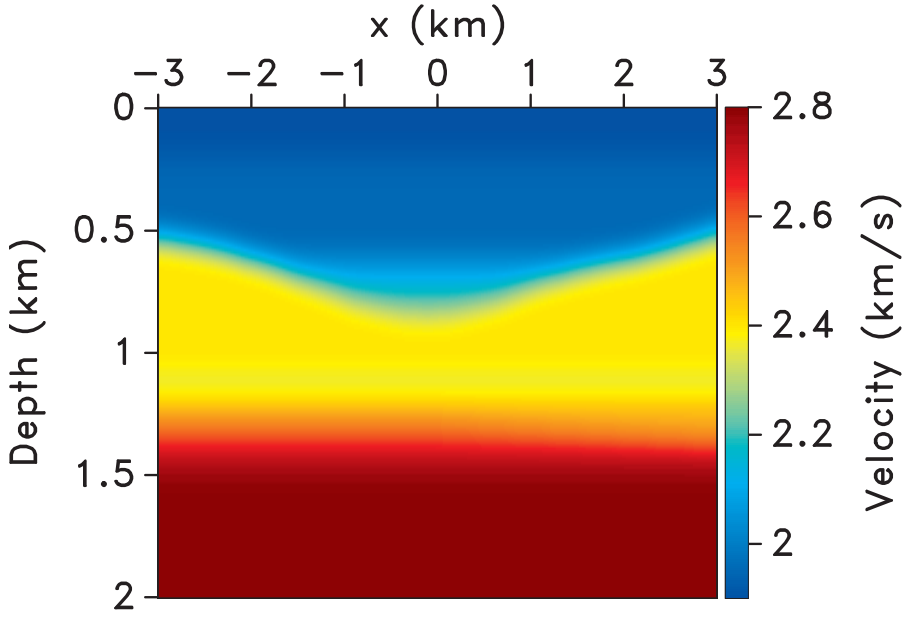

Figure 4.15: Macro-model, i.e. smooth version of Figure 4.11, used to compute the first arrivals from the virtual source location to the surface.

from the same inputs as RTM, i.e. the reflection response at the surface and the smooth velocity model in Figure 4.15. We begin with the correlation imaging condition using the retrieved Green's function.

4.3.1 Correlation imaging in 2D

The multi-dimensional correlation in the frequency domain for the retrieved up- and down-going Green's function is

$$C(\mathbf{x_i}, \mathbf{x_i'}, \omega) = \int_{\partial D_0} G^-(\mathbf{x_i}, \mathbf{x_0''}, \omega) G^+(\mathbf{x_i}, \mathbf{x_0''}, \omega)^* d\mathbf{x_0''}. \tag{4.19}$$

The integral of $C(\mathbf{x_i}, \mathbf{x_i}, \omega)$ over all frequencies at zero-offset is the correlation imaging condition. Conversely, in the time domain, the correlation imaging condition is the zero-offset and zero time contribution of equation 4.2, $C(\mathbf{x_i}, \mathbf{x_i}, t = 0)$. The correlation image using the retrieved Green's functions are shown in Figure 4.16.

We construct each image point independently of the other image points and therefore, we build a subset of the image; this process is called target-oriented imaging. Figure 4.16 is obtained by

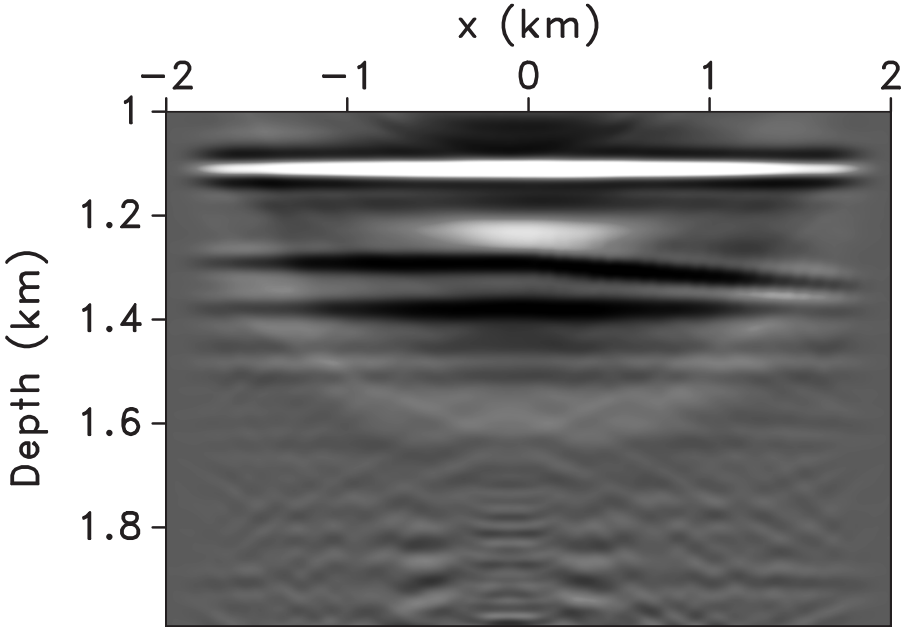

Figure 4.16: Marchenko correlation imaging of the model in Figure 4.13 in the target zone.

computing the Green's function $G^{\pm}(\mathbf{x_0''}, \mathbf{x_i'}, t)$ at the surface for virtual receivers, at intervals of 4 m, in the target area; the image is the superposition of the correlation imaging condition at each Green's function virtual receiver location. In the Marchenko image in Figure 4.16 the reflectors are clearly discernible and match the interfaces in the target area in Figure 4.13. In the imaging box the artifacts from the free-surface and internal multiples are no longer visible compared to the RTM image in Figure 4.14.

4.3.2 Multidimensional Deconvolution imaging

As mentioned earlier, solving equation 4.18 for R_0 in 1D requires deconvolution, equation 4.8. However, in higher dimension, we solve equation 4.18 for R_0 by multidimensional deconvolution. In the frequency domain, equation 4.18 becomes

$$G^{-}(\mathbf{x_i'}, \mathbf{x_0''}, \omega) = \int_{\partial D_i} G^{+}(\mathbf{x_i}, \mathbf{x_0''}, \omega) R_0(\mathbf{x_i'}, \mathbf{x_i}, \omega) d\mathbf{x_i}. \tag{4.20}$$

To solve equation 4.20 (discussed in Wapenaar et al. (2014b)), we first multiply both sides of the equation by G^+ and integrate over source positions at the acquisition surface x_0'' to yield

$$C(\mathbf{x_i'}, \mathbf{x_i'''}, \omega) = \int_{\partial D_i} \Gamma(\mathbf{x_i'}, \mathbf{x_i'''}, \omega) R_0(\mathbf{x_i}, \mathbf{x_i'}, \omega) d\mathbf{x_i}, \tag{4.21}$$

where the correlation function C is given in equation 4.19 and the point-spread function is given by

$$\Gamma(\mathbf{x_i'}, \mathbf{x_i'''}, \omega) = \int_{\partial D_i} G^+(\mathbf{x_i'}, \mathbf{x_0''}, \omega) G^+(\mathbf{x_i'''}, \mathbf{x_0''}, \omega) d\mathbf{x_0''}. \tag{4.22}$$

We invert equation 4.21 for $R_0(\mathbf{x_i}, \mathbf{x_i'}, \omega)$ (van der Neut et al., 2011; Wapenaar et al., 2008b). The multi-dimensional deconvolution imaging condition is $R_0(\mathbf{x_i}, \mathbf{x_i}, t = 0)$ (the reflection response R_0 at zero-offset and at time = zero seconds). To construct the image, we compute $R_0(\mathbf{x_i}, \mathbf{x_i}, t = 0)$ at every sampled point in the image.

The Marchenko images constructed with correlation and MDD yield similar results; however, as a more instructive approach to compare these images, we show a trace at $x_1 = (-0.2)$ km below 1 km for each of the corresponding images (see Figure 4.17). The traces in Figure 4.17 show that 1) MDD matches the true reflectivity better than the other imaging conditions, 2) the events in the traces (MDD and correlation) correspond to the interfaces in the actual model at the right locations. The true reflectivity trace in Figure 4.17 is constructed by computing the reflection coefficients at zero offset at $x_1 = (-0.2)$ km below 1 km, then convolving this trace with the Ricker wavelet used in finite difference modeling of the reflection response at the surface.

4.3.3 Deconvolution imaging 2D

Multidimensional deconvolution requires the Green's functions along the horizontal datum ∂D_i to construct an image at a point $\mathbf{x_i}$ on ∂D_i. Strictly speaking, this MDD image is not imaging at a particular target as we require the Green's functions along the datum ∂D_i. Target oriented imaging is the image at a point using only the Green's function at that point. Similar to correlation imaging, deconvolution imaging requires only the Green's function at the virtual receiver location to construct the image at that location, hence this is target-oriented imaging.

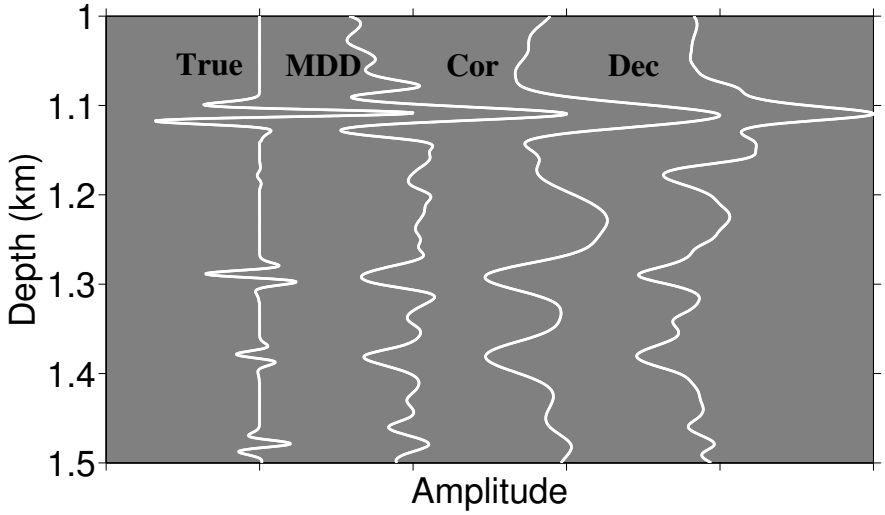

Figure 4.17: Comparison of the imaging conditions: multidimensional deconvolution (MDD), correlation (Cor), and deconvolution (Dec), of the down-going Green's function with the up-going Green's function for the model in Figure 4.13 at horizontal location -0.2 km in the target area.

Deconvolution imaging in 2D is the trace by trace deconvolution of the up-and down-going Green's functions at each virtual receiver location at zero offset and zero time $R_0(\mathbf{x}, \mathbf{x}, t = 0)$. Alternative techniques on the implementation of the deconvolution imaging condition are given by Schleicher et al. (2007). The deconvolution image yield similar results to correlation, therefore we show a trace of the deconvolution image for a closer analysis (see Figure 4.17). The trace of the deconvolution image in Figure 4.17 places the reflector at the correct location but it does not match the true reflectivity of the model as is also summarized in Table Table 4.1. The traces of the correlation and deconvolution are scaled to match the reflectivity of the interface at 1.1 km because neither correlation nor deconvolution give the true reflection coefficients; however in 1D, deconvolution imaging does match the true reflectivity as explained in the 1D imaging section.

4.3.4 Imaging with the redatumed reflection response in 2D

Similar to the 1D example on redatuming, we use the up- and down-going Green's function at virtual receivers $\mathbf{x}'_{\mathbf{i}} = (-2\ to\ 2, 1)$ km to compute the redatumed reflection response R_0 given in equation 4.18, and we use this response to image the subsurface using standard imaging algorithms.

To retrieve the redatumed response $R_0(\mathbf{x_i}, \mathbf{x_i'}, t)$ accurately we solve equation 4.21 by MDD. We perform RTM using the redatumed response $R_0(\mathbf{x_i}, \mathbf{x_i'}, t)$ at $\mathbf{x_i} = (-2\ to\ 2, 1)$ km to image the target area (see Figure 4.18). The RTM correlation imaging condition is used to construct the redatumed RTM in Figure 4.18 and the RTM with surface recordings in Figure 4.14.

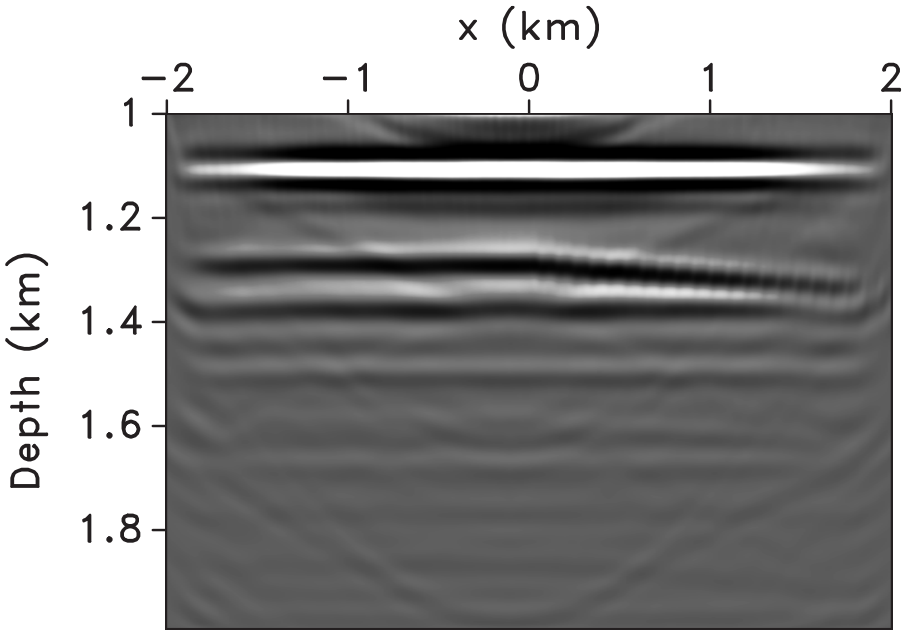

Figure 4.18: RTM of the redatumed reflection response in the target area.

In Figure 4.18 the artifacts are dramatically reduced compared to the RTM image in Figure 4.14. Specifically, the multiples from the syncline structure are not present in the image in Figure 4.18 using the redatumed response compared to the RTM in Figure 4.14. This reduction in artifacts is a result of the fact that the redatumed reflection response R_0 only includes the reflections below 1 km. The redatumed reflection response still, however includes internal multiples from the interfaces below the redatuming depth. Therefore, the redatumed RTM image does in fact have artifacts from such internal multiples, for instance at z=1.68 km in Figure 4.18, but they are significantly weaker than the reflections caused by the overburden, i.e. the syncline reflections (see Figure 4.14). In higher dimensions, trace by trace deconvolution does not solve for R_0 in equation 4.18 (as we have the integral over space $d\mathbf{x_i'}$ on the right hand side which we do not account for) and therefore we cannot use R_0 obtained by deconvolution to perform imaging of the subsurface

by standard imaging algorithms.

4.3.5 Imaging with the first arrival of G^+ and G^- in 2D

We performed correlation, deconvolution, and MDD imaging condition using G_f^+ and G^-; the images are the same as the images constructed with G^+ and G^- using the same imaging conditions for our 2D examples. Figure 4.19 shows a comparison between the true reflectivity, a trace from the MDD imaging with G^+ and G^-, and MDD imaging with G_f^+ and G^-. As expected from the 1D imaging section, imaging with G^+ and G^- or imaging with G_f^+ and G^- gives similar contributions at the interfaces. However, similar to the 1D imaging section, using G_f^+ and G^- does not give the

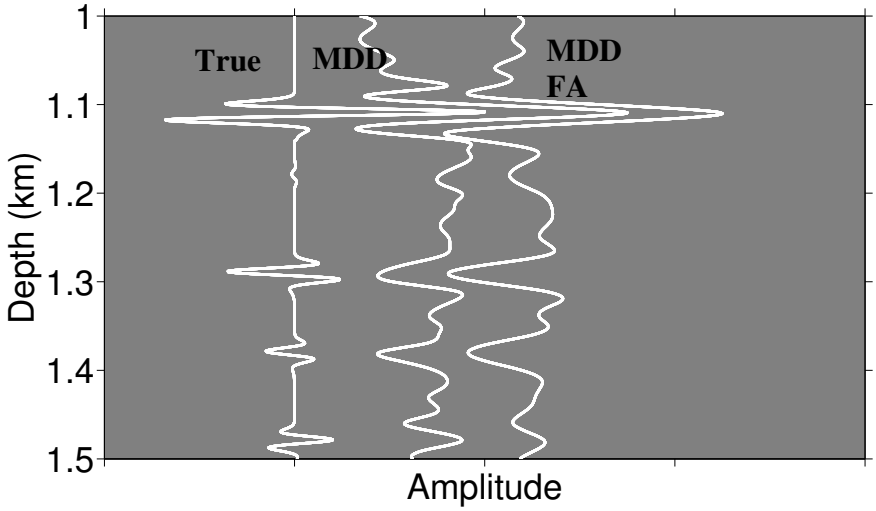

Figure 4.19: Multidimensional deconvolution imaging of first arrival of down-going Green's function with up-going Green's function (MDD FA) for the model in Figure 4.13 at horizontal location -0.2 km in the target area compared to the true reflectivity and MDD imaging with the complete one-way Green's functions.

correct redatumed response, and hence cannot be used to create an image below the redatuming depth.

4.4 Discussion

The findings of this paper are summarized in Table Table 4.1. Starting with the first imaging condition in Table Table 4.1, correlation imaging with the retrieved Green's function gives

false interfaces caused by the interaction of the reflections in G^+ and in G^-. A false interface in Marchenko correlation imaging is due to events in G^+ which exist at the same time as events in G^-. At the interface however, all the waves in G^+ arrive at the same time as all the waves in G^-. Therefore at the interface, the stacking of all the kinematically similar events is generally larger than at a false interface.

The multidimensional deconvolution imaging condition applied to G^+ and G^- yields a good match with the true reflectivity and minimizes false interfaces as MDD is the theoretically accurate way to solve for the image compared to the other methods in this paper. Note that, in the imaging step, for instance equation 4.11, the denominators of G^+ and G^- (the multiple reflections in G^+ and G^-) cancel out. Therefore G^+ and G^- must either have all the multiples included or both G^+ and G^- must be truncated in such a way that they (G^+ and G^-) include the same order of multiples to have the multiples removed in the imaging step. (Failure to include the same order of multiples in G^+ and G^- creates false interfaces in the imaging step.) However in practice, it is not feasible to know if we have the same order of multiples in G^+ and G^-. For this reason, it is more advantageous to use the first arrival of G_f^+ and G^- as we do not need to match the order of multiples in the up- and down-going fields while still matching the true reflectivity and avoiding false interfaces.

Note that all imaging conditions using G_f^+ and G^- result in comparable or better images than using G^+ and G^-. The most advantageous use of G_f^+ and G^- is in the correlation imaging condition, where the false interfaces are completely removed.

Even though MDD with G^+ and G^- does give the correct redatumed response with accurate reflection amplitudes, applying standard imaging to the corresponding redatumed response does not necessarily mean that the resulting image will be free of false interfaces. These false interfaces are caused by the internal-multiple reflections below the datum level. However, the images constructed by the redatumed response are void of overburden reflections.

4.5 Conclusion

Even though Marchenko imaging reduces the artifacts caused by multiples compared to standard imaging algorithms, these artifacts are still present. Theoretically, the correct procedure to image with the retrieved Green's functions is MDD and therefore best matches the correct image of the subsurface compared to other Marchenko imaging conditions. However, instead of using G^+ and G^-, Marchenko imaging with the first arrival of the down-going Green's function G_f^+ and the associated up-going Green's function G^-, removes these artifacts corresponding to false interfaces. Despite the fact that G_f^+ does not contain the reflection events, the resulting multidimensional deconvolution image better matches the true reflectivity of the model compared to standard imaging or Marchenko imaging with correlation or deconvolution. Note that since only the primaries contribute to the construction of the image while the multiples are implicitly removed in the inversion process to produce the image, it suffices to only use G_f^+ and G^- compared to G^+ and G^- in the imaging.

Importantly, the inputs for Marchenko imaging are exactly the same as most standard imaging techniques; a smooth version of the velocity and the reflection response at the surface. Unlike standard imaging techniques, in Marchenko imaging, we do not need to remove the free-surface or internal multiples from the reflection response, as the Marchenko equations in this paper properly handle these multiples.

4.6 Acknowledgments

We thank Kees Wapenaar (Delft University), Joost van Der Neut (Delft University), Ivan Vasconcelos (Schlumberger Gould Research), Esteban Diaz (CWP) for fruitful discussions. We are grateful to Diane Witters for her help in preparing this manuscript. This work was funded by the sponsor companies of the Consortium Project on Seismic Inverse Methods for Complex Structures and by Shell Research. The 2D reflection response in this paper is generated with the finite difference package in Thorbecke and Draganov (2011).

CHAPTER 5

BEYOND MARCHENKO – OBTAINING VIRTUAL RECEIVERS AND VIRTUAL SOURCES IN THE SUBSURFACE

By solving the Marchenko equations, the Green's function can be retrieved between a virtual receiver in the subsurface to points at the *surface* (no physical receiver is required at the virtual location). We extend the idea of these equations to retrieve the Green's function between any two points in the *subsurface*; i.e, between a virtual source and a virtual receiver (no physical source or physical receiver is required at either of these locations). This Green's function is called the virtual Green's function and includes all the primaries, internal and free-surface multiples. Similar to the Marchenko Green's function, we require the reflection response at the surface (single-sided illumination) and an estimate of the first arrival travel time from the virtual location to the surface.

5.1 Introduction

We propose a method to retrieve the Green's function between two points in the subsurface of the Earth. We call these two points a virtual source and a virtual receiver pair. To retrieve the Green's function at a virtual receiver for a virtual source we require neither a physical source nor a physical receiver at the virtual source and receiver. The requirements for the retrieval of this Green's function is the reflection response for physical sources and physical receivers at the surface (single sided-illumination) and a smooth version of the velocity model (no small-scale details of the model are necessary). For brevity we define this Green's function i.e., the response of a virtual source recorded at a virtual receiver, as the *Virtual Green's function*. We label the method of retrieving the *Virtual Green's function* as the modified Marchenko method.

Similar ideas of retrieving the Green's function between two points have been proposed in seismic interferometry (Bakulin and Calvert, 2006; Curtis et al., 2006; Curtis and Halliday, 2010; Curtis et al., 2009; Snieder et al., 2007; van Manen et al., 2006; Wapenaar, 2004) and in the Marchenko method (Broggini and Snieder, 2012; Broggini et al., 2012; Singh et al., 2015, 2016;

Slob et al., 2014; Wapenaar et al., 2013a, 2014b). However, these methods (interferometry and Marchenko method) have more restrictions in the source-receiver geometry, as discussed later, for the accurate retrieval of the Green's function than our proposed method (modified Marchenko method).

In seismic interferometry, we create virtual sources at locations where there are physical receivers. We also require a closed surface of sources to adequately retrieve the Green's function. Unlike interferometry, a physical receiver or physical source is not needed by our modified Marchenko method to create either a virtual source or a virtual receiver and we only require single-sided illumination (a closed surface of sources not needed). The Green's function retrieved by the Marchenko equations is the response of virtual source in the subsurface recorded at **physical receivers** at the **surface** (Broggini and Snieder, 2012; Broggini et al., 2012; Singh et al., 2015, 2016; Slob et al., 2014; Wapenaar et al., 2013a, 2014b). The Marchenko retrieved Green's function requires neither a physical source nor a physical receiver at the virtual source location in the subsurface.

Our algorithm retrieves the Green's function (both up- and down-going at the receiver) for virtual sources and virtual receivers. The Marchenko-retrieved Green's functions are limited to virtual sources in the subsurface recorded at the **surface** but the Modified Marchenko method (our Work) is not restricted to recording on the surface for each virtual source. In our method, the response of the virtual source can be retrieved for a virtual reciever anywhere in the **subsurface**.

Wapenaar et al. (2016) has proposed similar work to ours, but their approach retrieves (1) the two-way virtual Green's function while our work retrieves the up- and down- going (one-way) virtual Green's function, the summation of these one-way Green's function gives the two-way Green's function, and (2) the homogeneous Green's function while we retrieve the causal Green's function.

We discuss in this paper the theory of retrieving the virtual Green's function. Our numerical examples are split into three sections (1) A verification of our algorithm to demonstrate that we retrieve the up- and down-going virtual Green's function (using a 1D example for simplicity) (2) A complicated 1D example illustrating our algorithm accurately retrieves the Green's function

with the free-surface multiples and without the free-surface multiples (3) A 2D numerical example of the virtual Green's function constructed in such a way that we create a wavefield with all the reflections and first arrivals from a virtual source. This last numerical example is complicated since the discontinuities in the density and the velocity are at different locations.

5.2 Theory

To retrieve the Green's function from a virtual receiver in the subsurface for *sources on the surface*, one solves the Marchenko equations. The retrieval only requires the reflection response at the surface and an estimate of the first arrival travel-time from the virtual receiver to the surface. The retrieved Green's function can either include free-surface multiples (Singh et al., 2015, 2016) or exclude these multiples (Broggini and Snieder, 2012; Broggini et al., 2012; Slob et al., 2014; Wapenaar et al., 2013a, 2014b).

In addition to the retrieved Green's function, the Marchenko equations also gives us the one-way focusing functions. These functions are outputs from the Marchenko equations that exist at the acquisition level ∂D_0 (acquisition surface) and focus on an arbitrary depth level ∂D_i at $t = 0$ (time equal zero).

The focusing functions are auxiliary wavefields that reside in a truncated medium that has the same material properties as the actual inhomogeneous medium between ∂D_0 and ∂D_i and that is homogeneous above ∂D_0 and reflection-free below ∂D_i (Slob et al., 2014). Therefore, the boundary conditions on ∂D_0 and ∂D_i in the truncated medium, where the focusing function exists, are reflection-free, see Figure 5.1. Our algorithm moves the sources of the Green's function retrieved by Marchenko equations from the surface into the subsurface at a virtual point with the help of the focusing function.

In this paper, the spatial coordinates are defined by their horizontal and depth components; for instance $\mathbf{x_0} = (\mathbf{x_{H,0}}, x_{3,0})$, where $\mathbf{x_{H,0}}$ are the horizontal coordinates at a depth $\mathbf{x_{3,0}}$. Superscript $(+)$ refers to down-going waves and $(-)$ to up-going waves at the observation point $\mathbf{x}$. Additionally, any variable with a subscript 0 (e.g., R_0) indicates that no free-surface is present.

One-way reciprocity theorems of the convolution and correlation type, equations 5.1 and 5.2 respectively, are used to relate up- and down-going fields at arbitrary depth levels to each other in different wave states (Wapenaar and Grimbergen, 1996). The one-way reciprocity theorems of the convolution and correlation type are

$$\int_{\partial D_0} [p_B^+ p_A^- - p_B^- p_A^+] d\mathbf{x_0} = \int_{\partial D_i} [p_B^+ p_A^- - p_B^- p_A^+] d\mathbf{x_i}, \tag{5.1}$$

$$\int_{\partial D_0} [(p_B^+)^* p_A^+ - (p_B^-)^* p_A^-] d\mathbf{x_0} = \int_{\partial D_i} [(p_B^+)^* p_A^+ - (p_B^-)^* p_A^-] d\mathbf{x_i}, \tag{5.2}$$

where the asterisk * denotes complex conjugation, the subscripts A and B are two wave states, and ∂D_0 and ∂D_i are arbitrary depth levels.

The correlation reciprocity theorem, equation 5.2, is based on time reversal invariance of our wavefields, which implicitly assumes that the medium is lossless. Since we assume the wavefields can be decomposed into up- and down-going waves, we ignore evanescent waves; hence all our results obtained from equations 5.1 and 5.2 are spatially band-limited (Wapenaar et al., 2004a). More details on one-way reciprocity can be obtained in Wapenaar (1998), Wapenaar et al. (2001), and Wapenaar et al. (2004b).

Wave state A is defined for the truncated medium and P_A is the focusing function. The one-way wavefields for wave state A for a source at $\mathbf{x_i'}$ are given in Table Table 5.1 and Figure 5.1.

Table 5.1: The wavefields of the focusing function f_1 and Green's functions at the acquisition surface ∂D_0 and the level ∂D_i. $p_A^\pm$ symbolizes one-way wavefields in the frequency domain for wave state A, at arbitrary depth levels in the reference medium, see Figure 5.1 while $p_B^\pm$ symbolizes one-way wavefields at arbitrary depth levels in the inhomogeneous medium in wave state B, where $\mathbf{r}$ is the reflection coefficient of the free surface, see Figure 5.2.

	State A	State B
On ∂D_0:	$p_A^+ = f_1^+(\mathbf{x_0}, \mathbf{x_i'}, \omega)$	$p_B^+ = rG(\mathbf{x_0}, \mathbf{x_j''}, \omega)$
	$p_A^- = f_1^-(\mathbf{x_0}, \mathbf{x_i'}, \omega)$	$p_B^- = G(\mathbf{x_0}, \mathbf{x_j''}, \omega)$
On ∂D_i:	$p_A^+ = f_1^+(\mathbf{x_i}, \mathbf{x_i'}, \omega) = \delta(\mathbf{x}_H - \mathbf{x}'_H)$	$p_B^+ = G^+(\mathbf{x_i}, \mathbf{x_j''}, \omega)$
	$p_A^- = f_1^-(\mathbf{x_1}, \mathbf{x_i'}, \omega) = 0$	$p_B^- = G^-(\mathbf{x_i}, \mathbf{x_j''}, \omega)$

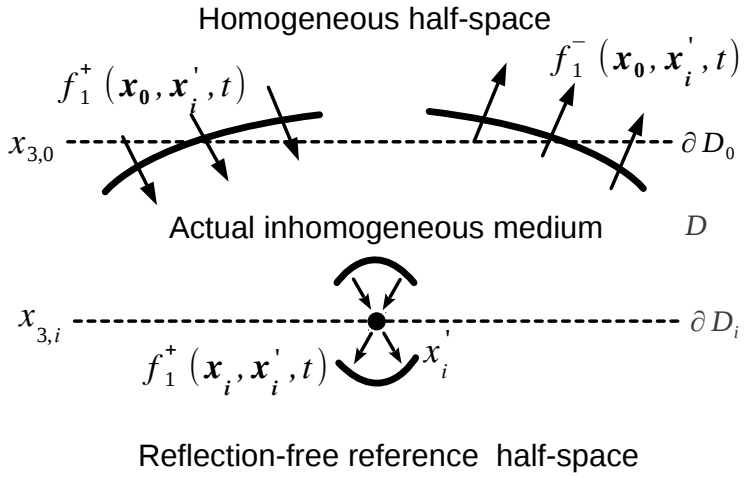

Figure 5.1: Up- and down-going focusing function $f_1^{\pm}$ that focuses at $\mathbf{x_i'}$ in the truncated medium. This medium is homogeneous above ∂D_0 and below ∂D_i and is equal to the real medium between ∂D_0 and ∂D_i.

The Green's functions in the actual medium is defined as wave state B. The one-way wavefields for wave state B, the actual medium, for a source at $\mathbf{x}_j''$ are given in Table Table 5.1 and Figure 5.2. These Green's functions are retrieved using the Marchenko equations and include the primary, internal, and free-surface multiple reflections of the actual medium (Singh et al., 2015, 2016).

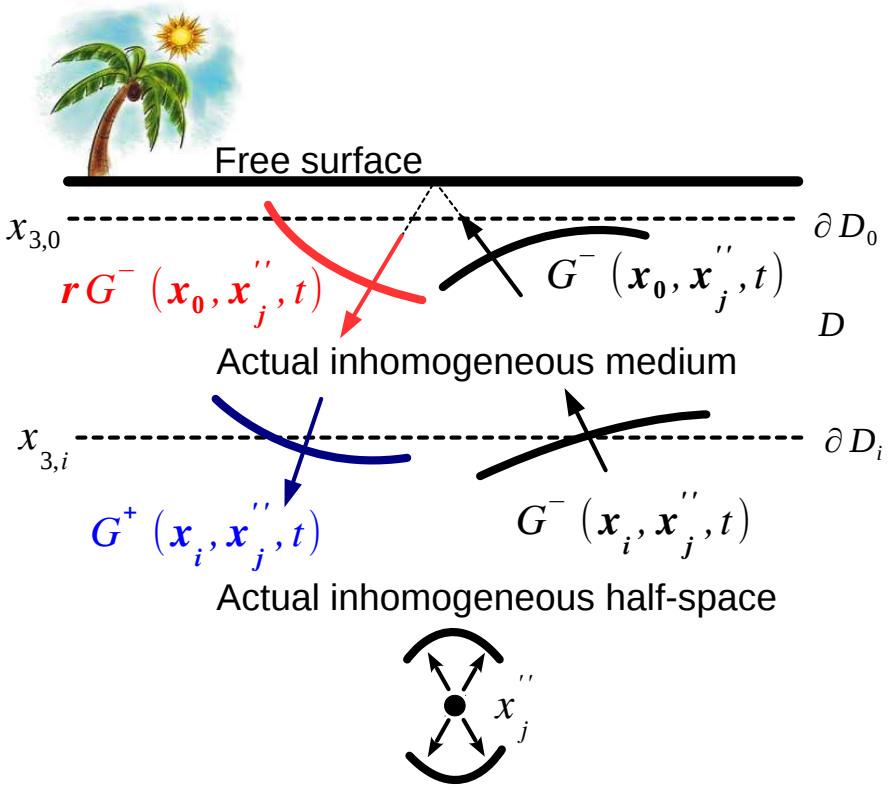

Figure 5.2: The Green's functions in the actual inhomogeneous medium in the presence of a free surface at the acquisition surface ∂D_0 and the arbitrary surface ∂D_i. The tree indicates the presence of the free surface.

We substitute the one-way wavefields described in Table Table 5.1 into equations 5.1 and 5.2 and use the sifting property of the delta function to yield

$$G^-(\mathbf{x_i}', \mathbf{x_j}'', \omega) = \int_{-\infty}^{\infty} [G^-(\mathbf{x_0}, \mathbf{x_j}'', \omega) f_1^+(\mathbf{x_0}, \mathbf{x_i}', \omega) - rG^-(\mathbf{x_0}, \mathbf{x_j}'', \omega) f_1^-(\mathbf{x_0}, \mathbf{x_i}', \omega)] d\mathbf{x_0}, \quad (5.3)$$

$$G^{+}(\mathbf{x_i}^{'}, \mathbf{x_j}^{''}, \omega)^{*} = \int_{-\infty}^{\infty} [rG^{-}(\mathbf{x_0}, \mathbf{x_j}^{''}, \omega)^{*} f_1^{+}(\mathbf{x_0}, \mathbf{x_i}^{'}, \omega) - G^{-}(\mathbf{x_0}, \mathbf{x_j}^{''}, \omega)^{*} f_1^{-}(\mathbf{x_0}, \mathbf{x_i}^{'}, \omega)] d\mathbf{x_0}, \quad (5.4)$$

where r denotes the reflection coefficient of the free surface (in the examples shown in this paper $r = -1$.)

Equations 5.3 and 5.4 yield the up- and down-going virtual Green's functions, respectively, for a virtual receiver at $\mathbf{x_i}'$ and a virtual source at $\mathbf{x_j}''$ in the subsurface. Note, we are not limited to the source $\mathbf{x_j}''$ being below the receiver $\mathbf{x_i}'$ since by reciprocity, $G(\mathbf{x_i}^{'}, \mathbf{x_j}^{''}, t)$ = $G(\mathbf{x_j}^{''}, \mathbf{x_i}^{'}, t)$.

To compute the up- and down-going virtual Green's function in equations 5.3 and 5.4, we require 1) the Green's function $G^{-}(\mathbf{x_0}, \mathbf{x_j}^{''}, \omega)$ at the surface $\mathbf{x_0}$ for a virtual source at $\mathbf{x_j}''$ and 2) the focusing function $f^{\pm}(\mathbf{x_0}, \mathbf{x_i}', \omega)$ at the surface $\mathbf{x_0}$ for a virtual source at $\mathbf{x_i}'$. We retrieve both these functions by solving the Marchenko equations.

We can also retrieve the virtual Green's function which does not include free-surface multiples by simply setting the reflection coefficient at the free-surface r to zero in equations 5.3 and 5.4. Thus, the equation to retrieve the virtual Green's function without the presence of a free surface is

$$G_0^{-}(\mathbf{x_i}^{'}, \mathbf{x_j}^{''}, \omega) = \int_{-\infty}^{\infty} G_0^{-}(\mathbf{x_0}, \mathbf{x_j}^{''}, \omega) f_1^{+}(\mathbf{x_0}, \mathbf{x_i}^{'}, \omega) d\mathbf{x_0}, \quad (5.5)$$

$$G_0^{+}(\mathbf{x_i}^{'}, \mathbf{x_j}^{''}, \omega)^{*} = -\int_{-\infty}^{\infty} G_0^{-}(\mathbf{x_0}, \mathbf{x_j}^{''}, \omega)^{*} f_1^{-}(\mathbf{x_0}, \mathbf{x_i}^{'}, \omega) d\mathbf{x_0}, \quad (5.6)$$

where $G_0^{\pm}(\mathbf{x_i}^{'}, \mathbf{x_j}^{''}, \omega)$ is the up- and down-going Green's function without free-surface multiples for a virtual receiver at $\mathbf{x_i}^{'}$ and virtual source at $\mathbf{x_j}^{''}$.

5.3 Numerical examples

To show a proof of concept for our algorithm, we begin with a simple 1D numerical example. Our model consists of two homogeneous layers separated by an interface at $0.5\ km$ with constant density and velocity in each layer and a free surface. At the interface, the velocity changes from $2\ km$ to $2.8\ km$, while the density changes from $1\ g/cm^3$ to $2.5\ g/cm^3$.

Our objective is to retrieve the virtual up- and down-going Green's function $G^{\pm}(\mathbf{x_i'}, \mathbf{x_j''}, \omega)$ at the virtual receiver $\mathbf{x_i'} = 0.25\ km$ for a virtual source at $\mathbf{x_j''} = 1.75\ km$, a schematic of these waves is shown in Figure 5.3. To retrieve the virtual Green's function, we solve equations 5.3 and 5.4. These equations (5.3 and 5.4) require at the surface $\mathbf{x_0}$: 1) the focusing function $f^{\pm}(\mathbf{x_0}, \mathbf{x_i'}, t)$ and 2) the Green's function $G(\mathbf{x_0}, \mathbf{x_j''}, t)$; with their virtual source locations are at $\mathbf{x_i'}$ and $\mathbf{x_j''}$, respectively. The focusing functions are up- and down-going at the surface ∂D_0 and are shaped to focus at the virtual receiver $\mathbf{x_i'} = 0.25\ km$ for $t = 0$.

We retrieve the one-way focusing functions at the surface by solving the Marchenko equations (Singh et al., 2015, 2016). The down-going focusing function is shown in Figure 5.4 in blue (normalized by its maximum amplitude). Since the medium between the surface and the focusing point is homogeneous, the up-going focusing function vanishes as it suffices to only have a down-going focusing function to create a focus at $\mathbf{x_i'} = 0.25\ km$ (see Figure 5.4).

The Green's function $G(\mathbf{x_0}, \mathbf{x_j''}, t)$ (in the right-hand side of equations 5.3 and 5.4) needed for our virtual Green's function (in the left-hand side of equations 5.3 and 5.4) is retrieved by the Marchenko equations as well. $G(\mathbf{x_0}, \mathbf{x_j''}, t)$ includes free-surface multiples, internal multiples, and primaries. $G(\mathbf{x_0}, \mathbf{x_j''}, t)$ is the response of a virtual source at $\mathbf{x_j''} = 1.75\ km$ recorded at the surface ∂D_0, see Figure 5.4.

In order to solve the Marchenko equation, to obtain the focusing functions $f^{\pm}(\mathbf{x_0}, \mathbf{x_i'}, t)$ and the Green's function $G(\mathbf{x_0}, \mathbf{x_j''}, t)$; and consequently the virtual Green's function from equations 5.3 and 5.4, we require the reflection response at the acquisition level (which includes all multiples and primaries) and an estimate of the travel-time from each of the virtual points to the acquisition level.

By substituting $G(\mathbf{x_0}, \mathbf{x_j''}, t)$ and $f_1^{\pm}(\mathbf{x_0}, \mathbf{x_i'}, t)$ (shown in Figure 5.4) into equations 5.3 and 5.4 and adding the corresponding up- and down-going virtual Green's function, we obtain the two-way virtual Green's function $G(\mathbf{x_i'}, \mathbf{x_j''}, t)$ recorded at a virtual receiver located at $\mathbf{x_i'} = 0.25\ km$ and a virtual source at $\mathbf{x_j''} = 1.75\ km$, see Figure 5.5. This illustrates that we can accurately retrieve the virtual Green's function as there is minimal mismatch with the modeled Green's function (in

black) (source at 1.75 km and receiver at 0.25 km). The modeled Green's function is computed using finite differences with the exact velocity and density.

Figure 5.3 shows a schematic of a few of the up- (solid lines) and down-going (dashed lines) events at the virtual receiver for the virtual Green's function in our one-interface model. These events (numbered) in Figure 5.3 corresponds to the retrieved virtual up- and down-going Green's functions in Figure 5.6, at the correct travel-times; hence confirming the proof of concept of our one-way equations in 5.3 and 5.4.

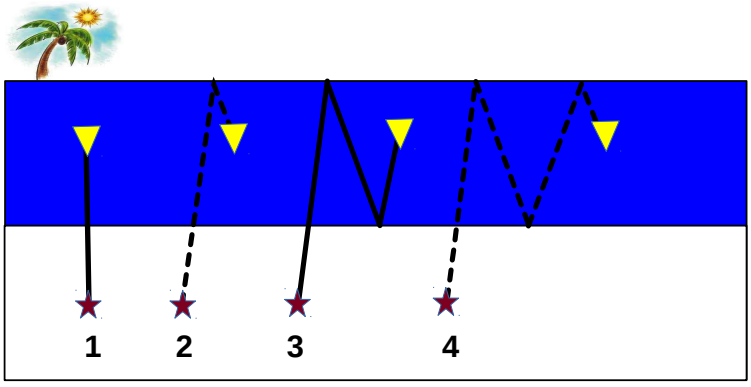

Figure 5.3: Schematic of the up- and down-going events at the receiver position for the simple 2 layer model. Solid lines represent up-going while dotted events represent down-going events.

The second example illustrates the retrieval of the virtual Green's function without the free-surface reflections (Figure 5.7) for the 1D model given in Figure 5.8 with the virtual source and receiver shown by the red and blue dots, respectively. This example also contains variable density, with discontinuities at the same depth as the velocity model, with densities ranging from $1\ gcm^{-3}$ to $3\ gcm^{-3}$. As shown in Figure 5.7, there is an almost perfect match between the modeled Green's function and the retrieved virtual Green's function.

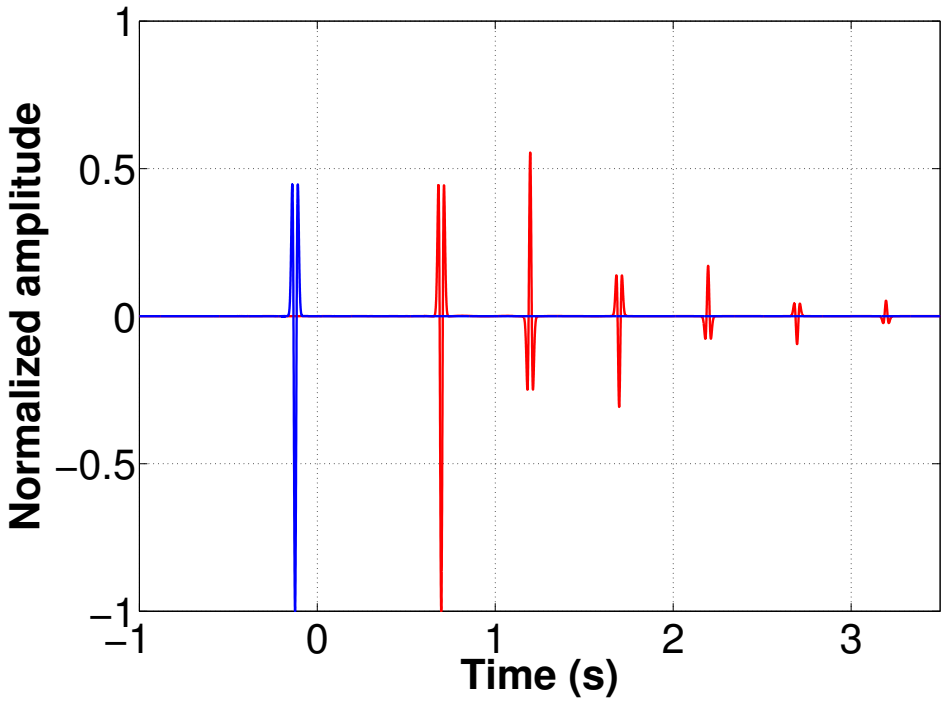

Figure 5.4: The input wavefields required for equations 5.4 and 5.3: The two-way Green's functions $G(\mathbf{x_0}, \mathbf{x_j''}, t)$ (in red) retrieved by the Marchenko equations in the presence of a free surface for $\mathbf{x_j''} = 1.75\ km$ and the down-going focusing function $f^+(\mathbf{x_0}, \mathbf{x_i'}, t)$ (in blue) also retrieved by the Marchenko equations for $\mathbf{x_i'} = 0.25\ km$.

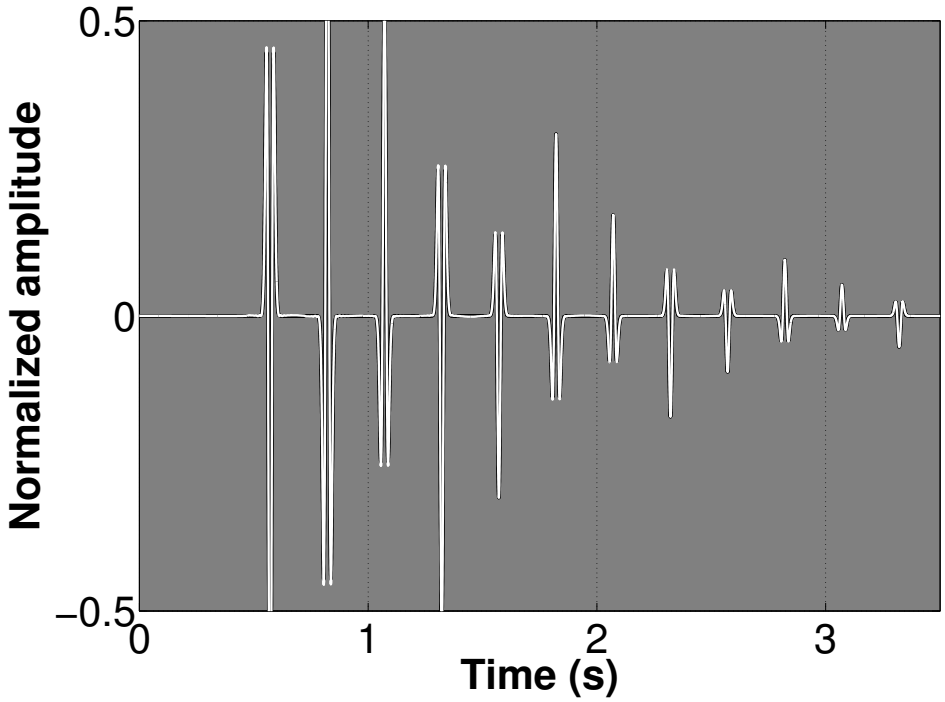

Figure 5.5: Green's function with virtual source $\mathbf{x}_j''$ at depth 1.75 km and recording at the virtual receiver $\mathbf{x}_i'$ at depth 0.25 km. The black thicker line is the modeled Green's function, superimposed on it is the retrieved Green's function. Each trace is divided by its maximum amplitude hence the y-axis label is called normalized amplitude. The plot limits are chosen between 0.5 to -0.5 normalized amplitude to visualize the smaller amplitude events better.

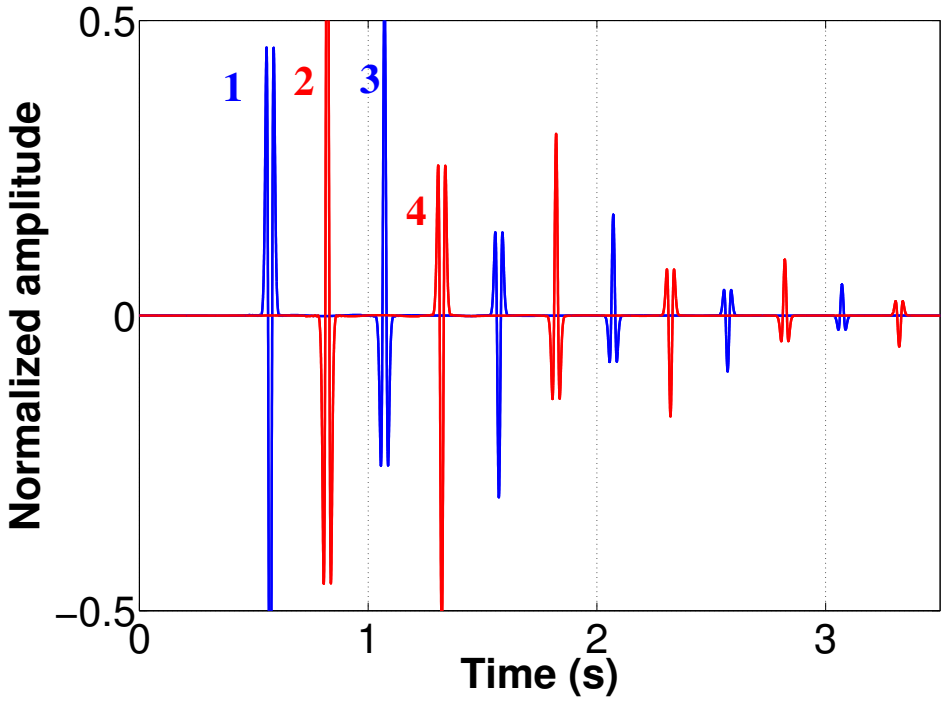

Figure 5.6: The up- (blue line) and the down-going (red line) Green's function with the numbers in Figure 5.3 corresponding to the the appropriate event.

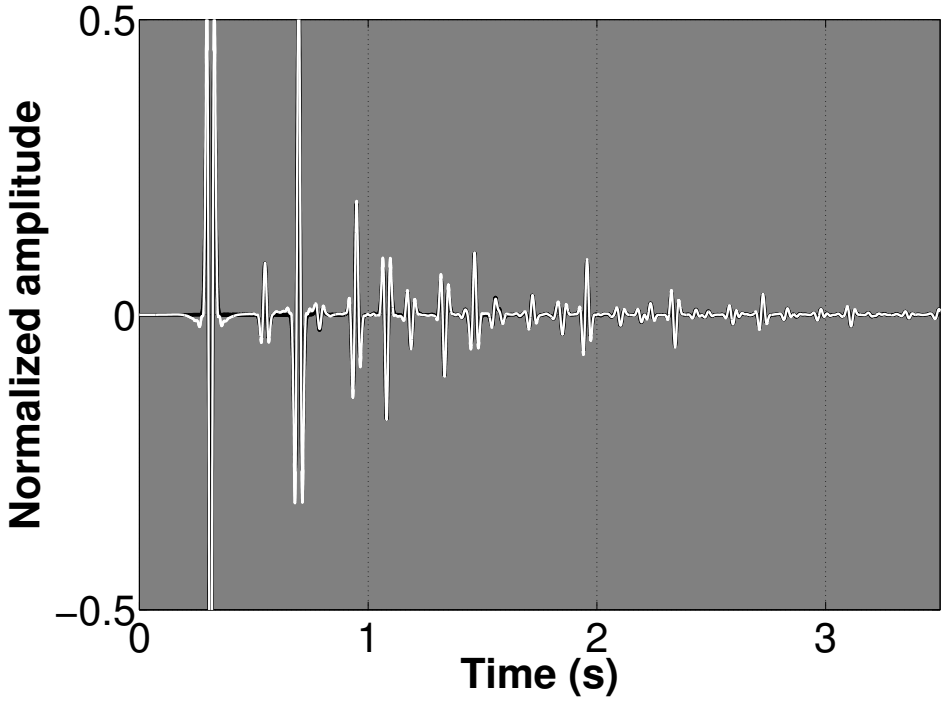

Figure 5.7: Virtual Green's function (white line) with virtual source $\mathbf{x}_j''$ at depth 1.75 km and recording at the virtual receiver $\mathbf{x}_i'$ at depth 0.75 km superimposed on it the modeled Green's function (black line). Both Green's functions do not include free-surface multiples.

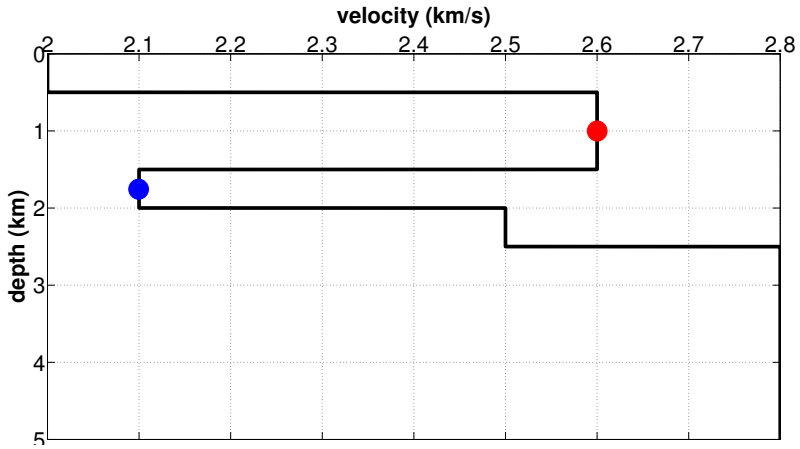

Figure 5.8: 1D velocity model with a free surface. The red dot at 0.75 km is the location of the virtual receiver while the blue dot at 1.75 km is the position of the virtual source for the retrieved virtual Green's function.

Figure 5.9 is the virtual Green's function using the same model in Figure 5.8 but with free-surface multiples. Note the increased reflections and complexity the free surface introduces (Figure 5.9) compared to the case without the free surface (Figure 5.7). The match between the modeled Green's function and the retrieved Green's function using our algorithm is almost exact, see Figure 5.9.

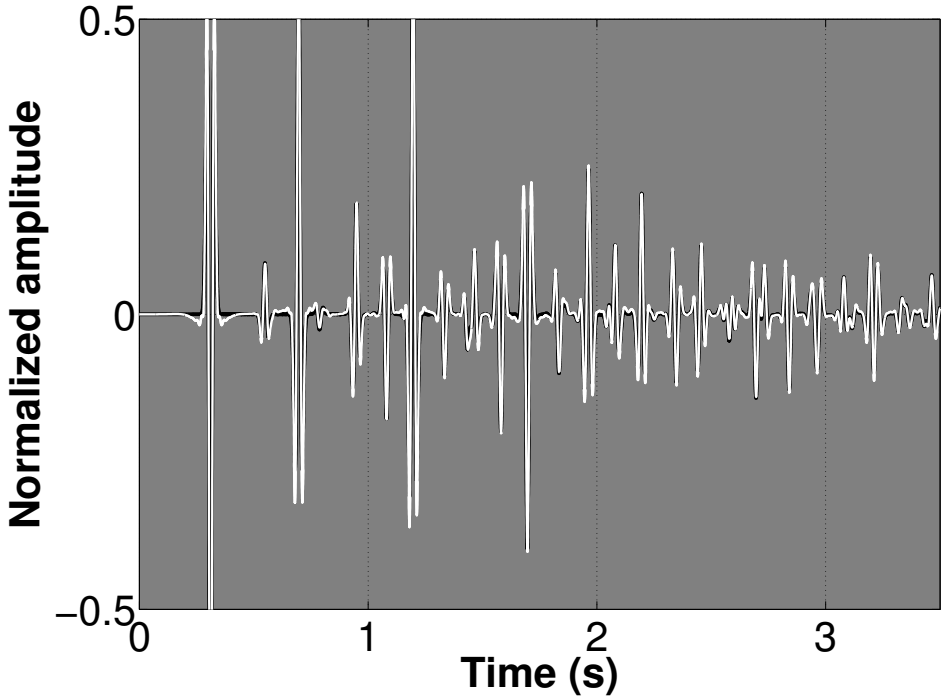

Figure 5.9: Virtual Green's function with free-surface multiples (white line) with virtual source x_j'' at depth 1.75 km and recording at the virtual receiver x_i' at depth 0.75 km for the model in Figure 5.8 with a free surface. The modeled Green's function is superimposed on it which also includes the free-surface multiples (black line).

The 1D numerical examples have *perfect* aperture, hence, the 1D examples almost perfectly match the retrieved virtual Green's function to the modeled Green's function. The equations to obtain the virtual Green's function are multidimensional. We next show a 2D numerical example of the virtual Green's function in a velocity and density model shown in Figure 5.10 and Figure 5.11, respectively. Notice that the discontinuities and the dip of the interfaces in the velocity are different from those in the density.

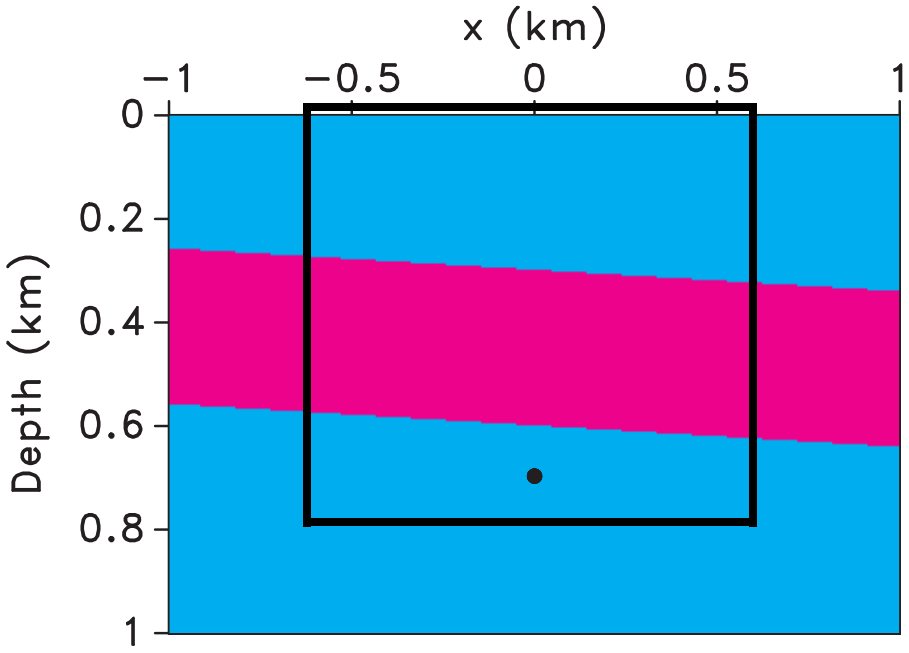

Figure 5.10: Two-interface velocity model with velocities ranging from 2.0 to 2.4 km/s. The dot shows the position of the virtual source for the virtual Green's function and the black box is the target zone where we place virtual receivers.

Our algorithm allows us to place virtual receivers and virtual sources in any target location in the subsurface. For our numerical example, we retrieve the virtual Green's function $G(\mathbf{x}'_\mathbf{i}, \mathbf{x}''_\mathbf{j}, t)$, Figure 5.12, where $\mathbf{x}'_\mathbf{i}$ are the virtual receivers populating the target location at every 32 m (black box in Figure 5.10) and $\mathbf{x}''_\mathbf{j} = (0, 0.7)\ km$ is the virtual source (black dot in Figure 5.10). In Figure 5.12 notice:

1. In panel b, the first arrival from the virtual source $\mathbf{x}''_\mathbf{j} = (0, 0.7)\ km$ and the reflection from the bottom velocity layer.

2. In panels c and d, the inability of our algorithm to handle the horizontal propagating energy of the first arrival from the virtual source, hence the dimming on the sides of the first arrival of the virtual Green's function. To retrieve near-horizontally propagating events (in this case, these waves are not evanescent) especially in the first arrival of the virtual Green's function, we require a much larger aperture than is used in this example. Note that the later arriving

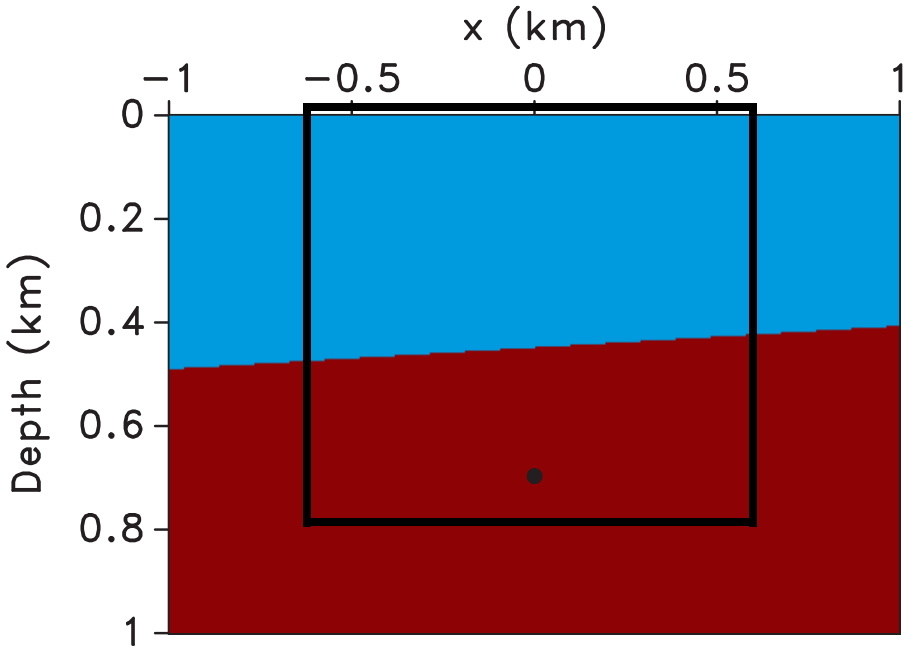

Figure 5.11: One-interface density model with densities ranging from 2.0 to 3.0 g/cm^3. The dot shows the position of the virtual source for the virtual Green's function and the black box is the target zone where we place virtual receivers.

up- and down-ward propagating waves are retrieved accurately at the depth of the virtual source $\mathbf{x}_j'' = (0, 0.7)$ km in Figure 5.12, panel d and e, since the reflections are purely up- and down-going.

3. In panels c and d, we do however, retrieve the reflections from the density layer (pink line in Figure 5.12) although we did not use any explicit information of the density model in our numerical retrieval of the virtual Green's function.

4. In panel f, a free-surface multiple is present. As expected, there is a polarity change of the free surface multiple compared to the incident wave at the top of panel e due to the interaction of this wave in panel e with the free surface.

5. In panel h, we obtain the up-going reflections caused by the free-surface multiple interacting with the velocity and density layer.

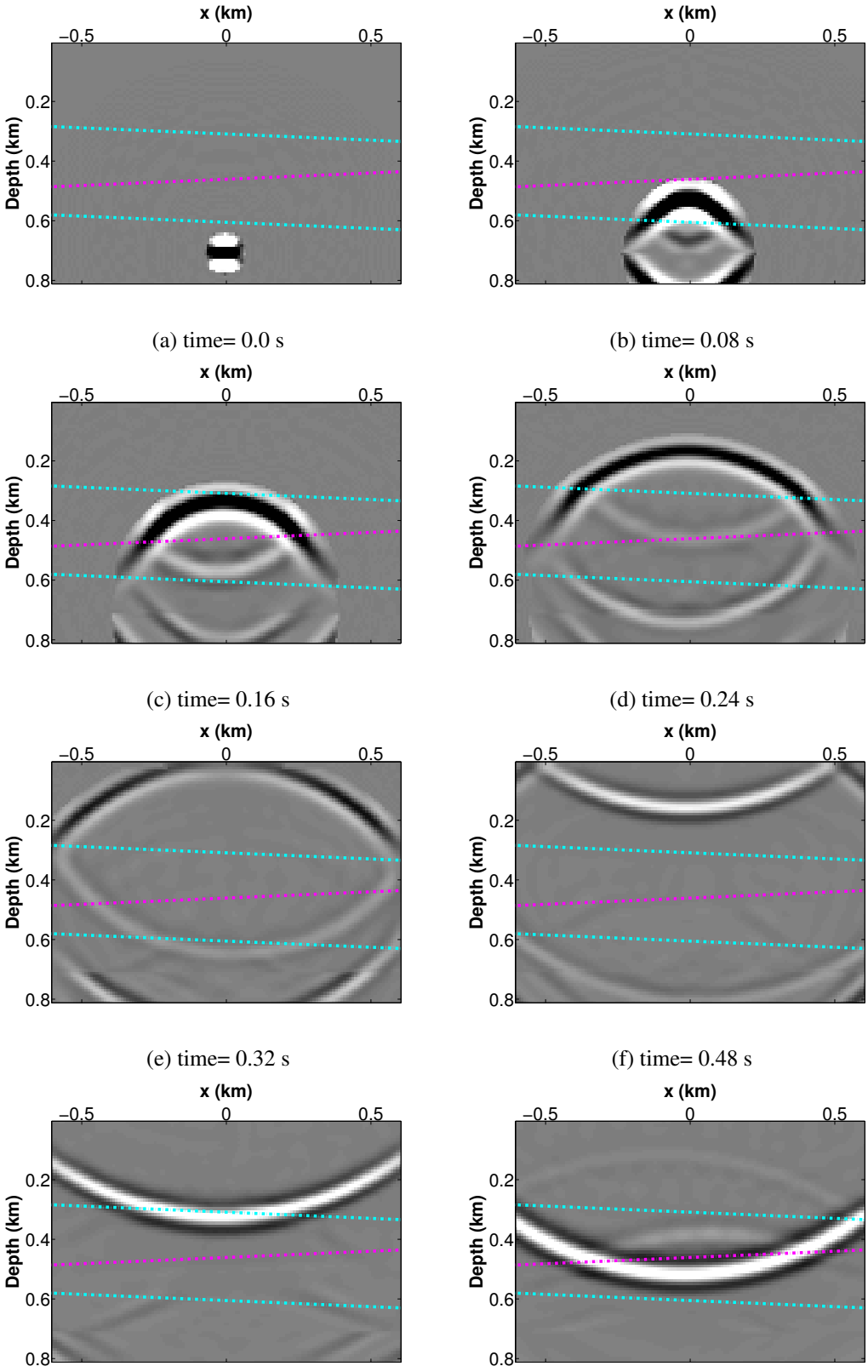

(a) time= 0.0 s

(b) time= 0.08 s

(c) time= 0.16 s

(d) time= 0.24 s

(e) time= 0.32 s

(f) time= 0.48 s

(g) time= 0.56 s

(h) time= 0.64 s

Figure 5.12: Snapshots of the virtual Green's function $G(\mathbf{x}'_i, \mathbf{x}''_j, t)$ with virtual sources $\mathbf{x}''_j = (0, 0.7)\ km$ and virtual receivers $\mathbf{x}'_i$ populating the target box in Figure 5.10.

We compare in Figure 5.13 a trace of the virtual Green's function $G(\mathbf{x}'_\mathbf{i}, \mathbf{x}''_\mathbf{j}, t)$ at virtual location $\mathbf{x}'_\mathbf{i} = (0, 0.17)\ km$ and $\mathbf{x}''_\mathbf{j} = (0, 0.7)\ km$ to the modeled Green's function with physical receiver and physical source at the virtual receiver and virtual source location $\mathbf{x}'_\mathbf{i}$ and $\mathbf{x}''_\mathbf{j}$, respectively. The modeled Green's function in Figure 5.13 is generated by finite differences using the exact velocity and density. The trace of the virtual Green's function is comparable to the modeled Green's function as shown in Figure 5.13.

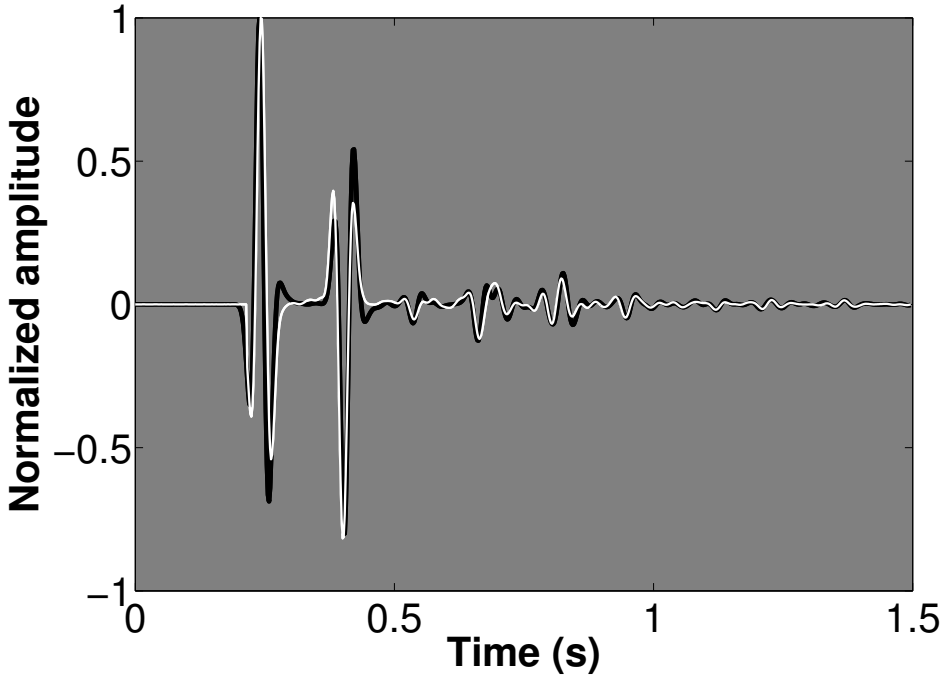

Figure 5.13: Virtual Green's function (white line) with virtual source $\mathbf{x}''_\mathbf{j} = (0, 0.7)\ km$ and recording at the virtual receiver $\mathbf{x}'_\mathbf{i} = (0, 0.17)\ km$ for the 2D model in Figure 5.10. The black thicker line is the modeled Green's function, superimposed on it is the retrieved Green's function.

In our algorithm, we evaluate an integral over space using a sampling interval dx, for example, in equations 5.3 and 5.4. These integrals over space, which yields the stationary phase contribution, also generate artifacts due to end point contributions. Similar to interferometry, these artifacts can be mitigated through tapering at the edges of the integration interval (Mehta et al., 2008; van der Neut et al., 2009). In our 2D model these artifacts that arise from the integrals over space are also present. We remove these artifacts by muting the wavefield before the first arrival of the virtual source $\mathbf{x}''_\mathbf{j}$, and estimate the travel time of the first arrival using the smooth velocity model.

5.4 Discussion

The theory of the virtual Green's function is based on Marchenko equations and uses the Marchenko solutions as well; hence, the virtual Green's function also suffers from the shortcomings and requirements of the Marchenko retrieved Green's function that are described elsewhere (Broggini and Snieder, 2012; Broggini et al., 2012; Singh et al., 2015, 2016; Slob et al., 2014; Wapenaar et al., 2013a, 2014b).

A fair question to ask is: why not use interferometry to cross-correlate the Green's function at a virtual receiver and at virtual source to get the virtual Green's function between the virtual source and the receiver? This interferometric method will not retrieve the virtual Green's function when we only have a source at the surface because interferometry requires sources on both sides of the receiver. In Figure 5.14 (red line), we show the interferometric Green's function, (cross-correlation of the Green's functions from the virtual source and receiver to the surface), for the same model (see Figure 5.7) with the same virtual source $\mathbf{x}_\mathbf{j}'' = 1.75\ km$ and virtual receiver $\mathbf{x}_\mathbf{i}' = 0.25\ km$ locations in the second 1D example.

Since we have reflectors below the virtual source location $\mathbf{x}_\mathbf{j}'' = 1.75\ km$ (see Figure 5.8) and our physical sources are at the surface, our interferometric Green's function does not match the modeled or virtual Green's function (see Figure 5.14 – white line). This mis-match is caused by ignoring contributions from reflectors below the virtual source (we violated the requirement of the closed surface interferometric integral for physical sources that create the virtual source).

For the simple 2D model, the discontinuities and dip in the velocity and density are different. However, we retrieve the two-way and one-way wavefield of the virtual Green's function without any knowledge of the density model. Figure 5.12 shows reflections from the density interface (middle interface in Figure 5.12), even though no density information was included in our algorithm. We retrieve these reflections because the density information is embedded in the reflection response recorded at the surface and the Marchenko equations are able to retrieve the density reflections from this response.

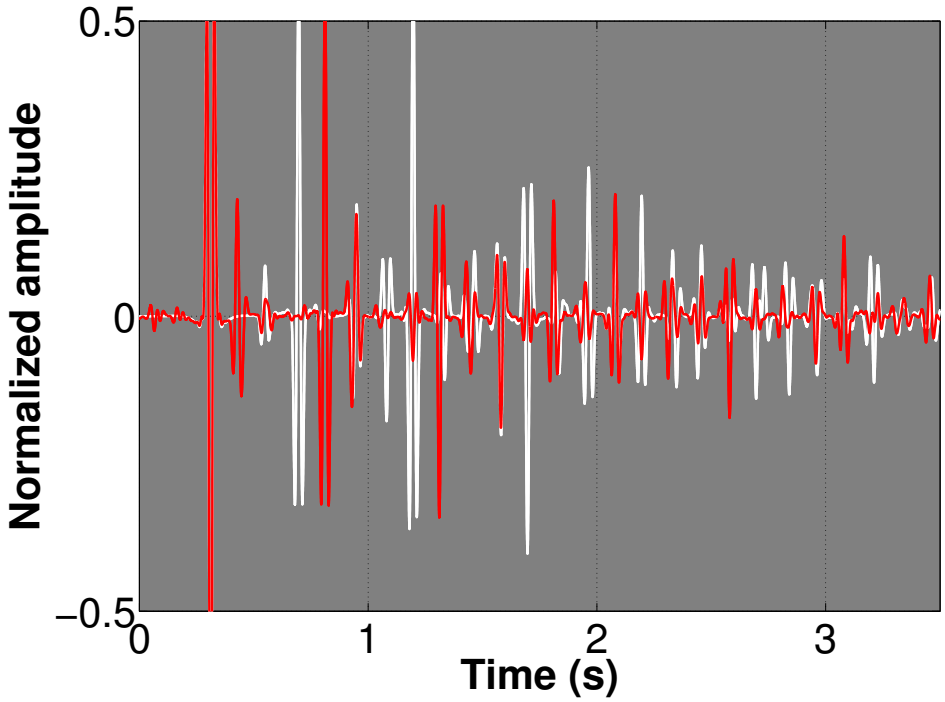

Figure 5.14: Virtual Green's function with virtual source x_j'' at depth 1.75 m and recording at the virtual receiver x_i' at depth 0.75 km retrieved by the method of this paper (white line) and computed by interferometry (red line). The retrieved virtual Green's function (white line) is almost identical to the modeled virtual Green's function.

5.5 Conclusion

We can retrieve the Green's function between two points in the subsurface with single-sided illumination. Generally, interferometry gives inaccurate Green's functions for illumination from above (single-sided) because we do not have the illumination contributions from below. However, the Marchenko equations can be thought of as the mechanism to obviate the need for illumination from below to retrieve the virtual Green's function. The removal of the requirement for illumination from below (for interferometry) comes from the use of the focusing function, a solution to the Marchenko equations. The events in the focusing function only depend on the truncated medium and this function is solved using illumination only from above. In this paper, we explore this single-side illumination advantage of the focusing function to avoid the illumination from below to retrieve the virtual Green's function.

5.6 Acknowledgments

We thank Kees Wapenaar (Delft University), Joost van Der Neut (Delft University), Ivan Vasconcelos (Schlumberger Gould Research), Esteban Diaz (CWP), and Nishant Kamath (CWP) for fruitful discussions. We are grateful to Diane Witters for her help in preparing this manuscript. This work was funded by the sponsor companies of the Consortium Project on Seismic Inverse Methods for Complex Structures and by Shell Research. The 2D reflection response in this paper is generated with the finite difference package in Thorbecke and Draganov (2011).

CHAPTER 6

SUMMARY AND FUTURE RECOMMENDATIONS

The main points in my thesis are:

1. I show how to retrieve the Green's function in the presence of the free surface; hence this Green's function includes primaries, internal, and free-surface multiples.

2. This method obviates the need to remove free-surface multiples from the reflection response as opposed to previous work which requires these multiples to be removed before retrieving the Green's functions (Broggini and Snieder, 2012; Broggini et al., 2012; Slob et al., 2014; Wapenaar et al., 2013a, 2014b).

3. I show that imaging with the Green's function using multidimensional deconvolution significantly reduces the artifacts caused by free-surface multiples compared to standard imaging algorithms.

4. I illustrate that imaging with the first arrival of the down-going Green's function and the up-going Green's function is more robust and practical compared to imaging with the down- and up-going Green's function.

5. The Green's function in Marchenko imaging is retrieved at a point on the surface to a virtual receiver in the subsurface; however, I utilize the Marchenko equations and the reciprocity theorems to retrieve the Green's function at a virtual source in the subsurface to a virtual receiver also in the subsurface, called the *virtual Green's function*.

More detailed summaries of my work are found in the conclusion section in each chapter.

6.1 Direction for future research

In this section I briefly explain possible future research ideas.

6.1.1 Future Research 1

Can one invert for velocity and density using Hooke's law and Newton's laws?

The Marchenko equations are able to retrieve the Green's function at the surface for virtual receivers in the subsurface without requiring a physical receiver to be present at the virtual receiver. Therefore, one can create the wavefield in the subsurface or at a target location, for sources on the surface, by populating the subsurface with virtual receivers. In theory, one can use these wavefields in the scalar wave equation to invert for the velocity.

In addition, density is the parameter that relates the time derivative of the particle velocity recording to the spatial derivative of the pressure recording in Newton's second law. The Marchenko Green's functions can retrieve the particle (v_z) or pressure recording p for an acoustic source, therefore can one invert for the density using these recording?

Note that the fields constructed by the Marchenko equations (v_z and p) do have the correct relative amplitudes, but the scaling factor in each of the fields are different. Therefore, a simple inversion of the Marchenko retrieved v_z and p will not yield the subsurface density. However, one can match the surface expression of the wavefields (v_z and p) to our surface reflection response to obtain the correct scaling factor, which should help us better invert for the density.

But can the Marchenko wavefields give the correct relative amplitudes in complex geology?

6.1.2 Future Research 2

Can the retrieved Green's functions be used to correctly update the smooth version of starting velocity that initializes the Marchenko scheme?

The accuracy of the retrieved Green's function is driven by the kinematic exactness of the smooth velocity model used for solving the Marchenko equations. Recent work shows that for the wrong velocity model, at the virtual receiver location, the Green's function does not focus to a band-limited delta function; however it appears to have a preferential shape (defocusing) depending on if the velocity is too high or too low. Can one use this defocusing to update the velocity model to the correct values using similar principles proposed by Symes and Carazzone (1991) and Sava

and Biondi (2004)?

6.1.3 Future Research 3

Can we include horizontal propagating energy by re-deriving the Marchenko equations with two-way wavefields instead of one-way wavefields?

The Marchenko equations are derived using one-way reciprocity theorems, which restrict the retrieval of the Green's function to propagation paths that are not horizontal or near horizontal. These one-way wavefields also require normalizations, as discussed in Chapter 3, for one-way reciprocity to be applicable. However, two-way equations exist which are equivalent to the one-way reciprocity theorems that do not require the fields to be normalized and include horizontally propagating events. These two-way equations require both the velocity and pressure fields at the receiver.

Constructing the Marchenko equations with the two-way reciprocity theorems seems like an rudimentary extension, but defining the focusing functions as two-way wavefields may not be as simple. At the focusing location for two-way wavefield, one has to define the pressure and the velocity wavefield as as a delta function and a vertical derivative of a delta function. Computing the vertical derivative of the delta function is not trivial, it seems that one should redefine the focusing functions to avoid this derivative.

Horizontally propagating waves such as evanescent waves (bounded states) are restricted to the interfaces in the subsurface and may not be recorded at the surface. Including such horizontally propagating energy will introduce non-uniqueness in the retrieval of the Green's function.

6.1.4 Future Research 4

Does multiples contribute to the subsurface image?

I have not yet analyzed the advantage of including the multiples in the Green's function for imaging. This procedure can be investigated by imaging target areas of models which are blind to primaries but not multiples. Intuitively, multiples in the retrieved Green's function should not contribute to the parts of the model that are blind to the primaries in the Green's function, as only

the primary reflections are necessary to create the stationary phase contribution of the retrieved Green's function (van der Neut et al., 2015). Conversely, in standard imaging multiples provide redundant as well as new information that is still useful to improve our image. Using multiples can increase the illumination and lead to better vertical resolution in the image (Jiang et al., 2007; Muijs et al., 2007a,b; Schuster et al., 2003). How does the Marchenko equation exactly handle the multiples? may help in answering if the multiples do contribute in Marchenko imaging.

6.1.5 Future Research 5

Can the Marchenko equations account for elastic waves in the presence of the free-surface?

The retrieval of the Green's function and hence the Marchenko imaging is currently an acoustic technique; work has already begun on making the procedure, for data without free-surface multiples, elastodynamic (da Costa Filho et al., 2014; Wapenaar and Slob, 2014). To account for the free-surface multiples in the elastic Marchenko equations one can follow a similar procedure as discussed in Chapter 2 and 3. The causality assumptions are more complex in the elastic case compared to the acoustic case, therefore solving the elastic Marchenko equations are more involved and including the free-surface multiples may cause more instabilities.

6.1.6 Future Research 6

Can one include the ghost reflections in the Green's function?

The Marchenko equations require the surface reflection response to retrieve the Green's function. The sources and receivers must be on the acquisition surface, i.e. at the free surface, to record this reflection response. The scheme to derive the Marchenko equations requires up- and down-going fields at the acquisition datum; given that the up- and down-going fields at the datum can be obtained. Computation of the up and down-going fields at an arbitrary acquisition surface is extensively discussed in the literature (Bale, 1998; Barr and Sanders, 1989; Osen and Reitan, 1999; Soubaras, 1996).

Placing this datum at the free-surface means that, at the free surface, all up-going waves are equal to the down-going waves scaled by the reflection coefficient at the free surface. Moving

the datum away from the free-surface includes the ghost reflections and makes the Marchenko equation difficult to solve with our conventional approach. My preliminary derivations suggests that I must know the direct ghost arrivals to include the ghosts in the retrieved Green's functions.

REFERENCES CITED

Amundsen, L., 2001, Elimination of free-surface related multiples without need of the source wavelet: Geophysics, **66**, 327–341.

Bakulin, A., and R. Calvert, 2006, The virtual source method: Theory and case study: Geophysics, **71(4)**, SI139–SI150.

Bale, R. A., 1998, Plane wave deghosting of hydrophone and geophone OBC data: 68th Annual Meeting, SEG, Expanded Abstract, 730–733.

Barr, F. J., and J. I. Sanders, 1989, Attenuation of watercolumn reverberations using pressure and velocity detectors in a waterbottom cable: 59th Annual SEG Meeting, Expanded Abstracts, 653–655.

Baysal, E., D. D. Kosloff, and J. W. Sherwood, 1983, Reverse time migration: Geophysics, **48**, 1514–1524.

Behura, J., K. Wapenaar, and R. Snieder, 2012, Newton-Marchenko-Rose imaging, *in* SEG Technical Program Expanded Abstracts 2012: Society of Exploration Geophysicists, 1–6.

Berkhout, A., and D. Verschuur, 1997, Estimation of multiple scattering by iterative inversion, part I: Theoretical considerations: Geophysics, **62**, 1586–1595.

———, 2006, Imaging of multiple reflections: Geophysics, **71(6)**, SI209–SI220.

Broggini, F., and R. Snieder, 2012, Connection of scattering principles: a visual and mathematical tour: European Journal of Physics, **33**, 593–613.

Broggini, F., R. Snieder, and K. Wapenaar, 2011, Connection of scattering principles: Focusing the wavefield without source or receiver, *in* SEG Technical Program Expanded Abstracts 2011: Society of Exploration Geophysicists, 3845–3850.

———, 2012, Focusing the wavefield inside an unknown 1D medium: Beyond seismic interferometry: Geophysics, **77(5)**, A25–A28.

Broggini, F., R. Snieder, K. Wapenaar, and J. Behura, 2014, Wavefield autofocusing and imaging with multidimensional deconvolution: Numerical examples for reflection data with internal multiples: Geophysics, **72(3)**, WA107–WA115.

Burridge, R., 1980, The Gelfand-Levitan, the Marchenko, and the Gopinath-Sondhi integral equations of inverse scattering theory, regarded in the context of inverse impulse-response problems: Wave Motion, **2**, 305–323.

Chadan, K., and P. C. Sabatier, 2012, Inverse problems in quantum scattering theory: Springer Science & Business Media.

Challis, L., and F. Sheard, 2003, The Green of Green functions: Phys. Today, **56**, 41–46.

Chavent, G., and C. A. Jacewitz, 1995, Determination of background velocities by multiple migration fitting: Geophysics, **60**, 476–490.

Claerbout, J., 1971, Toward a unified theory of reflector mapping: Geophysics, **36**, 467–481.

———, 1985, Imaging the Earth's interior: Blackwell scientific publications.

Clayton, R., and R. Wiggins, 1976, Source shape estimation and deconvolution of teleseismic body waves: Geophys. J.R. Astr. Soc., **47**, 151–177.

Curtis, A., P. Gerstoft, H. Sato, R. Snieder, and K. Wapenaar, 2006, Seismic interferometry -turning noise into signal: The Leading Edge, **25**, 1082–1092.

Curtis, A., and D. Halliday, 2010, Source-receiver wave field interferometry: Physical Review E, **81**, 046601.

Curtis, A., H. Nicolson, D. Halliday, J. Trampert, and B. Baptie, 2009, Virtual seismometers in the subsurface of the earth from seismic interferometry: Nature Geoscience, **2**, 700–704.

da Costa Filho, C. A., M. Ravasi, A. Curtis, and G. A. Meles, 2014, Elastodynamic Green's function retrieval through single-sided Marchenko inverse scattering: Phys. Rev. E, **90**, no. 6, 063201.

Glogovsky, V., E. Landa, and J. Paffenholz, 2002, Integrated approach to subsalt depth imaging: Synthetic case study: The Leading Edge, **21**, 1217–1223.

Goupillaud, P. L., 1961, An approach to inverse filtering of near-surface layer effects from seismic records: Geophysics, **26**, 754–760.

Guitton, A., et al., 2002, Shot-profile migration of multiple reflections: SEG Technical Program Expanded Abstracts, 1296–1299.

Jiang, Z., J. Sheng, J. Yu, G. Schuster, and B. Hornby, 2007, Migration methods for imaging different-order multiples: Geophysical Prospecting, **55**, 1–19.

Lamb Jr, G. L., 1980, Elements of soliton theory: New York, Wiley-Interscience, 1980.

Lokshtanov, D., 1999, Multiple suppression by data-consistent deconvolution: The Leading Edge, **18**, 115–119.

Malcolm, A., B. Ursin, and V. Maarten, 2009, Seismic imaging and illumination with internal multiples: Geophysical Journal International, **176**, 847–864.

Marchenko, V. A., 1955, On reconstruction of the potential energy from phases of the scattered waves: Dokl. Akad. Nauk SSSR, 695–698.

McMechan, G. A., 1989, A review of seismic acoustic imaging by reverse-time migration: International Journal of Imaging Systems and Technology, **1**, 18–21.

Mehta, K., A. Bakulin, J. Sheiman, R. Calvert, and R. Snieder, 2007, Improving the virtual source method by wavefield separation: Geophysics, **72**, V79–V86.

Mehta, K., R. Snieder, R. Calvert, and J. Sheiman, 2008, Acquisition geometry requirements for generating virtual-source data: The Leading Edge, **27**, 620–629.

Morse, P. M., and H. Feshbach, 1953, Methods of theoretical physics: McGraw-Hill Book Co., Inc, **Parts I and II**.

Muijs, R., J. O. A. Robertsson, and K. Holliger, 2007a, Prestack depth migration of primary and surface-related multiple reflections: Part I: Imaging: Geophysics, **72(2)**, S59–S69.

———, 2007b, Prestack depth migration of primary and surface-related multiple reflections: Part II: Identification and removal of residual multiples: Geophysics, **72(2)**, S71–S76.

Noble, M., J. Lindgren, A. Tarantola, et al., 1991, Large-sized nonlinear inversion of a marine data set: Retrieving the source, the background velocity and the impedance contrasts: 61st SEG meeting, Houston, USA, Expanded Abstracts, 893–896.

O'Brien, M. J., and S. H. Gray, 1996, Can we image beneath salt?: The Leading Edge, **15**, 17–22.

Ong, C., C. Lapilli, J. Perdomo, and R. Coates, 2002, Extended imaging and illumination in wave migrations: SEG Technical Program Expanded Abstracts, 4116–4120.

Osen, A., L. A., and A. Reitan, 1999, Removal of waterlayer multiples from multicomponent seabottom data: Geophysics, **64**, 838–851.

Ramírez, A., A. Weglein, et al., 2005, An inverse scattering internal multiple elimination method: Beyond attenuation, a new algorithm and initial tests: SEG Expanded Abstracts, 2115–2118.

Reiter, E., M. Toksöz, T. Keho, and G. Purdy, 1991, Imaging with deep-water multiples: Geophysics, **56**, 1081–1086.

Rose, J., 2002a, Single-sided autofocusing of sound in layered materials: Inverse problems, **18**, 1923–1934.

———, 2002b, Time reversal, focusing and exact inverse scattering, *in* Imaging of complex media with acoustic and seismic waves: Springer, 97–106.

Sava, P., and B. Biondi, 2004, Wave-equation migration velocity analysis. I. theory: Geophysical Prospecting, **52**.

Schleicher, J., J. Costa, and A. Novais, 2007, A comparison of imaging conditions for wave-equation shot-profile migration: 2393–2397.

Schneider, W., 1978, Integral formulation for migration in two and three dimensions: Geophysics, **43**, 49–76.

Schuster, G. T., Z. Jiang, and J. Yu, 2003, Imaging the most bounce out of multiples: Presented at the 65th Annual Conference, EAGE Expanded Abstracts: session on Multiple Elimination.

Singh, S., R. Snieder, J. Behura, J. van der Neut, K. Wapenaar, and E. Slob, 2015, Marchenko imaging: Imaging with primaries, internal multiples, and free-surface multiples: Geophysics, **80**, S165–S174.

Singh, S., R. Snieder, J. Thorbecke, J. van der Neut, K. Wapenaar, and E. Slob, 2016, Incoporating free surface multiples in Marchenko imaging: Geophysics, submitted.

Slob, E., K. Wapenaar, F. Broggini, and R. Snieder, 2014, Seismic reflector imaging using internal multiples with Marchenko-type equations: Geophysics, **79(2)**, S63–S76.

Snieder, R., 1990a, A perturbative analysis of nonlinear inversion: Geophys. J. Int., **101**, 545–556.

———, 1990b, The role of the Born-approximation in nonlinear inversion: Inverse Problems, **6**, 247–266.

———, 2004, Extracting the Green's function from the correlation of coda waves: A derivation based on stationary phase: Physical Review E, **69**, 046610.

Snieder, R., K. Wapenaar, and K. Larner, 2006, Spurious multiples in seismic interferometry of primaries: Geophysics, **71**, SI111–SI124.

Snieder, R., K. Wapenaar, and U. Wegler, 2007, Unified Green's function retrieval by cross-correlation; connection with energy principles: Physical Review E, **75**, 036103.

Soubaras, R., 1996, Ocean bottom hydrophone and geophone processing: 66th Annual Meeting, SEG, Expanded Abstract, 24–27.

Symes, W. W., and J. J. Carazzone, 1991, Velocity inversion by differential semblance optimization: Geophysics, **56**, 654–663.

Thorbecke, J. W., and D. Draganov, 2011, Finite-difference modeling experiments for seismic interferometry: Geophysics, **76**, H1–H18.

Ursin, B., 1983, Review of elastic and electromagnetic wave propagation in horizontally layered media: Geophysics, **48**, 1063–1081.

van der Neut, J., J. Thorbecke, et al., 2009, Resolution function for controlled-source seismic interferometry: a data-driven diagnosis: SEG Technical Program Expanded Abstracts 2009, 4090–4094.

van der Neut, J., J. Thorbecke, K. Mehta, E. Slob, and K. Wapenaar, 2011, Controlled-source interferometric redatuming by crosscorrelation and multidimensional deconvolution in elastic media: Geophysics, **76(4)**, SA63–SA76.

van der Neut, J., I. Vasconcelos, and K. Wapenaar, 2015, On Green's function retrieval by iterative substitution of the coupled Marchenko equations: Geophysical Journal International, **203**, 792–813.

van Groenestijn, G., and D. Verschuur, 2009, Estimating primaries by sparse inversion and application to near-offset data reconstruction: Geophysics, **74(3)**, A23–A28.

van Manen, D.-J., A. Curtis, and J. O. Robertsson, 2006, Interferometric modeling of wave propagation in inhomogeneous elastic media using time reversal and reciprocity: Geophysics, **71**, SI47–SI60.

Verschuur, D., and A. Berkhout, 2005, Removal of internal multiples with the common-focus-point (CFP) approach: Part 2 Application strategies and data examples: Geophysics, **70(3)**, V61–V72.

Verschuur, D., A. Berkhout, and C. Wapenaar, 1992, Adaptive surface-related multiple elimination: Geophysics, **57**, 1166–1177.

Wapenaar, C., M. Dillen, and J. Fokkema, 2001, Reciprocity theorems for electromagnetic or acoustic one-way wave fields in dissipative inhomogeneous media: Radio Science, **36**, 851–863.

Wapenaar, C., G. Peels, V. Budejicky, and A. Berkhout, 1989, Inverse extrapolation of primary seismic waves: Geophysics, **54**, 853–863.

Wapenaar, C. P. A., and J. L. T. Grimbergen, 1996, Reciprocity theorems for one-way wavefields: Geophysical Journal International, **127**, 169–177.

Wapenaar, K., 1998, Reciprocity properties of one-way propagators: Geophysics, **63**, 1795.

———, 2004, Retrieving the elastodynamic Green's function of an arbitrary inhomogeneous medium by cross correlation: Physical Review Letters, **93**, 254301.

Wapenaar, K., F. Broggini, E. Slob, and R. Snieder, 2013a, Three-dimensional single-sided Marchenko inverse scattering, data-driven focusing, Green's function retrieval, and their mutual relations: Physical Review Letters, **110**, no. 8, 084301.

Wapenaar, K., F. Broggini, and R. Snieder, 2012, Creating a virtual source inside a medium from reflection data: heuristic derivation and stationary-phase analysis: Geophysical Journal International, **190**.

Wapenaar, K., F. Broggini, R. Snieder, et al., 2011, A proposal for model-independent 3D wave field reconstruction from reflection data: 2011 SEG Annual Meeting, Society of Exploration Geophysicists, 3788–3792.

Wapenaar, K., and J. Fokkema, 2006, Greens function representations for seismic interferometry: Geophysics, **71(4)**, SI33–SI46.

Wapenaar, K., J. Fokkema, M. Dillen, P. Scherpenhuijsen, et al., 2000, One-way acoustic reciprocity and its applications in multiple elimination and time-lapse seismics: SEG Technical Program Expanded Abstracts 2000, Society of Exploration Geophysicists, 2377–2380.

Wapenaar, K., and E. Slob, 2014, On the Marchenko equation for multicomponent single-sided reflection data: Geophysical Journal International, **199**, 1367–1371.

Wapenaar, K., E. Slob, and R. Snieder, 2008a, Seismic and electromagnetic controlled-source interferometry in dissipative media: Geophysical Prospecting, **56**, 419–434.

———, 2008b, Seismic and electromagnetic controlled-source interferometry in dissipative media: Geophys. Prosp., **56**, 419–434.

Wapenaar, K., E. Slob, J. van der Neut, J. Thorbecke, F. Broggini, and R. Snieder, 2013b, Three-dimensional Marchenko equation for Green's function retrieval beyond seismic interferometry: 83rd Annual International meeting of the SEG, 4573–4578.

Wapenaar, K., J. Thorbecke, and D. Draganov, 2004a, Relations between reflection and transmission responses of three-dimensional inhomogeneous media: Geophysical Journal International, **156**, 179–194.

———, 2004b, Relations between reflection and transmission responses of three-dimensional inhomogeneous media: Geophysical Journal International, **156**, 179–194.

Wapenaar, K., J. Thorbecke, and J. van der Neut, 2016, A single-sided homogeneous Green's function representation for holographic imaging, inverse scattering, time-reversal acoustics and interferometric Green's function retrieval: Geophysical Journal International, **205**, 531–535.

Wapenaar, K., J. Thorbecke, J. van der Neut, F. Broggini, E. Slob, and R. Snieder, 2014a, Green's function retrieval from reflection data, in absence of a receiver at the virtual source position: Journal of the Acoustical Society of America, **135**, 2847–2861.

———, 2014b, Marchenko imaging: Geophysics, **79**, WA39–WA57.

Weglein, A., F. Araújo, P. Carvalho, R. Stolt, K. Matson, R. Coates, D. Corrigan, D. Foster, S. Shaw, and H. Zhang, 2003, Inverse scattering series and seismic exploration: Inverse problems, **19**, R27–R83.

Weglein, A., and W. Dragoset, 2007, Multiple attenuation: Society of Exploration Geophysicists, **23**, 482.

Weglein, A., F. Gasparotto, P. Carvalho, and R. Stolt, 1997, An inverse-scattering series method for attenuating multiples in seismic reflection data: Geophysics, **62**, 1975–1989.

Whitmore, N. D., 1983, Iterative depth migration by backward time propagation: SEG Technical Program Expanded Abstracts, 382–385.

Wiggins, J., 1988, Attenuation of complex water-bottom multiples by wave-equation-based prediction and subtraction: Geophysics, **53**, 1527–1539.

Wiggins, J. W., 1984, Kirchhoff integral extrapolation and migration of nonplanar data: Geophysics, **49**, 1239–1248.

Ypma, F., and D. Verschuur, 2013, Estimating primaries by sparse inversion, a generalized approach: Geophysical Prospecting, **61**, 94–108.

Ziolkowski, A., D. Taylor, and R. Johnston, 1999, Marine seismic wavefield measurement to remove sea-surface multiples: Geophysical Prospecting, **47**, 841–870.

APPENDIX A - GREEN'S FUNCTION RETRIEVAL IN THE PRESENCE OF THE FREE SURFACE

We discuss our adaptation of the method of Wapenaar et al. (2013b) to account for the free-surface reflections. The focusing functions are the wavefields that focus, in both time and space, at a point in the medium or at the surface (Figure 2.2(a) and Figure 2.2(b)). These focusing functions exist in the reference medium, which is homogeneous above the depth level ∂D_0 and reflection-free below ∂D_i.

The reciprocity theorems for one-way (up-going and down-going) wavefields are derived by Wapenaar and Grimbergen (1996), see equations A.3 and A.4. We use the convolution-type and correlation-type reciprocity theorems to find relationships between our up- and down-going wavefields. As discussed by Wapenaar et al. (2014a), we obtain a relationship between the focusing functions (f_1 and f_2) by using their respective up- and down-going waves at each depth level (∂D_0 and ∂D_i) with the convolution reciprocity theorem

$$f_1^+(\mathbf{x_0''}, \mathbf{x_i'}, \omega) = f_2^-(\mathbf{x_i'}, \mathbf{x_0''}, \omega) \tag{A.1}$$

and correlation reciprocity theorem

$$-f_1^-(\mathbf{x_0''}, \mathbf{x_i'}, \omega)^* = f_2^+(\mathbf{x_i'}, \mathbf{x_0''}, \omega). \tag{A.2}$$

Our actual inhomogeneous model with a free surface above ∂D_0 is shown in Figure 2.3. As opposed to the model in Wapenaar et al. (2013a), which does not have a free surface, we consider the reflections from the free surface for a down-going source similar to the work of Wapenaar et al. (2004a). In Figure 2.3, we describe the wavefield in its up- and down-going components. The downward propagating component of the wavefield (Green's function) at ∂D_0 is $G^+(\mathbf{x_0}, \mathbf{x_0''}, \omega) = \delta(\mathbf{x_H} - \mathbf{x_H''}) + rR(\mathbf{x_0}, \mathbf{x_0''}, \omega)$, which includes (in the right hand side) the downward-going impulsive source and the reflection from the free surface. The down-going source $\delta(\mathbf{x_H} - \mathbf{x_H''})$ is a 2-dimensional Dirac delta where $\mathbf{x_H''}$ is the lateral position of the focal point of f_2.

Note G^+ is the component of the Green's function that is propagating downwards at $\mathbf{x_0}$ for a downward radiating source at $\mathbf{x_0''}$. In the case without the free surface, there are no reflections from the free surface, hence $G_0^+(\mathbf{x_0}, \mathbf{x_0''}, \omega) = \delta(\mathbf{x_H} - \mathbf{x_H''})$ because $r = 0$. The upward-going propagating part of the Green's function G^- at ∂D_0 is the reflection response $R(\mathbf{x_0}, \mathbf{x_0''}, \omega)$. We consider the up- and down-going components of the Green's function at ∂D_i. The down-going component is $G^+(\mathbf{x_i}, \mathbf{x_0''}, \omega)$ while the up-going component is $G^-(\mathbf{x_i}, \mathbf{x_0''}, \omega)$ (G^+ and G^- respectively, Figure 2.3). We use the convolution and correlation reciprocity theorems to find relationships for the one-way wavefields of f_1 shown in Figure 2.2(a) and the one-way wavefields of the Green's function in the actual medium shown in Figure 2.3:

$$G^-(\mathbf{x_i'}, \mathbf{x_0''}, \omega) = \int_{\partial D_0} [f_1^+(\mathbf{x_0}, \mathbf{x_i'}, \omega) R(\mathbf{x_0}, \mathbf{x_0''}, \omega) - r f_1^-(\mathbf{x_0}, \mathbf{x_i'}, \omega) R(\mathbf{x_0}, \mathbf{x_0''}, \omega)] d\mathbf{x} - f_1^-(\mathbf{x_0''}, \mathbf{x_i'}, \omega), \tag{A.3}$$

and

$$G^+(\mathbf{x_i'}, \mathbf{x_0''}, \omega) = - \int_{\partial D_0} [f_1^-(\mathbf{x_0}, \mathbf{x_i'}, \omega)^* R(\mathbf{x_0}, \mathbf{x_0''}, \omega) - r f_1^+(\mathbf{x_0}, \mathbf{x_i'}, \omega)^* R(\mathbf{x_0}, \mathbf{x_0''}, \omega)] d\mathbf{x} + f_1^+(\mathbf{x_0''}, \mathbf{x_i'}, \omega)^*. \tag{A.4}$$

Equations A.3 and A.4 are similar to the relation for the up- and down-going Green's function in Wapenaar et al. (2014a), however equations A.3 and A.4 also accounts for the reflected waves from the free surface. These free-surface reflections are the expressions in equations A.3 and A.4 that are multiplied by r. The two-way Green's function is obtained by adding equations A.3 and A.4 as well as using equations 2.2, 2.3, A.1, and A.2:

$$G(\mathbf{x_i'}, \mathbf{x_0''}, \omega) = f_2(\mathbf{x_i'}, \mathbf{x_0''}, \omega)^* + \int_{\partial D_0} f_2(\mathbf{x_i'}, \mathbf{x_0}, \omega) R(\mathbf{x_0}, \mathbf{x_0''}, \omega) d\mathbf{x_0} + r \int_{\partial D_0} f_2(\mathbf{x_i'}, \mathbf{x_0}, \omega)^* R(\mathbf{x_0}, \mathbf{x_0''}, \omega) d\mathbf{x_0}. \tag{A.5}$$

We consider equation A.5, in time, for the interval $t < t_d(\mathbf{x_i'}, \mathbf{x_0''})$, where t_d is the travel time for the first arrival of G. No waves arrive before $t_d(\mathbf{x_i'}, \mathbf{x_0''})$ since t_d is the time for the first arriving

event. Therefore, $G(\mathbf{x_i}^{'}, \mathbf{x_0}^{''}, \omega)$ vanishes for $t < t_d(\mathbf{x_i}^{'}, \mathbf{x_0}^{''})$ and as a result

$$0 = f_2(\mathbf{x_i}^{'}, \mathbf{x_0}^{''}, -t) + \int_{\partial D_0} d\mathbf{x_0} \int_{-\infty}^{t} f_2(\mathbf{x_i}^{'}, \mathbf{x_0}, t^{'}) R(\mathbf{x_0}, \mathbf{x_0}^{''}, t - t^{'}) dt^{'} + r \int_{\partial D_0} d\mathbf{x_0} \int_{-t}^{\infty} f_2(\mathbf{x_i}^{'}, \mathbf{x_0}, t^{'}) R(\mathbf{x_0}, \mathbf{x_0}^{''}, t + t^{'}) dt^{'}. \tag{A.6}$$

We use the same ansatz for f_2 as Wapenaar et al. (2013a) because we are using the same reference medium, i.e. the model where the focusing functions exist. The ansatz is given by

$$f_2(\mathbf{x_i}, \mathbf{x_0}^{''}, t) = [T_d(\mathbf{x_i}, \mathbf{x_0}^{''}, t)]^{inv} + M(\mathbf{x_i}, \mathbf{x_0}^{''}, t), \tag{A.7}$$

where $[T_d(\mathbf{x_i}, \mathbf{x_0}^{''}, t)]^{inv}$, defined as the inverse of the direct arrival of the transmission response, is the first arriving event of $f_2(\mathbf{x_i}, \mathbf{x_0}^{''}, t)$ and $M(\mathbf{x_i}, \mathbf{x_0}^{''}, t)$ is the scattering coda of f_2 following the first arrival as shown by Wapenaar et al. (2013a). The substitution of expression A.7 in equation A.6 yields

$$\begin{aligned} 0 = M(\mathbf{x_i}', \mathbf{x_0}^{''}, -t) + & \int_{\partial D_0} d\mathbf{x_0} \int_{-\infty}^{-t_d^{\epsilon}(\mathbf{x_i}', \mathbf{x_0})} [T_d(\mathbf{x_i}', \mathbf{x_0}, t')]^{inv} R(\mathbf{x_0}, \mathbf{x_0}^{''}, t - t^{'}) dt^{'} \\ + & \int_{\partial D_0} d\mathbf{x_0} \int_{-t_d^{\epsilon}(\mathbf{x_i}', \mathbf{x_0})}^{t} M(\mathbf{x_i}', \mathbf{x_0}, t') R(\mathbf{x_0}, \mathbf{x_0}^{''}, t - t^{'}) dt^{'} \\ & + r \int_{\partial D_0} d\mathbf{x_0} \int_{-t_d^{\epsilon}(\mathbf{x_i}', \mathbf{x_0})}^{\infty} M(\mathbf{x_i}', \mathbf{x_0}, t') R(\mathbf{x_0}, \mathbf{x_0}^{''}, t + t^{'}) dt^{'} \\ & + r \int_{\partial D_0} d\mathbf{x_0} \int_{-t}^{-t_d^{\epsilon}(\mathbf{x_i}', \mathbf{x_0})} [T_d(\mathbf{x_i}', \mathbf{x_0}, t')]^{inv} R(\mathbf{x_0}, \mathbf{x_0}^{''}, t + t^{'}) dt^{'}, \end{aligned} \tag{A.8}$$

for $t < t_d(\mathbf{x_i}^{'}, \mathbf{x_0}^{''})$ with $t_d^{\epsilon}(\mathbf{x_i}', \mathbf{x_0}^{''})$= $t_d(\mathbf{x_i}', \mathbf{x_0}^{''}) - \epsilon$ where ϵ is a small positive constant to include the direct arrival in the integral. Equation A.8 is a Fredholm integral of the second kind and can be solved iteratively as follows:

$$\begin{aligned} M_k(\mathbf{x_i}', \mathbf{x_0}^{''}, -t) = M_0(\mathbf{x_i}', \mathbf{x_0}^{''}, -t) - & \int_{\partial D_0} d\mathbf{x_0} \int_{-t_d^{\epsilon}(\mathbf{x_i}', \mathbf{x_0})}^{\infty} M_{k-1}(\mathbf{x_i}', \mathbf{x_0}, t') R(\mathbf{x_0}, \mathbf{x_0}^{''}, t - t^{'}) dt^{'} \\ & - r \int_{\partial D_0} d\mathbf{x_0} \int_{-t_d^{\epsilon}(\mathbf{x_i}', \mathbf{x_0})}^{\infty} M_{k-1}(\mathbf{x_i}', \mathbf{x_0}, t') R(\mathbf{x_0}, \mathbf{x_0}^{''}, t + t^{'}) dt^{'}, \end{aligned} \tag{A.9}$$

where

$$M_0(\mathbf{x}_\mathbf{i}', \mathbf{x}_\mathbf{0}'', -t) = -\int_{\partial D_0} d\mathbf{x_0} \int_{-\infty}^{-t_d^\epsilon(\mathbf{x}_\mathbf{i}', \mathbf{x_0})} [T_d(\mathbf{x}_\mathbf{i}', \mathbf{x_0}, t')]^{inv} R(\mathbf{x_0}, \mathbf{x}_\mathbf{0}^{''}, t - t^{'}) dt^{'}$$
$$- r \int_{\partial D_0} d\mathbf{x_0} \int_{-t}^{-t_d^\epsilon(\mathbf{x}_\mathbf{i}', \mathbf{x_0})} [T_d(\mathbf{x}_\mathbf{i}', \mathbf{x_0}, t')]^{inv} R(\mathbf{x_0}, \mathbf{x}_\mathbf{0}^{''}, t + t^{'}) dt^{'}, \qquad \text{(A.10)}$$

for $t < t_d(\mathbf{x}_\mathbf{i}^{'}, \mathbf{x}_\mathbf{0}^{''})$ and $M_k(\mathbf{x}_\mathbf{i}', \mathbf{x}_\mathbf{0}'', -t) = 0$ for $t \geq t_d(\mathbf{x}_\mathbf{i}^{'}, \mathbf{x}_\mathbf{0}^{''})$. In contrast to the algorithm of Wapenaar et al. (2013a), we use R instead of R_0 and we also include the reflection from the free surface (last term in equation A.9). After convergence, we substitute the coda M into equation A.7 to yield the focusing function f_2. The f_2 solution is then used in equation A.5 to obtain the two-way Green's function.

APPENDIX B - RETRIEVING THE GREEN'S FUNCTIONS ANALYTICALLY USING THE MARCHENKO EQUATIONS

For a three-interface model (two layers) in Figure 4.1,

1. The first interface is just below the acquisition surface with reflection and transmission coefficients r_0 and τ_0.

2. Similarly, r_1, τ_1, r_2, and τ_2 are the reflection and transmission coefficients of the second and third interfaces, respectively.

3. The one-way travel time of the first layer (between first and second interface) is t_1.

4. The one-way travel time of the second layer is t_2.

The reflection response for the three-interface model (two layers) for sources and receivers on the surface in Figure 4.1, in the frequency domain, is (Goupillaud, 1961)

$$R(z_0,\omega) = \frac{r_0 + r_1 e^{-2i\omega t_1} + r_2 e^{-2i\omega(t_1+t_2)} + r_0 r_1 r_2 e^{-2i\omega t_2}}{1 + r_0 r_1 e^{-2i\omega t_1} + r_0 r_2 e^{-2i\omega(t_1+t_2)} + r_1 r_2 e^{-2i\omega t_2}}, \tag{B.1}$$

where r_0, r_1, and r_2 are the reflection coefficients of the layers in order of increasing depth, respectively; t_1 and t_2 are the one way travel of the first and second layers, respectively.

We use the reflection response of this three-interface model to compute the Green's functions at two locations in the model: 1) in the middle of the first layer ($z = z_a$) and 2) just above the second interface ($z = z_1$), in Figure 4.1.

We retrieve these Green's function by solving the Marchenko equations (Broggini and Snieder, 2012; Broggini et al., 2012; Singh et al., 2015, 2016; Slob et al., 2014; Wapenaar et al., 2013a, 2014b).

Given we know the model, we can compute the focusing functions $f_1^{\pm}$ (Slob et al., 2014) as follows:

$$f_1^{+}(z_i, z_0, \omega) = \frac{1}{T^{+}(z_i, z_0, \omega)}, \tag{B.2}$$

$$f_1^-(z_i, z_0, \omega) = \frac{R(z_0, z_0, \omega)}{T^+(z_i, z_0, \omega)}, \tag{B.3}$$

where z_0 and z_1 are the depths of the first and second reflector, $R(z_0, z_0, \omega)$ is the reflection response at the surface for a source at z_0, and $T^+(z_i, z_0, \omega)$ is the transmission response at z_i for a source at z_0.

The Marchenko equations relating the Green's functions $G^{\pm}$ to the focusing functions $f_1^{\pm}$ are

$$G^-(z_i, z_0, \omega) = \ f_1^+(z_0, z_i, \omega)R(z_0, z_0, \omega) - f_1^-(z_0, z_i, \omega), \tag{B.4}$$

and

$$G^+(z_i, z_0, \omega) = -f_1^-(z_0, z_i, \omega)^* R(z_0, z_0, \omega) + f_1^+(z_0, z_i, \omega)^*, \tag{B.5}$$

where $G^{\pm}(z_i, z_0, \omega)$ are the one-way Green's functions at z_i for a source at z_0 (Broggini and Snieder, 2012; Broggini et al., 2012; Singh et al., 2015, 2016; Slob et al., 2014; Wapenaar et al., 2013a, 2014b). The one-way Green's functions are decomposed at the observation point z denoted by the first superscript $+$ or $-$. We consider downwards to be positive; hence the superscript $+$ represents down-going waves and $-$ up-going waves.

The focusing functions are auxiliary wavefields that reside in a truncated medium that 1) has the same material properties as the actual inhomogeneous medium between z_0 and z_i (arbitrary depth level) and 2) is homogeneous above z_0 and reflection-free below z_i (Slob et al., 2014). Therefore the boundary conditions on z_0 and z_i in the truncated medium, where the focusing function exists, are reflection-free.

B.1 Green's function retrieval in the middle of the first layer z_a

The focusing function exist in a truncated medium which we label Υ_a. At z_a, we define the truncated medium Υ_a as homogeneous at and below z_a and the same as the actual model above z_a. Therefore for this truncated medium Υ_a, the reflection response $R(z_0, z_0, \omega)$ in the frequency domain is r_0 while the transmission response $T(z = z_a, z_0, \omega) = \tau_0 e^{i\omega t_1/2}$.

Substituting the reflection and the transmission response for the truncated medium Υ_a into equations B.2 and B.3 yields

$$f_1^-(z_a, z_0, \omega) = \frac{1}{\tau_0} e^{i\omega t_1/2}, \tag{B.6}$$

$$f_1^+(z_a, z_0, \omega) = \frac{r_0}{\tau_0} e^{i\omega t_1/2}. \tag{B.7}$$

We retrieve the up- and down-going Green's function $G^{\pm}(z_a, z_0, \omega)$ by substituting equations B.6, B.7, and B.1 into equations B.4 and B.5:

$$G^-(z_a, z_0, \omega) = \tau_0 \frac{r_1 e^{-\frac{3}{2}i\omega t_1} + r_2 e^{-i\omega(\frac{3}{2}t_1 + 2t_2)}}{1 + r_0 r_1 e^{-2i\omega t_1} + r_0 r_2 e^{-2i\omega(t_1+t_2)} + r_1 r_2 e^{-2i\omega t_2}}, \tag{B.8}$$

$$G^+(z_a, z_0, \omega) = \tau_0 \frac{e^{-\frac{1}{2}i\omega t_1} + r_1 r_2 e^{-i\omega(\frac{1}{2}t_1 + 2t_2)}}{1 + r_0 r_1 e^{-2i\omega t_1} + r_0 r_2 e^{-2i\omega(t_1+t_2)} + r_1 r_2 e^{-2i\omega t_2}}. \tag{B.9}$$

To verify our result, we compute the time time domain expression for the series expansion of equation B.8 to yield

$$\begin{aligned} G^-(z_a, z_0, t) =& \tau_0\{r_1\delta(t - \frac{3}{2}t_1) + r_2\delta(t - \frac{3}{2}t_1 - 2t_2) - \\ & r_0 r_1^2 \delta(t - \frac{7}{2}t_1) - r_1^2 r_2 \delta(t - \frac{3}{2}t_1 - 2t_2) + ...\}, \end{aligned} \tag{B.10}$$

$$= \tau_0\{r_1\delta(t - \frac{3}{2}t_1) + \tau_1^2 r_2 \delta(t - \frac{3}{2}t_1 - 2t_2) - r_0 r_1^2 \delta(t - \frac{7}{2}t_1) + ...\}, \tag{B.11}$$

where τ_1^2=$1 - r_1^2$ and t_1 and t_2 describe the time for a wave to traverse, in one direction, the length of the first and second layers, respectively. These waves in equation B.11 are shown in the ray diagram, see Figure B.1 and correctly correspond to the events in Figure 4.1. Note that the retrieval of the Green's function in equation B.11 takes into account the transmission coefficients of the layers.

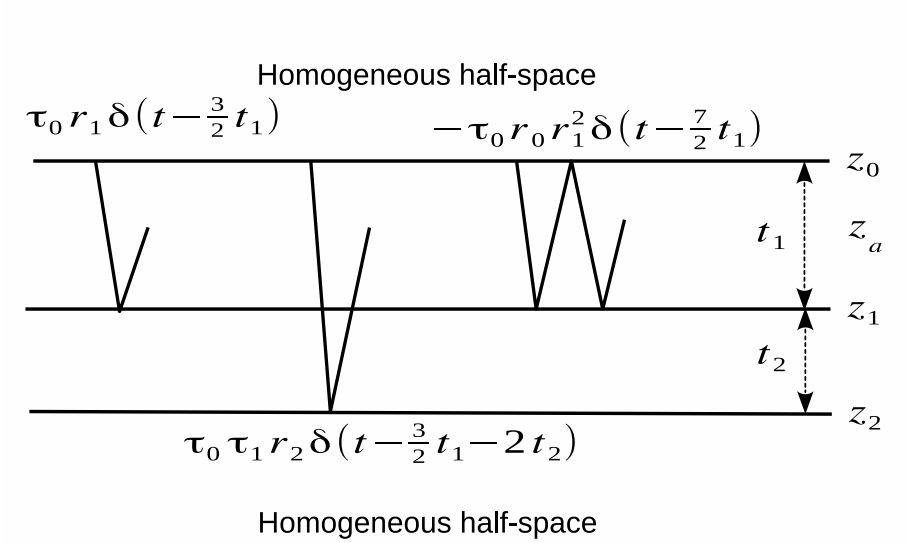

Figure B.1: Ray diagram of the waves in $G^-(z_a, z_0, t)$, equation B.11.

B.2 Green's function retrieval at the second layer z_1

To retrieve the Green's function at the second layer $z = z_1$, we compute (analytically) the reflection response at z_0 and the transmission response at z_1 for the truncated medium Υ_1. The truncated medium Υ_1 is homogeneous at and below z_1 and the same as the actual model above z_1. For this reason, the reflection response for the truncated medium Υ_1 remains the same as the reflection response in the truncated medium Υ_a as no new interfaces are included.

The transmission response for the truncated medium Υ_1 becomes $T(z = z_1, z_0, \omega) = \tau_0 e^{i\omega t_1}$. The corresponding focusing functions become

$$f_1^-(z_1, z_0, \omega) = \frac{1}{\tau_0} e^{i\omega t_1}, \tag{B.12}$$

$$f_1^+(z_1, z_0, \omega) = \frac{r_0}{\tau_0} e^{i\omega t_1}. \tag{B.13}$$

Substituting equations B.12, B.13, and B.1 into equations B.4 and B.5 yields the Green's function at the second layer:

$$G^{-}(z_1, z_0, \omega) = \tau_0 \frac{r_1 e^{-i\omega t_1} + r_2 e^{-i\omega(t_1+2t_2)}}{1 + r_0 r_1 e^{-2i\omega t_1} + r_0 r_2 e^{-2i\omega(t_1+t_2)} + r_1 r_2 e^{-2i\omega t_2}}, \tag{B.14}$$

$$G^{+}(z_1, z_0, \omega) = \tau_0 \frac{e^{-i\omega t_1} + r_1 r_2 e^{-i\omega(t_1+2t_2)}}{1 + r_0 r_1 e^{-2i\omega t_1} + r_0 r_2 e^{-2i\omega(t_1+t_2)} + r_1 r_2 e^{-2i\omega t_2}}. \tag{B.15}$$